2-22-2016

Solid state synthesis and characterization of the rare earth-free anti-perovskites Sr2.5-xBa0.5Al1-xP xO4F (0 ≤ x ≤ 0.15), Sr3Al1-xY xO4F (0 ≤ x ≤ 1), and Sr2.5-x/2Ba0.5 Al1-xHfxO4F (0 ≤ x ≤ 0.1) as potential phosphor materials

Sean Thomas Keil
Illinois State University, stkeil@ilstu.edu

SOLID STATE SYNTHESIS AND CHARACTERIZATION OF THE RARE EARTH-FREE ANTI-PEROVSKITES $Sr_{2.5-x}Ba_{0.5}Al_{1-x}P_xO_4F$ ($0 \leq x \leq 0.15$), $Sr_3Al_{1-x}Y_xO_4F$ ($0 \leq x \leq 1$), AND $Sr_{2.5-\frac{x}{2}}Ba_{0.5}Al_{1-x}Hf_xO_4F$ ($0 \leq x \leq 0.1$) AS POTENTIAL PHOSPHOR MATERIALS

Sean T. Keil

92 Pages

Typical lighting systems such as incandescent and fluorescent bulbs are common in homes but are rather inefficient compared to the newer light emitting diodes (LEDs). LED-based lamps can be constructed to generate white light by combining a red, green, and blue LED, or by using an LED light source (typically with a low wavelength) with a complimentary phosphor coating to produce white light. The latter, known as phosphor-conversion (PC) LEDs, is the primary focus of this research, looking specifically at rare earth-free options for these phosphor coatings.

Anti-perovskites are a potential lattice type for this type of conversion, in particular the A_3MO_4F (*A*= Sr, Ba, Ca; *M*= Al, Ga) tetragonal structure. Photoluminescence has been observed in the Sr_3AlO_4F system upon doping with various lanthanides, but rare earth metals are expensive, scarce due to increased use in new technologies, and their mining process introduces toxins into the environment. Focusing on doping without rare earth metals will prove beneficial as people are becoming more

conscientious of their carbon footprint and new dopants will lower the cost for the consumer.

Isovalent and aliovalent doping on the Sr_3AlO_4F lattice has been demonstrated on the *A* site (Sr), and this proven technique has introduced many rare earth trivalent cation ions as successful dopants. Doping on the *M* site (Al) is less studied but various non-rare earth (RE) cations such as Ga^{3+}, Si^{4+}, and In^{3+} have been incorporated on this site, making this site the primary focus of this thesis. The specific cations investigated are P^{5+}, Y^{3+}, and Hf^{4+} to expand the range of isovalent dopants and determine if aliovalent doping can be achieved on this site. High temperature synthesis was used to synthesize the novel products $Sr_{2.5-x}Ba_{0.5}Al_{1-x}P_xO_4F$, $Sr_{3-x}Al_{1-x}Y_xO_4F$, and $Sr_{2.5-\frac{x}{2}}Ba_{0.5}Al_{1-x}Hf_xO_4F$. The structures of these oxyfluorides were analyzed *via* powder X-ray diffraction (PXRD) and neutron powder diffraction (NPD), and their photoluminescent properties were analyzed through spectrofluorimetry before and after being treated under reducing conditions.

KEYWORDS: Anti-Perovskite, Light Emitting Diodes, Neutron Powder Diffraction, Oxyfluoride, Photoluminescence, Powder X-ray Diffraction, Solid State Synthesis

SOLID STATE SYNTHESIS AND CHARACTERIZATION OF THE RARE EARTH-FREE ANTI-PEROVSKITES $Sr_{2.5-x}Ba_{0.5}Al_{1-x}P_xO_4F$ ($0 \leq x \leq 0.15$), $Sr_3Al_{1-x}Y_xO_4F$ ($0 \leq x \leq 1$), AND $Sr_{2.5-\frac{x}{2}}Ba_{0.5}Al_{1-x}Hf_xO_4F$ ($0 \leq x \leq 0.1$) AS POTENTIAL PHOSPHOR MATERIALS

SEAN T. KEIL

A Thesis Submitted in Partial
Fulfillment of the Requirements
for the Degree of

MASTER OF SCIENCE

Department of Chemistry

ILLINOIS STATE UNIVERSITY

2016

SOLID STATE SYNTHESIS AND CHARACTERIZATION OF THE RARE EARTH-FREE ANTI-PEROVSKITES $Sr_{2.5-x}Ba_{0.5}Al_{1-x}P_xO_4F$ ($0 \leq x \leq 0.15$), $Sr_3Al_{1-x}Y_xO_4F$ ($0 \leq x \leq 1$), AND $Sr_{2.5-\frac{x}{2}}Ba_{0.5}Al_{1-x}Hf_xO_4F$ ($0 \leq x \leq 0.1$) AS POTENTIAL PHOSPHOR MATERIALS

SEAN T. KEIL

COMMITTEE MEMBERS:

Eirin C. Sullivan, Chair

Christopher G. Hamaker

Shawn R. Hitchcock

ACKNOWLEDGMENTS

I would first like to thank my family for supporting me through all of my academic adventures. From a young age my parents supported me as a scientist and encouraged me to always keep pushing forward, especially during the tough times. My sister Anna, extended family, friends, and roommate Bella played a crucial support role in listening to me complain and for allowing me to be proud of my success all the while keeping me grounded. I have had the pleasure of working with many great, young scientists throughout my undergraduate and graduate careers that helped me think about my work from all angles and help me over various hurdles, whether in the lab or not.

All of this work would not have been possible without the support of my advisor, Dr. Eirin Sullivan, who proved to be an invaluable support system for my time here at Illinois State University. My continued growth and success in this Masters' program is due to her guidance in both the laboratory and the classroom. A special thanks to all of my labmates here at ISU; making it through this program would not have been possible without you all. Also, I would like to recognize those on my committee, Drs. Christopher Hamaker and Shawn Hitchcock, for taking time to support me and serve on my committee. Again, thank you to everyone who has been there for me, your acts of kindness are something I will never forget.

S. T. K.

CONTENTS

FIGURES

TABLES

EQUATIONS

SCHEMES

CHAPTER I

INTRODUCTION TO SOLID STATE LIGHTING SYSTEMS

Early Lighting Systems

Energy for lighting systems accounts for 22% of energy consumption in the U.S.,[1] making this a valuable area of research in helping to reduce one's carbon footprint. Incandescent bulbs were the primary artificial lighting source in most homes until the mid-1980s. However, since light is produced due to an electric current running through a wire filament, this process releases a lot of heat resulting in an overall efficiency of only about 5%.

The first major improvement to this bulb was the compact fluorescence light (CFL), which uses about 25% less energy and lasts up to 10 times longer. Various lighting systems such as halogen lamps and neon lights were invented when the priority at the time was lighting large areas, not being concerned as much with the energy required to generate this light. More commonly sought after now are light emitting diodes (LEDs), and their efficiency compared to incandescent bulbs is even greater, as they use 20% of the energy and can last up to 25 times longer.[2,3]

Other than efficiency, the toxicity of CFLs should also be of concern to the industry. Mercury vapor is found inside of these bulbs and is inherently toxic on a large scale.[3] If a mercury-containing bulb is broken in your home, mercury poisoning is not of concern to adults if cleaned and ventilated properly due to the minute amount of mercury

used,but these bulbs need to be carefully handled and recycled as mercury can leak into the surrounding environment if they are improperly disposed of in landfills.

Light Emitting Diodes (LEDs)

While LEDs are more efficient and emit less heat than a standard CFL bulb,[3] they commonly contain rare earth metals that are incorporated for their ability to generate specific colors. Rare earth metals are not intrinsically toxic, but they have been shown to have negative effects on certain environments with increasing concentration.[4] The mining process for rare earth metals introduces toxic byproducts into the area that can leak into the water stream; an elevated concentration of some metals can affect the body's ability to retain metals and elements necessary for normal bodily function.[5] Also, the majority of rare earth metals are mined outside of the US, thus supply is potentially unreliable and, therefore, expensive. Being able to synthesize an LED-based bulb without rare earth metals would be a large step for the lighting industry for many reasons, including efficiency, toxicity, and overall price to the consumer.

Inside of an LED bulb is a semiconductor die referred to as a diode. A diode is a two-terminal electronic component with asymmetric conductance, meaning it has low resistance to current in one direction and high resistance in the other. Semiconductors contain p-type and n-type regions, positive and negative respectively, where the dominant carriers are either positive holes or negative electrons. Separating these two fields is a charge depletion zone, shown in *Figure 1.1*, which is a non-conductive region at equilibrium. The electrons are in the conduction band and the positive holes are situated in the valence band, and when the p-type and n-type regions are connected to an external

electric field (*Figure 1.2*) the n-type region becomes relatively negative, and an electron in the n-type region can drop down into a hole in the valence band. This process emits a photon, and the distance between the conduction band and valence bands (the band gap) is directly responsible for the specific wavelength of light emitted, therefore producing the monochromatic color of LEDs.[6]

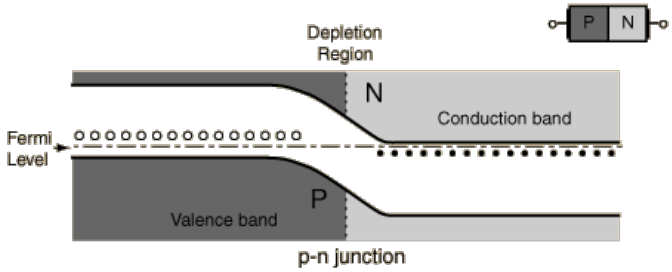

Figure 1.1. A p-n junction without an applied electric field. Adapted from HyperPhysics[6]

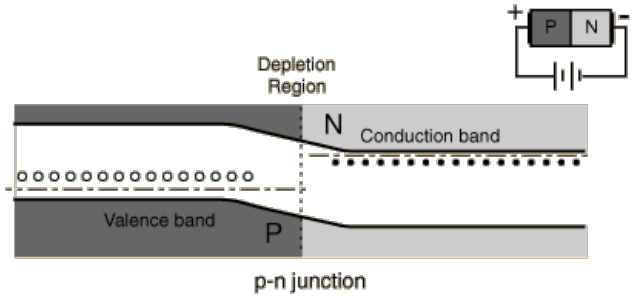

Figure 1.2. A p-n junction with an electrical field applied. Adapted from HyperPhysics[6]

In 2014 Akasaki, Amano, and Nakamura were awarded the Nobel Prize in physics based on their synthesis of an LED that emits blue light. The diode for this blue LED is comprised of gallium nitride layers with varying equivalents of indium and aluminum as dopants.[7,8] *Figure 2* shows the emission spectra for an $In_{1-x}Ga_xN$ LED, and when x is increased from 0.0 to 0.45 the wavelength of light emitted is also increaasing.[9] The change in wavelength from the UV region to the green region (through the IR region with

the appropriate dopant ions) is important to note so these LEDs can be tuned to a variety of wavelengths to fit the needs of the consumer.

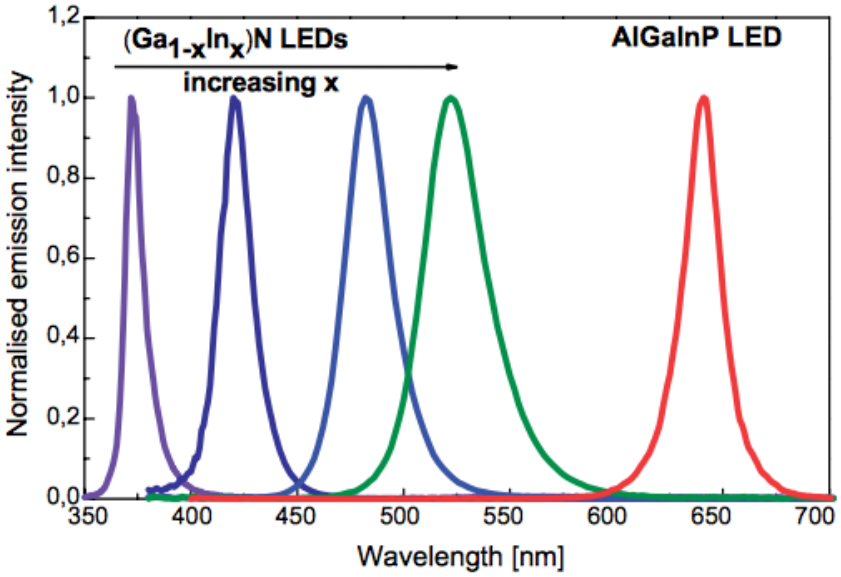

Figure 2. Emission spectrum of $In_{1-x}Ga_xN$ LED ($0 \leq x \leq 0.45$). Reproduced from Ronda[9]

Red and green LEDs, which have existed for many years prior, are primarily comprised of gallium arsenide phosphide[10] and gallium phosphide[11] respectively, although the exact composition varies due to variations in industrial processes and desired wavelength of light in the finished product. One way to produce artificial white light is through an RGB LED, which is a combination of red, green, and blue LEDs that gives the illusion of a white light. The primary issue with RGB bulbs is that the three different materials degenerate at different rates, decreasing the quality and usefulness of the light as time goes on.

Another way to generate white light is with PC-LEDs. Such devices use an LED light source combined with a phosphor coating that absorbs the wavelength emitted by the LED and emits a different wavelength *via* downconversion. Phosphors act as energy

converters, absorbing energy at one wavelength and emitting at another. Downconversion, also referred to as a Stoke's shift, is when an emitted photon has less energy than the absorbed photon, thus a higher wavelength. Upconversion, or an anti-Stoke's shift, is when the emitted photon has a lower wavelength than the absorbed photon.[12] *Figure 3* demonstrates a Stoke's and anti-Stoke's shift as would be seen from an emission spectrum. Being able to tune the composition of these phosphors allows for Stoke's or anti-Stoke's shifts to be intentionally induced to cater to a particular application.

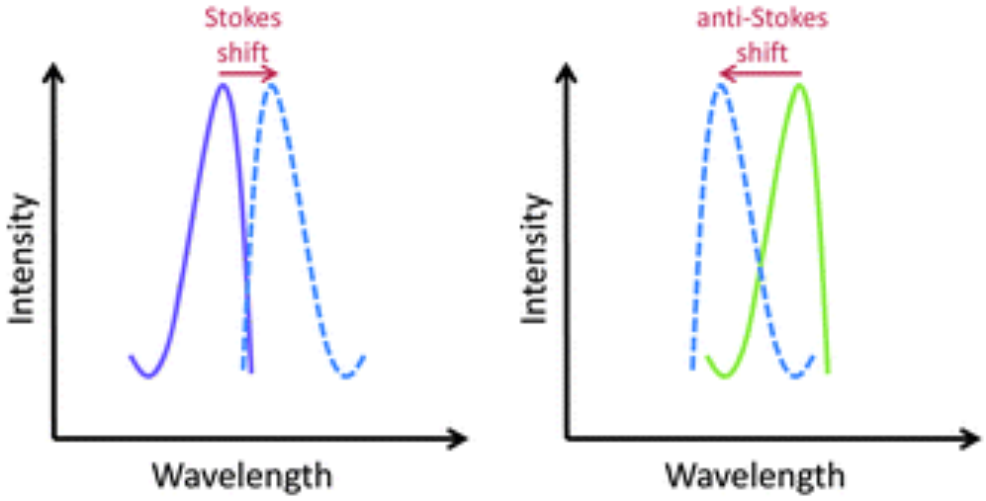

Figure 3. Stoke's shift and anti-Stoke's shift. Reproduced from Simon[12]

Typically, a blue light and a yellow phosphor coating are used to generate white light; a mixture of red and green phosphors or any pair of complimentary colors would have the same net effect. *Figure 4* is a simple representation of how a PC-LED bulb works and appears to the human eye, where the light from a blue LED interacts with yellow phosphor grains to generate a green-yellow emission. However, these grains do

not absorb all of the blue light, so the net effect of blue and green-yellow emissions yields a white light.[13]

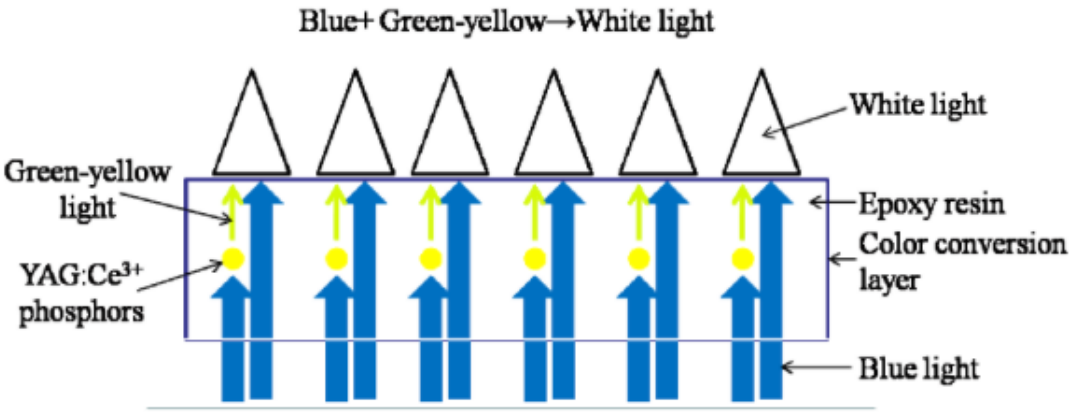

Figure 4. Representation of the inside of a PC-LED. Reproduced from Huang[14]

Photoluminescence

Luminescence is the emission of light by a material after it has absorbed non-heat energy. There are many types of luminescence and they are characterized by their excitation source: chemiluminescence, which encompasses bioluminescence, produces light due to a chemical reaction; photoluminescence, on the other hand, uses light as an excitation source, typically a UV light. Photoluminescence can further be broken down into two types, fluorescence and phosphorescence, which are dependent on the time lapse between excitation and emission. Fluorescence describes emissions where the luminescence stops as soon as the excitation source is removed, such as turning off a light bulb; phosphorescence refers to emissions that continue long after the excitation source has been removed, as seen in glow-in-the-dark materials.

The valence band is the highest occupied orbital, and the conduction band is the first unfilled orbital. When an electron is excited into an empty conduction band and

relaxes back down to the ground state the energy is released as a photon with a specific wavelength, hence photoluminescence is observed. This specific wavelength is what is responsible for the color emission seen. The path length between the conduction band and valence band is what results in the specific color. *Figure 5* shows the electronic transitions for three lanthanides commonly used in PC-LEDs.

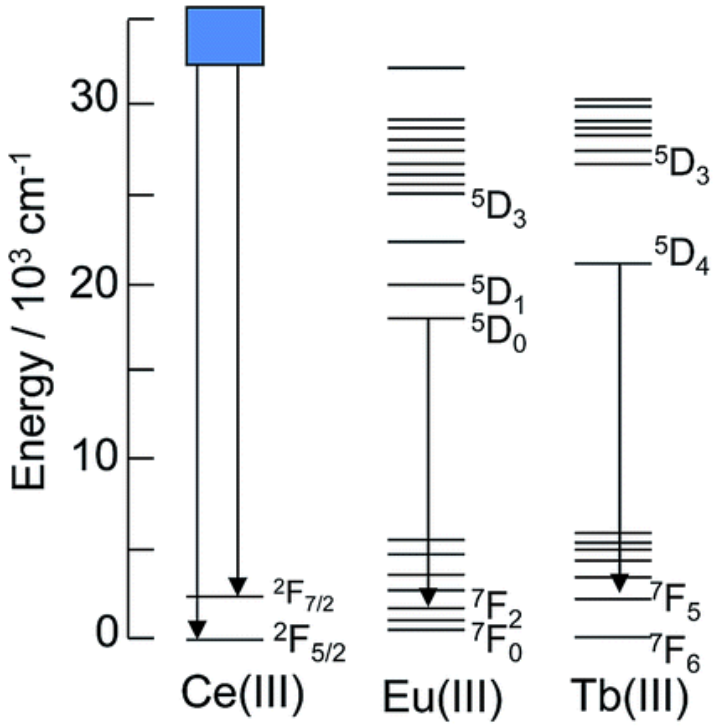

Figure 5. Electronic transitions of common rare earth metals found in LEDs. Adapted from Hasegawa[15]

The visible light spectrum ranges from 380-750 nm, where the lower wavelengths ($\lambda \approx$ 380-495 nm) correspond to a purple-blue color, green has an emission range of 495-570 nm, and yellow to orange then red correspond to increasing the wavelength from 570 to 750 nm. White light can be generated either by combining all of the wavelengths of visible light or by mixing complimentary colors, as discussed for RGB-LEDs and PC-LEDs. **Figure 6** shows the emission spectra of daylight compared with white light

emission from different light sources. The net effect of white light remains constant but its composition can vary; for instance daylight has a broad emission compared to that of different light bulbs, where CFL specifically shows line emissions. These line emissions arise from the rare earth dopants used in the phosphor coating, increasing the tunability of the light but decreasing the overall efficiency.

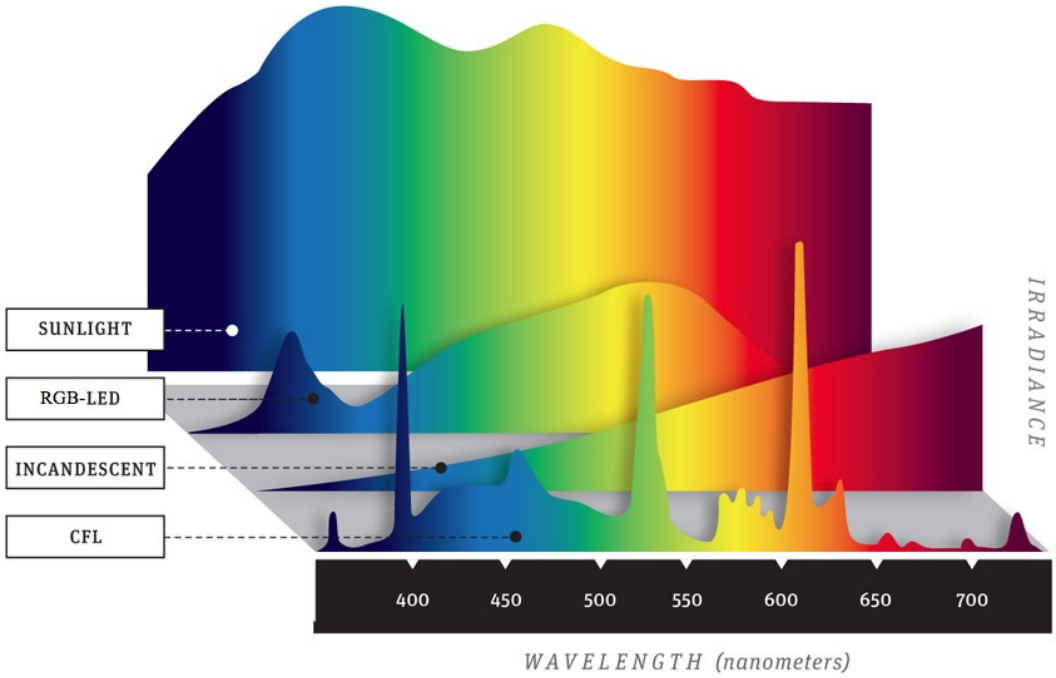

Figure 6. Emission spectra of various light sources. Adapted from Popular Mechanics[16]

A broad emission is seen when electronic states of an activator ion strongly interact with vibrational modes of the host lattice. In the case of *Figure 6*, the LED shows a broad emission, which is desirable because it most closely resembles that of natural light. Line emissions are where energy levels of an activator only show weak interactions with the host lattice; doping with rare earths leads to strong line emissions. These line

emissions are tailored around red, green, and blue wavelengths (610, 540, and 450 nm respectively) since the human eye is not equally sensitive to all colors.

Quantifying Color

RGB LEDs and PC-LEDs can be engineered to generate a white light, but their spectral distributions are not the same as daylight. There are many ways a light source can look or feel, which in turn affects what purposes it can be used for. One way to quantify the quality, or usefulness, of an artificial light source is by how well it mimics natural light. The color rendering index (CRI) describes how well a light source mimics natural light by comparing the colors of an object under artificial and natural light. CRI is scored on a 0-100 scale, where 100 is equivalent to natural light. Fluorescent lamps appear white, but have a relatively low CRI due to the small emission of red and green, causing an uneven spectral distribution. Fluorescent lamps' CRI values typically top out around 75, but the improved upon CFLs have a greater CRI value as high as 95.[1] The red, green, and blue emissions are line emissions as opposed to a broad emission, so although the light appears white it may be less comfortable to the human eye due to the less than desirable CRI. *Figure 7* shows colored pencils under various light sources with differing CRI values. Moving from left to right, it is clear that as the CRI value approaches 100 the colors look more accurate, and thus more appealing. This speaks to the importance of the tunability of LEDs to not only produce white light but one that mimics natural light.

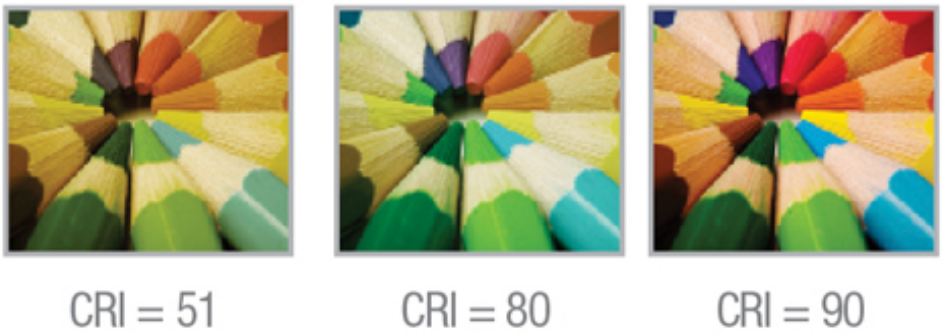

Figure 7. Increasing CRI value and the effect on color reproducibility. Reproduced from MDidea[17]

In 1931 the Commission Internationale de l'Eclairage (International Commission on Illumination, CIE) created the CIE 1931 color space, *Figure 8*, which reduces RGB tristimulus values to an *x* and *y* coordinate system to help mathematically quantify colors. By connecting any two points on the CIE graph, any color on that line can be produced by varying amounts of the two starting colors. This is particularly useful for designing white light emitting devices because if the line passes through the white area, as possible between blue and yellow, then a light that appears white to the human eye can be generated. Upon collecting photoluminescent data, the CIE coordinates of *x* and *y* can be calculated and plotted on the CIE graph.

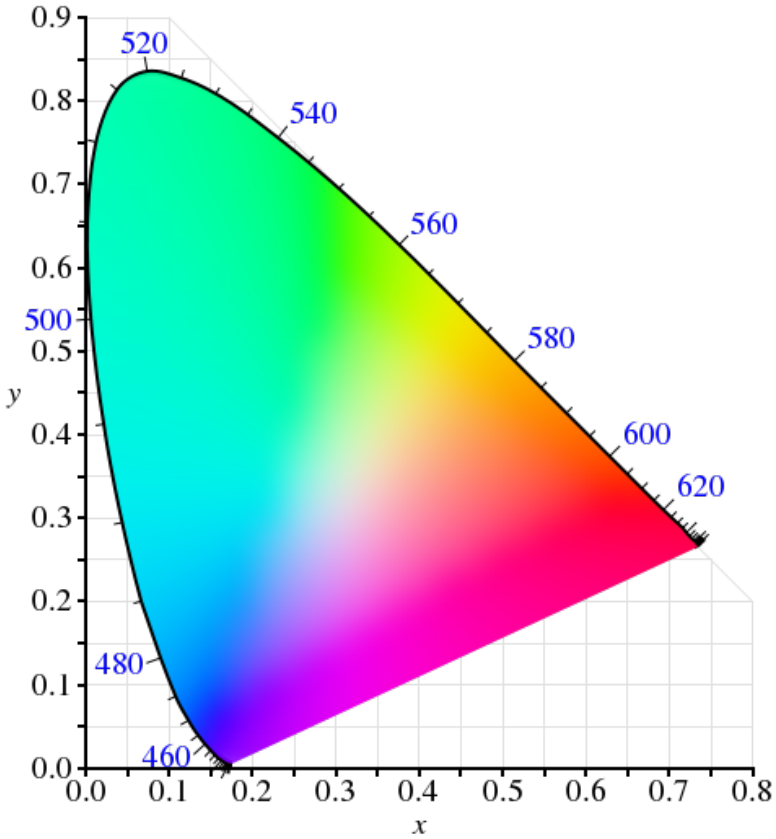

Figure 8. CIE 1931 color space. Reproduced from Guild[18]

The color of light can be quantified mathematically, but light can also have a certain feel. Light can feel "warm" or "cool" and is quantified with the correlated color temperature (CCT) scale. CRI and CCT are independent of one another, but work together to accurately describe the quality of light in question. The CCT is the temperature at which an ideal black body radiator emits a color that is comparable to the light source in question, as far as human color perception is concerned. As materials are heated to temperatures of ~1500 K, they appear "warm" or red, like embers of a fire. When this temperature increases to ~6000 K, the material has less of a color hue and appears white. This white color can be quantified as warm/cool, but this scale would also include other whites like daylight or a bright white. At temperatures of ~9000 K these

materials appear “cool” or blue, like the sky. The CCT scale is shown in *Figure 9* where cooler light appears blue and is beneficial for studying or working, but warmer light appears red and seems more relaxing making warm whites preferred in many homes.[19]

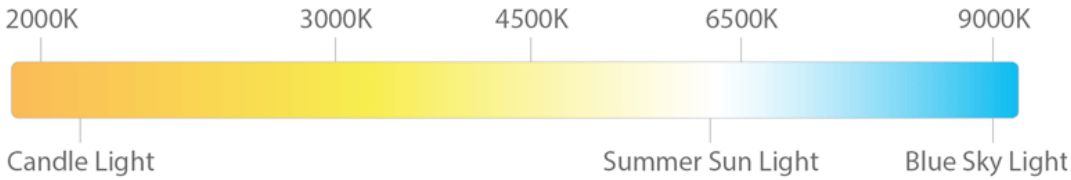

Figure 9. Correlated color temperature scale. Adapted from Smart Energy[19]

PC-LED devices can be tuned for the specific emission desired by the consumer by either changing the composition of the phosphor coating or the LED. The aim of this thesis is to investigate novel phosphors to work with blue/UV LEDs to generate a white light. These phosphor coatings are typically synthesized through high temperature solid-state reactions; this type of reaction between two or more solids completely disrupts their structure, resulting in the formation of a new, non-molecular, crystalline solid.

Crystal Structures

A crystal lattice can be formed from the repetition of a unit cell, which is the smallest group of atoms that has the overall symmetry of a crystal of that substance. A cubic crystal system is the simplest, where all of the sides are equidistant and all corners are right angles, but *Figure 10* shows all seven unique crystal systems. The seven crystal systems can all possess different symmetry elements, referred to as point groups, and each point group helps describe a mirror plane, glide plane, or other symmetry element present in the structure.[73]

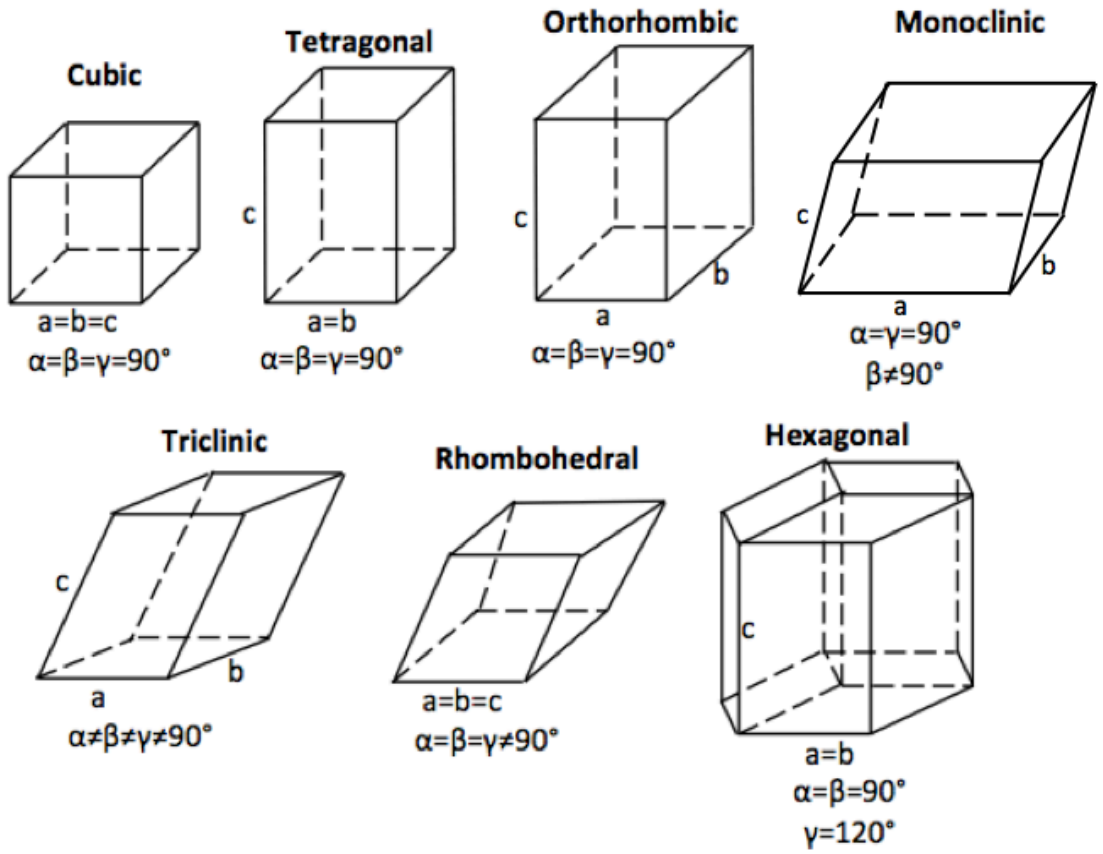

Figure 10. Visualization of the seven unique crystal structures. Adapted from Smart[73]

Along with the seven crystal systems there are four lattice types: primitive (*P*), with a lattice point at each corner; body-centered (*I*), with a lattice point at each corner and one in the center of the cell; face-centered (*F*), with a lattice point at each corner and one at the center of each face; and side-centered (*A, B,* or *C*), with a lattice point at each corner and one at the center of a pair of opposite faces.[73] Combining the seven crystal systems and four lattice types gives rise to 14 Bravais lattices, shown in *Figure 11*.

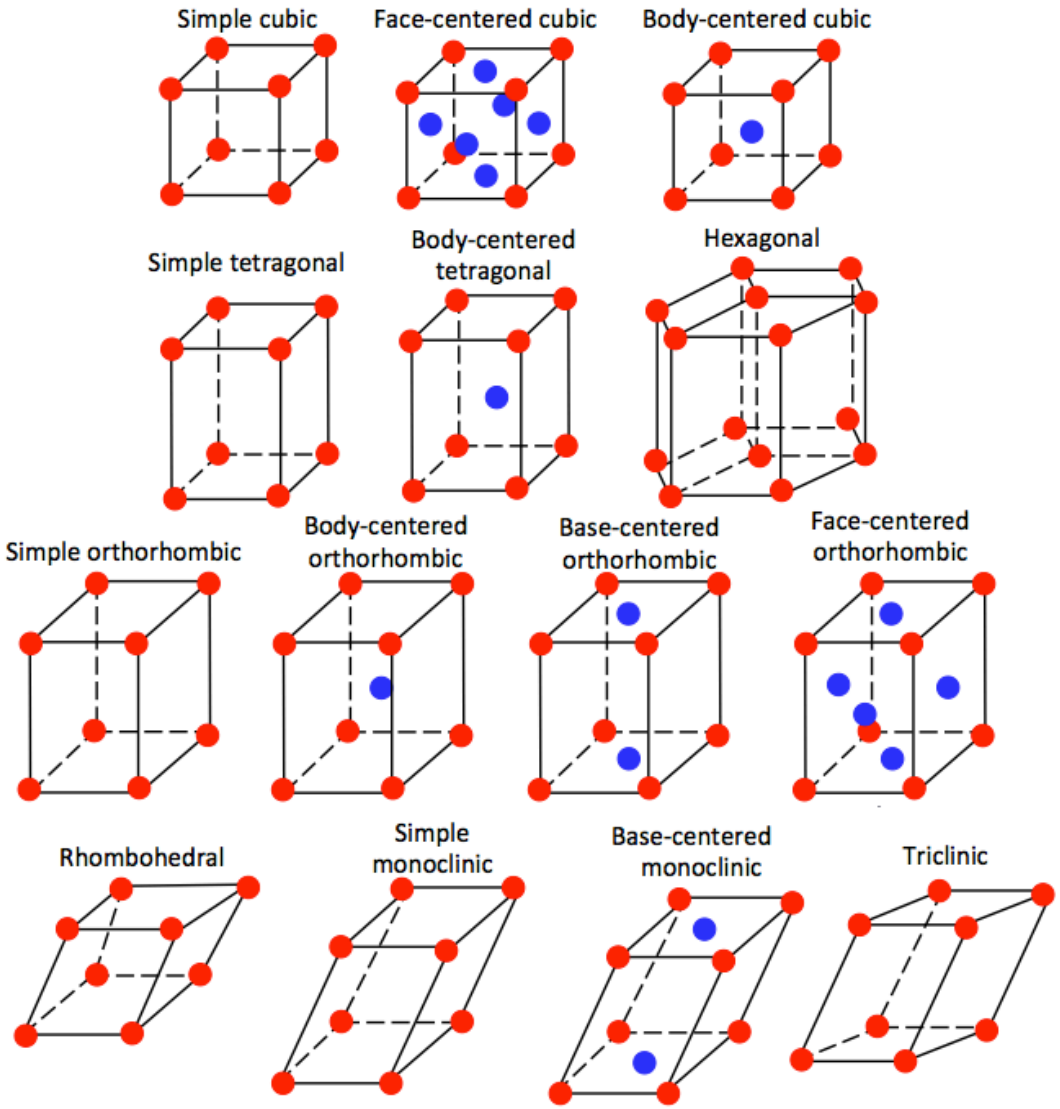

Figure 11. Visual representation of the 14 Bravais lattice types. Adapted from Smart[73]

Combining the 32 point groups with the 14 Bravais lattices allows for 230 different space groups describing all possible crystal symmetries. Space groups are reported in Herman-Mauguin notation, which simply indicates the type of lattice and symmetry elements present.[73] Using one of the most common space groups as an example, $P2_1/c$ would imply a primitive unit cell with a 2_1 screw axis that is orthogonal (at a right angle) to a *c* glide plane.

Perovskites and Anti-Perovskites

An ideal perovskite structure is described as a cubic crystal system with a primitive lattice type, as seen in *Figure 12.1*. The general formula is ABX_3, where *A* is a large body-centered cation and *B* is a small cation that is octahedrally coordinated to *X*, which is an anion positioned on the edges resulting in BX_6 corner-linked octahedra. Typically *A* is an alkaline earth metal, *B* is another metal cation (such as a transition metal), and *X* is oxygen.

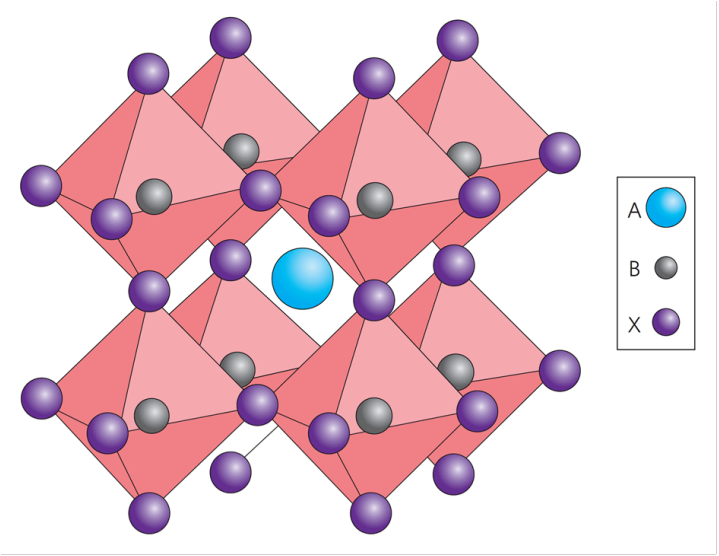

Figure 12.1. An ideal cubic anti-perovskite. Adapted from Green[20]

The mineral named perovskite, $CaTiO_3$, was first believed to exhibit a cubic crystal system and is modeled in *Figure 12.2*. This is a different view of the unit cell, where the BX_6 octahedra is at the origin of the unit cell (TiO_6), and Ca (*A*) is in blue on each of the corners.

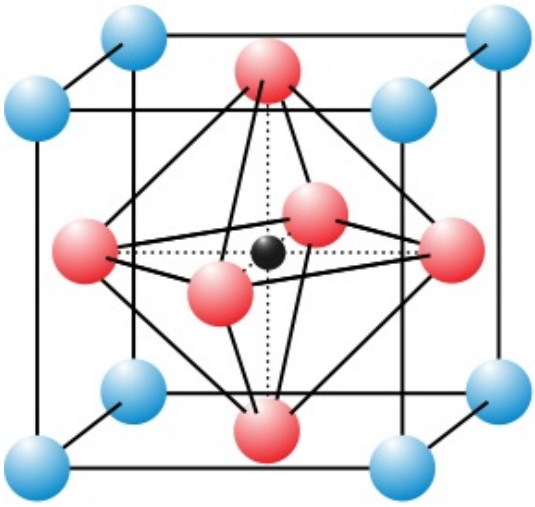

Figure 12.2. Unit cell of an ABX_3 perovskite. Reproduced from Pfaff[21]

It was later discovered that $CaTiO_3$ is orthorhombic, not cubic. Distortions arise as different elements are introduced to the compound that can change the general shape of the system, primarily due to the ion size. To quantify these distortions, the Goldschmidt tolerance factor[22] (t), *equation 1*, can be used to predict the structure based on the ion sizes, where R_A, R_B, and R_X are the ionic radii for the ions in a structure with a ABX_3-type formula:

$$t = \frac{R_A + R_X}{\sqrt{2}(R_B + R_X)}$$

Equation 1. Goldschmidt tolerance factor

In the case of $CaTiO_3$, the t value is calculated as 0.896, suggesting that the crystal is not a perfect perovskite: a t value greater than 1.01 suggests a hexagonal perovskite; between 0.9-1.01 suggests a cubic perovskite; 0.75-0.9 suggests an orthorhombic, rhombohedral, or tetragonal perovskite; if this value is under 0.75 the crystal is no longer classified as a perovskite. The t value is close to that of a cubic

perovskite, indicating that the Goldschmidt tolerance factor is a general guideline, not a determining factor. Other characterization techniques need to be taken into consideration for an exact determination of the crystal structure. By increasing or decreasing the size of the *A* and *B* cations, the cell parameters will change accordingly. A typical cubic perovskite, such as $SrTiO_3$, has ideal cation sizes for a cubic shape, but as the size of the *A* cation increases or the *B* cation decreases, the structure becomes hexagonal as seen in $BaNiO_3$.[23] Orthorhombic structures, such as the aforementioned $CaTiO_3$, arise when the *A* cation is too small to fit into the *B* interstices.

"Anti" structures are those where the cation and anion positions have been switched. Anti-perovskites, have the general formula X_3AB where *X* is a cation positioned on the edges, *A* is a large anion located at the body center, and *B* are the small anions on the corners, forming corner-linked anion-centered BX_6 octahedra.

Structural Defects

An ideal crystal system repeats the unit cell with uniform spacing and no defects; however, that is almost never the case. Only at absolute zero can a perfect crystal exist because they become imperfect at real temperatures due to atomic vibrations. These structural defects exist in crystals in many ways, either at just one point in the lattice or throughout the entire lattice.

There are two types of point defects, intrinsic and extrinsic. Intrinsic defects are stoichiometric in nature and the composition of the crystal is unchanged; these intrinsic defects can be categorized further as Schottky or Frenkel defects. A Schottky defect is where an ion is removed from its lattice site, leaving a vacancy. Schottky defects always lead to two vacancies, an anion and a cation vacancy, thereby preserving the

electroneutrality of the crystal. Additional ions on the surface of the compound preserve its stoichiometry. Frenkel defects are formed when an ion is displaced from its lattice site into an interstitial site that is normally empty. Due to the way materials crystalize and pack, there are "holes" or open spaces in the structure, allowing a cation to fit in this space. Anion Frenkel defects are possible, however, they are less common since the anions are typically larger than the cations in a given structure.[73] *Figure 13* shows these two defects where C+ indicates the cations, A- indicates the anions, and V is any created vacancies.

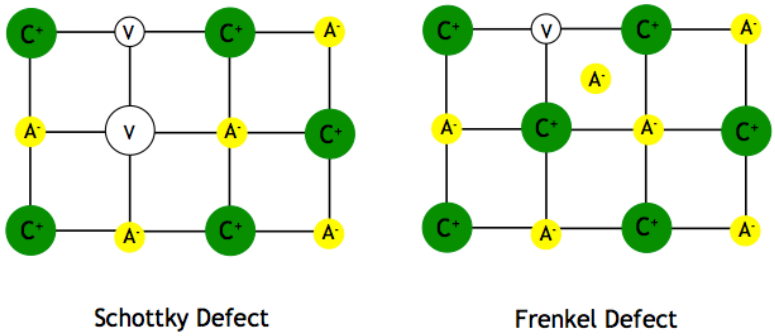

Figure 13. Representation of Schottky and Frenkel defects. Adapted from Smart[73]

Extrinsic or non-stoichiometric defects are commonly caused when the compound has a composition where the ratio of atoms is not an integer, as is the primary case when doping samples in this thesis. Stoichiometry is never perfect at the local level so extrinsic defects exist to some extent in all crystal structures. When doping with an aliovalent ion, vacancies are created to compensate for the difference in charge. For example, when doping with 0.1 equivalents of P^{5+}, one would not expect the compound $Sr_3Al_{0.9}P_{0.1}O_4F$ to form because it would not be charge neutral and would therefore be unstable. One would predict the composition $Sr_{2.9}Al_{0.9}P_{0.1}O_4F$, where the amount of Sr^{2+} in the

compound has been reduced to compensate for the charge of this aliovalent substitution, creating strontium cation vacancies.

Another way to dope with aliovalent elements without creating vacancies is by co-doping with another ion to charge compensate. Commonly seen when doping on the Sr^{2+} site with a trivalent cation such as Ce^{3+}, Na^{+} is introduced to help balance the charge of the compound. For example, doping on the Sr_3AlO_4F structure with 0.1 equivalents of both Ce^{3+} and Na^{+} leads to the formula $Sr_{2.8}Ce_{0.1}Na_{0.1}AlO_4F$ which has a neutral charge without the need for vacancies.[24] All crystal structures contain some sort of defect, so it is important to carefully consider the effects of aliovalent substitution on stoichiometry and defect creation so as to minimize the formation of impurities through making minor adjustments to the formula.

Important Phosphor Materials

Yttrium aluminum garnet ($Y_3Al_5O_{12}$, commonly abbreviated as YAG) is a cubic crystal that is typically colorless, but the color of the crystal can exhibit a wide array of colors when doped with various elements. This large unit cell (*Ia*3*d*) is shown in *Figure 14* with the top layer showing the AlO_4^{5-} and AlO_6^{7-} polyhedra and just one of the YO_8^{13-} polyhedra near the bottom.[25] This structure is commonly doped with Ce^{3+} and is used as a phosphor coating to produce white light in conjunction with the $In_xGa_{1-x}N$ blue LED.[26] When the YAG:Ce^{3+} phosphor is excited at a wavelength of 460 nm (the emission range of the InGaN LED[9]), this leads to a broad emission spectra from 500-700 nm with a maximum at 540 nm. This PC-LED is currently one of the best light bulbs of its type on

the market despite having a CRI value of ~70-80;[27] the CRI value is not as high as other bulbs due to the lack of red spectral emissions.

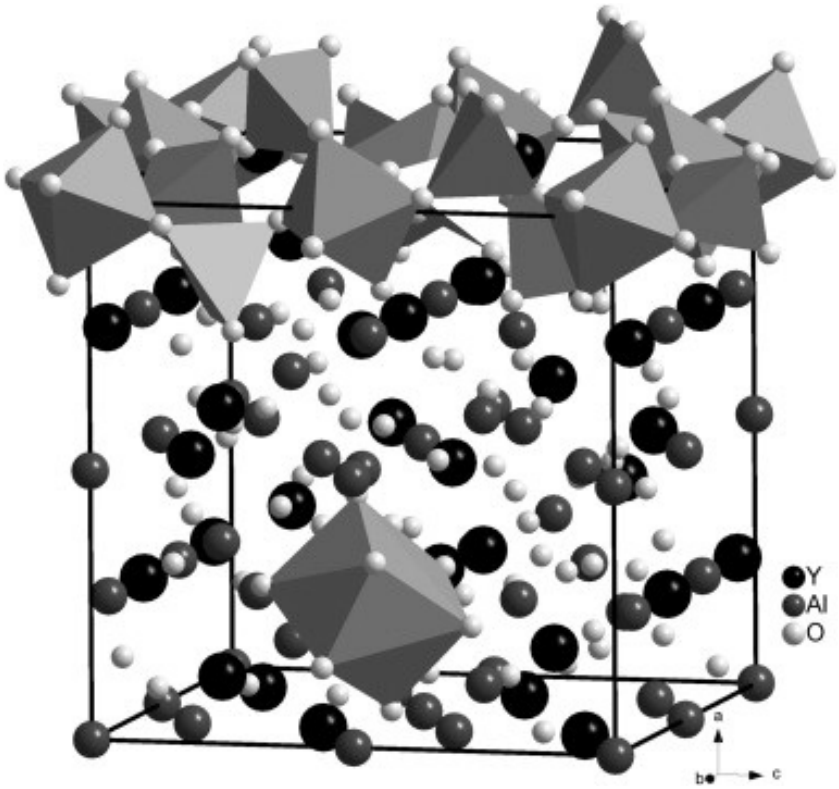

Figure 14. Unit cell of $Y_3Al_5O_{12}$ showing the three distinct polyhedra. Reproduced from Huang.[14]

Another phosphor closely related to YAG is $Ca_3Sc_2Si_3O_{12}:Ce^{3+}$. When this cubic phosphor (*Ia*3*d*) is excited at 450 nm it exhibits a broad emission band at ~505 nm that results in a yellow-green photoluminescent emission. When this phosphor is used in conjunction with $CaAlSiN_3:Eu^{2+}$ in the phosphor coating for a blue LED an overall emission is seen from 500-650 nm. This PC-LED has a CRI value of 92, making it another desirable option for solid state lighting systems.[28,29]

Magnesium germinate, $Mg_2GeO_4:Mn^{4+}$, was first synthesized in 1936 by Leverenz.[30] This olivine phosphor (*Pmnb*), when doped with excess amounts of magnesium, causes the composition to change to $Mg_{3.5}Ge_{1.25}O_6:Mn^{4+}$

($Mg_{28}Ge_{10}O_{48}:Mn^{4+}$), slightly changing the space group to *Pbam*.[31-33] When excited at 365 nm, this material shows four emission peaks between 620-660 nm, yielding a red emission.[34] The magnesium germanate phosphor was commonly used as a coating for mercury bulbs in streetlights from the 1950-70s. The typical red emission appeared to have a yellow hue, but even when the phosphor would degrade, the emission appeared orange which still made it a viable option for street lighting.[26]

This compound can be further co-doped with zinc, which plays a major role in the emission spectra exhibited.[34] As more Zn^{2+} is incorporated for Mn^{4+} the emission shifts from a red color, to orange, and then to yellow. $Mg_{28}Ge_{10}O_{48}:Mn^{4+}$ can also be doped with MgF_2, and this synthesis produced the first oxy-fluoride phosphor, $Mg_{3.5}Ge_{0.9375}O_{4.75}F_{1.25}$ ($Mg_{28}Ge_{7.5}O_{38}F_{10}$).[35,36] The addition of fluorine does not change the structure of the compound, but is useful as it increases the efficiency of the phosphor.

Strontium Aluminum Oxy-fluoride, Sr_3AlO_4F

This thesis focuses on the anti-perovskite with a general formula of A_3MO_4F, where MO_4 is the body-centered polyanion AlO_4^{5-} tetrahedron and the primary position for doping experimentation. *Figure 15.1* shows the tetragonal anti-perovskite related structure (*I*4/*mcm*) of A_3MO_4F (*A*= Sr; *M*= Al), where the Sr(1) and (2) sites are labeled accordingly, and the blue spheres are the *M* site atoms tetrahedrally coordinated to the red oxygen atoms, and the yellow spheres on the corner of the cell are the fluorine atoms. The fluorine atoms are coordinated to the strontium atoms on both the Sr(1) and Sr(2) sites forming corner-linked FSr_6 octahedra (transparent green) on the corners of the cell. Strontium is also coordinated to the MO_4 tetrahedra (transparent blue) *via* the oxygen

atoms. *Figure 15.2* is the same crystal structure but outlines the unit cell; *Table 1* lists the bonds present in the Sr_3AlO_4F anti-perovskite.[37]

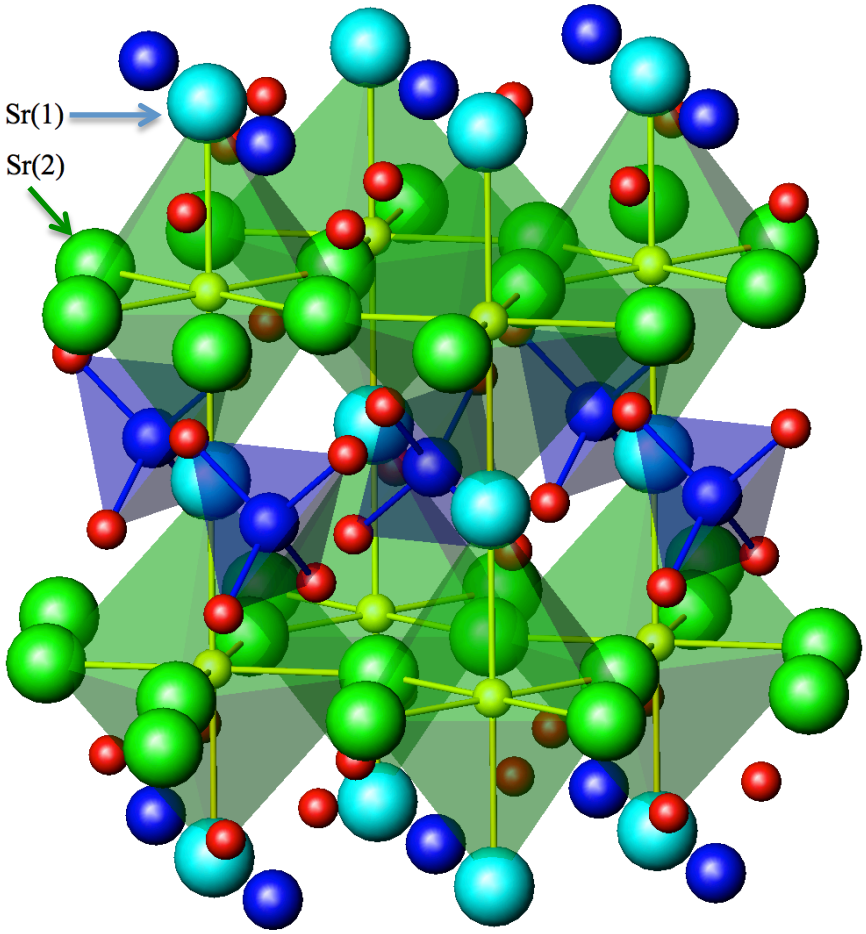

Figure 15.1. Structure of Sr_3AlO_4F [37]

Table 1. Coordination of the Atoms in the Sr_3AlO_4F Anti-Perovskite[37]

Primary Atom	*[Number of] Bonds Formed*
Sr(1)	8 x Sr(1)-O
	2 x Sr(1)-F
Sr(2)	4 x Sr(2)-O [long]
	2 x Sr(2)-O [short]
	2 x Sr(2)-F
Al	4 x Al-O
O	2 x Sr(2)-O [long]
	1 x Sr(2)-O [short]
	2 x Sr(1)-O
	1 x Al-O
F	4 x Sr(2)-F
	2 x Sr(1)-F

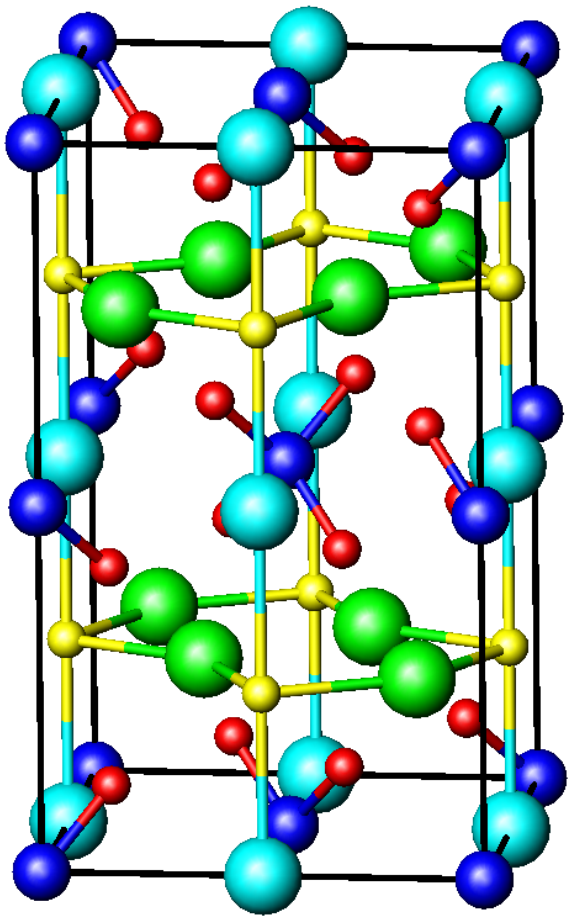

Figure 15.2. Unit cell of the Sr_3AlO_4F crystal[37]

Substituting the larger barium cation onto the Sr(1) site leads to greater stability as the Sr^{2+} cation is rather small for the 10-coordinate site. Conversely, doping with the smaller Ca^{2+} cation allows for more space in the cell when doping with large rare earth metals on this site. This was shown through the calculation of the bond valence sums which will be discussed in further detail in *Chapter III, Profile Refinement* when talking about calculations performed with these materials.[38]

Sr_3AlO_4F is not photoluminescent but can be doped with rare earth activators to form characteristic line transitions. Post-synthesis, phosphor materials can be treated with a reducing gas to induce anion defects, such as $5\%H_2(g)/95\%Ar(g)$ while heating at 900 °C, which leads to the formula $Sr_3AlO_{4-\alpha}F_{1-\delta}$. Upon annealing under reducing conditions to form $Sr_3AlO_{4-\alpha}F_{1-\delta}$, the host lattice becomes self-activating giving a broad emission. As seen in *Figure 16.1-16.2*[39], reducing the $Sr_{2.85}Eu_{0.1}Al_{0.9}In_{0.1}O_4F$ phosphor results in $Sr_{2.85}Eu_{0.1}Al_{0.9}In_{0.1}O_{4-\alpha}F_{1-\delta}$ which impacts the observed photoluminescence by adding a broad underlying emission. In *Figure 16.1* the emission spectrum is rather weak when excited at 365 nm; however, when excited at 290 nm, the emission is comprised of characteristic Eu^{3+} line emissions. After being reduced, the photoluminescence is not affected when excited at 290 nm, but when excited at 365 nm the photoluminescence also includes a broad emission.[39] Being able to induce anion defects that lead to a broad spectral distribution is useful for phosphors in solid state lighting systems by increasing the intensity of a wide range of wavelengths and resulting in a higher CRI value.

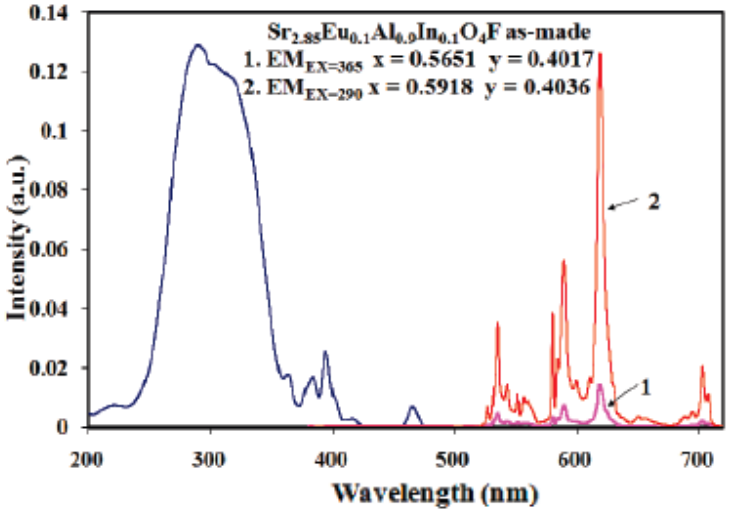

Figure 16.1. Excitation and Emission of $Sr_{2.85}Eu_{0.1}Al_{0.9}In_{0.1}O_4F$ (not reduced). Adapted from Park[39]

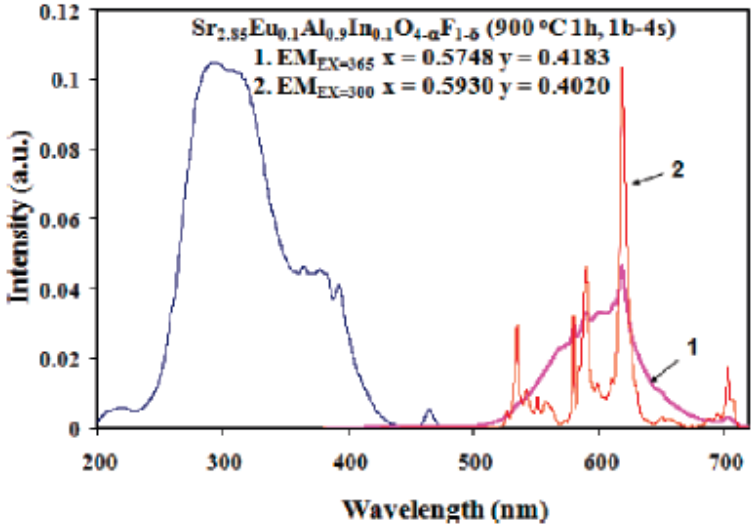

Figure 16.2. Excitation and Emission of $Sr_{2.85}Eu_{0.1}Al_{0.9}In_{0.1}O_{4-\alpha}F_{1-\delta}$ (reduced). Adapted from Park[39]

Trivalent lanthanides have been successfully incorporated onto various host lattices to induce photoluminescence. When looking specifically at the Sr_3AlO_4F cell (A_3MX), numerous lanthanide cations have been doped on the *A* site to induce photoluminescence *via* characteristic line emissions. *Figure 17* shows the CIE diagram for general trends from doping on the Sr_3MO_4F host lattice. The rare earths used are

terbium, thulium, and europium, and through varying the concentrations of these rare earths different emissions and subtle distortions to the host lattice are seen. Understanding the tunability of the excitation and emission shift with the introduction of various dopants is important to the solid state lighting industry.[40]

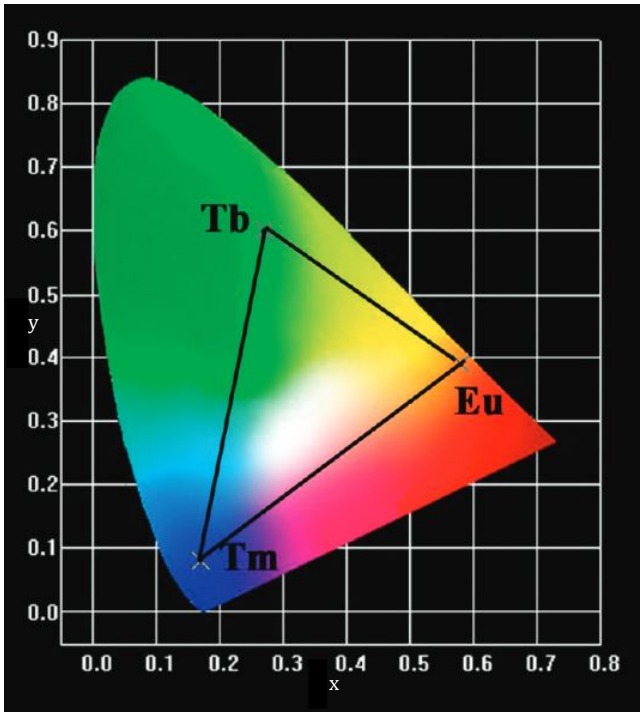

Figure 17. CIE diagram of various rare earth dopants on Sr_3MO_4F. Reproduced from Shang[40]

When doping on the Sr^{2+} site with the aliovalent Ce^{3+} cation, Sr^{2+} cation vacancies will form. To avoid these defects the Na^+ cation is co-doped at the same concentration as Ce^{3+} to maintain the electroneutrality of this compound.[24] $Sr_{2.98}Ce_{0.01}Na_{0.01}AlO_4F$ shows an emission at ~484 and 512 nm when excited at 404 and 440 nm respectively. As the concentration of Ce^{3+} (and Na^+) is increased from x= 0.01 to x= 0.20 the excitation at λ= 404 nm increases the emission wavelength to 550 nm. *Figure 18* shows the CIE coordinates for various $Sr_{3-2x}Ce_xNa_xAlO_4F$ compounds, showing the tunability of this phosphor and the effect that increasing concentrations of a rare earth

metal has on photoluminescence.[24]

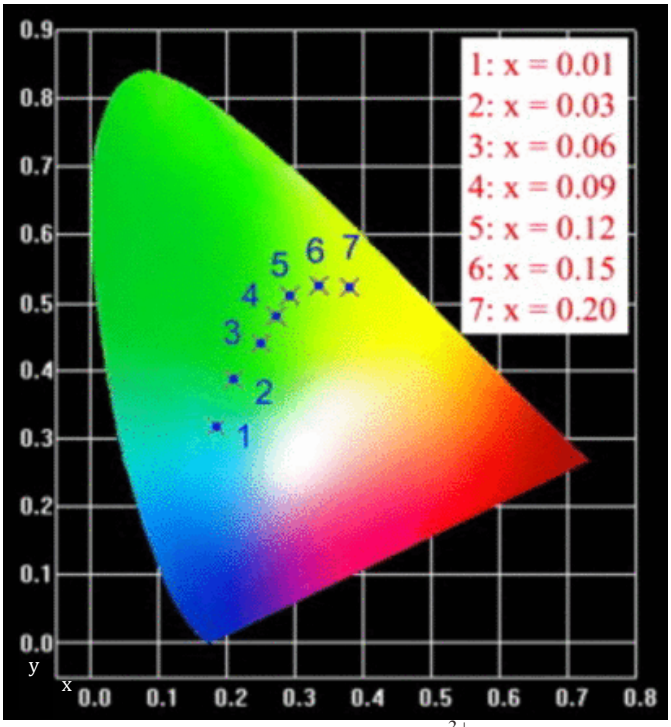

Figure 18. CIE graph of $Sr_{3-2x}Ce_xNa_xAlO_4F$ as [Ce^{3+}] is increased. Reproduced from Chen[24]

Similar to doping with Eu^{3+}, doping with Sm^{3+} results in a red emission, but this emission changes when synthesized under reducing conditions. *Figure 19* shows the tunability of $Sr_{2.5-\frac{3x}{2}}Ba_{0.5}Sm_xAlO_4F$ when excited at 254 nm when *x* is increased from 0.001 to 0.1 [A-D], but also plotted [E-H] are the same concentrations after being reduced ($Sr_{2.5-\frac{3x}{2}}Ba_{0.5}Sm_xAlO_{4-\alpha}F_{1-\delta}$). Excitation at 408 nm emits a wavelength in the red-orange region, but the emission shifts towards white after being reduced.[41]

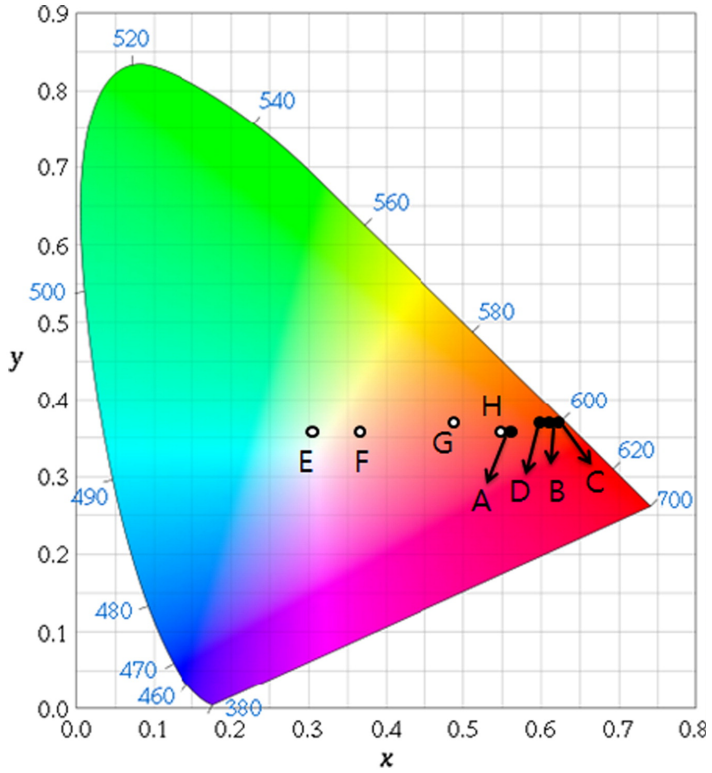

Figure 19. CIE graph of various $Sr_{2.5-3x/2}Ba_{0.5}Sm_xAlO_4F$ compounds, under normal and reduced synthesis conditions [A-D, E-H]. Reproduced from Park[41]

M-Site Doping

Doping on the *A*-site in the $Sr_{3-x}A_xAlO_4F$ (*A*= Ba, Ca, RE) compound has been well studied, yet doping on the *M*-site is not as widely reported. For this specific anti-perovskite, the *M*-site consists of some metal (*M*) bonded to four oxygen atoms forming a tetrahedron. Sr_3MO_4F was first synthesized by Vogt *et al.* in 1999[37] with Al and Ga on the *M* site individually, and both the Sr_3AlO_4F and Sr_3GaO_4F phosphors are photoluminescent when synthesized under reducing conditions.[38] When excited at a wavelength of 254 nm, $Sr_3AlO_{4-\alpha}F_{1-\delta}$ shows a blue-white emission, while $Sr_3GaO_{4-\alpha}F_{1-\delta}$ appears yellow-white.[42]

Isovalent doping on the *M*-site in the Sr_3AlO_4F phosphor has also been successfully reported with In^{3+}, showing promise for doping with non-rare earth metals.[43]

Partial doping with In^{3+} on the Al^{3+} site in this host lattice has been shown to induce photoluminescence. Specifically, the compound $Sr_{2.4}Ba_{0.6}Al_{0.9}In_{0.1}O_{4-\delta}F_{1-\delta}$ produces a broad emission band around 590 nm when excited at a wavelength between 365-372 nm. This results in a yellow emission, which could be paired with the $In_xGa_{1-x}N$ based blue LED for the production of a white light. Further doping with the Eu^{3+} lanthanide has been shown to affect the photoluminescence. When introduced in 0.1 equivalents on the Sr(2) site, yielding $Sr_{2.85}Eu_{0.1}Al_{0.9}In_{0.1}O_{4-\alpha}F_{1-\delta}$, this results in an orange emission around 619 nm with the same excitation of 365 nm.

Aliovalent doping on the *M*-site has been successfully reported with Si^{4+} up to 0.5 equivalents, and also while co-doped with various trivalent lanthanides including Ce^{3+}, Tb^{3+}, Gd^{3+}, and La^{3+}.[44,45] When charge compensation was necessary when introducing rare earth metals to the compound $Sr_3Al_{1-x}Si_xO_{4+x}F_{1-x}$ this was done with Li^+, as opposed to Na^+ as seen previously. The emission is centered ~531 nm for all of the samples when excited at 430 nm, but the emission was greatest when doped with Ce^{3+} at 0.025 equivalents. Si^{4+} is smaller than Al^{4+} (0.26 Å and 0.39 Å, respectively),[46] but the expected space group is present (*I*4/*mcm*), and this gives rise to doping on the *M*-site with an aliovalent cation.

Si^{4+} and Ge^{4+} are relatively similar in size (0.26 Å and 0.39 Å, respectively)[46] but when increasing the concentration of Ge^{4+} in the compound $Sr_{2.98-\frac{x}{2}}Na_{0.01}Ce_{0.01}Ga_{1-x}Ge_xO_4F$, the values for the global instability index varied inconsistently.[43] This could indicate that Ge^{4+} was not going into the structure, at least as readily as Si^{4+}, but major germanium containing impurities were not reported. It was

reported, however, that the photoluminescent properties of these compounds were not as great as those was reported for Si^{4+}.[43]

The CIE color space for a few of the aforementioned compounds is shown in *Figure 20*. Doping with In^{3+} is indicated by the one "In" point because the coordinates for the two compounds overlap.[47] In addition the "Si" is plotted, but when used in combination with an InGaN light source, the overall emission is very close to the theoretical white point (x=y= 0.33).[45] Also plotted on this CIE color space are where the reduced undoped $Sr_3AlO_{4-\alpha}F_{1-\delta}$ and $Sr_3GaO_{4-\alpha}F_{1-\delta}$ host lattices would appear. Al^{3+} and Ga^{3+} appear close to one another, but this is a base point for the tunability of compounds using these cations for the *M*-site. The Ge^{4+} doped compounds had CIE coordinates between the Al/Ga plots, but, as mentioned, the PL properties were not as good as when doping with either Si^{4+} or In^{3+}. If a green phosphor was being sought, Ga^{3+} would be the best starting material; where as if Al^{3+} was used it would result in phosphors with more of a blue emission.

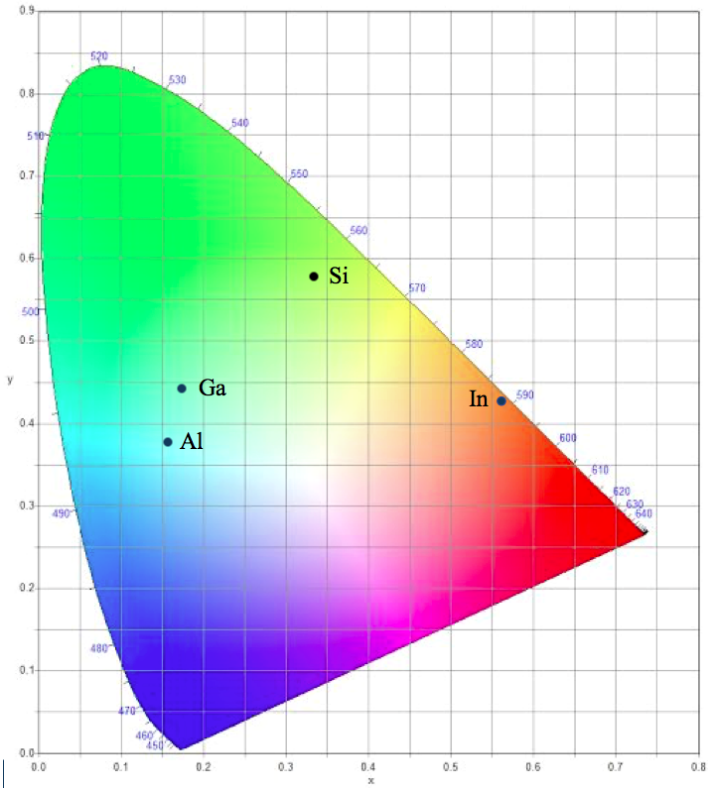

Figure 20. CIE color space of $Sr_{2.4}Ba_{0.6}Al_{0.9}In_{0.1}O_{4-\delta}F_{1-\delta}$, $Sr_{3-2x}Ce_xLi_xAl_{0.5}Si_{0.5}O_{4.5}F_{1.5}$, $Sr_3AlO_{4-\alpha}F_{1-\delta}$, and $Sr_3GaO_{4-\alpha}F_{1-\delta}$ [43,47,38,41]

Another oxyfluoride, Na_2CaPO_4F, shows a green emission when doped with 0.02 equivalents of Eu^{2+}. This rhombohedral phosphor (*R*3*m*) has a broad emission band centered at 506 nm when excited between 250-450 nm. In conjunction with a blue-emitting and red-emitting phosphor, a white LED was produced with CIE coordinates of x= 0.332, y= 0.365, a CCT value of 5540 K, and a CRI of 90.[48] Though the PL properties may be related to the doping with Eu^{2+}, the successful synthesis of PO_4^{3-} polyhedra through solid state synthesis of a related anti-perovskite system lead to the use of P^{5+} as a dopant on the Sr_3AlO_4F material to tune the CIE values.

When doping on the Al^{3+} *M*-site, the isovalent Y^{3+} cation would not require the formation of any structural defects, sparking interest for its use as a dopant. Yttrium was also chosen as a dopant of interest because of the photoluminescent properties seen from

YAG,[14] however, a structure with the YO_4^{5-} polyhedra has not yet been reported. Y^{3+} is, however, a much larger cation than Al^{3+} (0.90 Å and 0.39 Å, respectively),[46] so steric hindrances may be of concern for this dopant.

Hf^{4+} was also chosen as a dopant of interest on the *M*-site, although this does require the formation of structural defects. This Hf^{4+} cation sparked interest as it would allow for analysis of 3+, 4+, and 5+ dopants (yttrium, hafnium, and phosphorus, respectively). As stated previously Si^{4+} has been shown to incorporate on the *M* site, so it is hypothesized that Hf^{4+} should also incorporate. There is a relatively small increase in size between the Hf^{4+} and Al^{3+} ions (0.58 Å and 0.39 Å, respectively)[46] that should not result in any steric hindrances; however, Hf^{4+} is twice as large as Si^{4+} (0.26 Å),[46] so any additional strain on this compound may not allow for formation as hypothesized.

CHAPTER II

HIGH TEMPERATURE SYNTHESIS OF ANTI-PEROVSKITE RELATED COMPOUNDS

Solid State Synthesis

Solid state synthesis can be carried out in a variety of ways, the most common of which is the ceramic method. The ceramic method works on the principle of overcoming each of the starting material's lattice energies to form a new structure, something that is accomplished through long reaction times at high temperatures. When the starting materials are combined together there is a certain amount of contact between the different crystal faces referred to as the interface. At high temperatures these crystals start to overcome their lattice energies and ions begin to migrate across the interface that starts to form the new crystal, a process known as nucleation. When the reaction occurs a product layer is formed between the reactants making it harder for ions to migrate through the new structure, but intermittent grinding creates new interfaces to aid in nucleation. Pressing the powders into a pellet also allows for more surface interaction to minimize the diffusion distance of the ions.

Solid State Reactions Incorporating Phosphorus on the *M*-Site

The basis for my synthetic design was modeled from the original synthesis of the Sr_3AlO_4F anti-perovskite by Park and Vogt.[39] Stoichiometric amounts of the dry and pure starting materials were used: strontium carbonate ($SrCO_3$, 99.9%); strontium fluoride

(SrF_2, 99%); aluminum oxide (Al_2O_3); ammonium phosphate dibasic ($(NH_4)_2HPO_4$). After weighing the starting materials they were ground together with an agate mortar and pestle for five to 10 minutes or until a homogeneous powder was observed. Following reaction times of 12-16 hours at 700, 800, and 900 °C, then 48-72 hours at 1050 °C for up to three times with intermittent grinding before each heating, the compound $Sr_{3-x}Al_{1-x}P_xO_4F$ ($0 \leq x \leq 0.1$) was successfully synthesized. The synthesis conditions are adjusted according to the purity of the sample, as determined by a powder X-ray diffractometer (PXRD), and how receptive the materials are to heating at such high temperatures. *Scheme 1* is the reaction for the first material of interest, doping on the aluminum site with phosphorus.

$$2.5\text{-}x\ SrCO_3 + 0.5\ SrF_2 + \frac{1-x}{2} Al_2O_3 + x\ (NH_4)_2HPO_4 \rightarrow Sr_{3-x}Al_{1-x}P_xO_4F$$

Scheme 1. Synthesis of $Sr_{3-x}Al_{1-x}P_xO_4F$

The AlO_4^{5-} tetrahedra are being doped with an aliovalent cation, which causes a strontium cation defect, as discussed previously in *Chapter I, Structural Defects*. To reduce the amount of structural defects in the final compound, the stoichiometric amounts of starting materials are adjusted appropriately, as seen in *Scheme 1*, where the stoichiometric amount of strontium carbonate accounts for the amount of dopant introduced.

Introducing barium onto the strontium site has been shown using bond valence sum calculations by Prodjosantoso *et al.* to improve the stability of the structure.[38] Appropriate amounts of barium carbonate ($BaCO_3$) were used in this reaction. The anti-

perovskite was synthesized without Ba^{2+} for initial analysis but all other syntheses included 0.5 equivalents of Ba^{2+} as shown in *Scheme 2*.

$$2\text{-}x\ SrCO_3 + 0.5\ BaCO_3 + 0.5\ SrF_2 + \frac{1-x}{2}\ Al_2O_3 + x\ (NH_4)_2HPO_4 \rightarrow Sr_{2.5-x}Ba_{0.5}Al_{1-x}P_xO_4F$$

Scheme 2. Synthesis of $Sr_{2.5-x}Ba_{0.5}Al_{1-x}P_xO_4F$

Solid State Reactions Incorporating Yttrium on the *M*-Site

Y^{3+} and Al^{3+} are isovalent, so doping with yttrium should not require the formation of any extrinsic defects. *Scheme 3* shows the synthesis of $Sr_3Al_{1-x}Y_xO_4F$ ($0 \leq x \leq 1$). Stoichiometric amounts of the dry and pure starting materials were thoroughly ground together using an agate mortar and pestle: strontium carbonate ($SrCO_3$, 99.9%); strontium fluoride (SrF_2, 99%); aluminum oxide (Al_2O_3); yttrium oxide (Y_2O_3, 99.99%). Following reaction times of 12-16 hours at 700, 800, and 900 °C, then 48-72 hours at 1050 °C for up to three times with intermittent grinding before each heating, the compound $Sr_3Al_{1-x}Y_xO_4F$ ($0 \leq x \leq 1$) was synthesized. The synthesis conditions are adjusted according to the purity of the sample and how receptive the materials are to heating at increasingly high temperatures. Similar to *Scheme 1* for the P^{5+} doped syntheses, the larger barium cation was not included in these reactions due to the large size of the Y^{3+} ion.

$$2.5\ SrCO_3 + 0.5\ SrF_2 + \frac{1-x}{2}\ Al_2O_3 + \frac{x}{2}\ Y_2O_3 \rightarrow Sr_3Al_{1-x}Y_xO_4F$$

Scheme 3. Synthesis of $Sr_3Al_{1-x}Y_xO_4F$

Solid State Reactions Incorporating Hafnium on the *M*-Site

Similar to the phosphorus doping experiments, structural defects are required due to the aliovalent nature of Hf^{4+} and Al^{3+}. *Scheme 4* shows the synthesis of $Sr_{2.5-x/2}Ba_{0.5}Al_{1-x}Hf_xO_4F$ ($0 \leq x \leq 0.1$), and similar to *Scheme 2* the larger Ba^{2+} cation was included in these reactions due to the small size of the Hf^{4+} ion. Stoichiometric amounts of the dry and pure starting materials were weighed and thoroughly ground together using an agate mortar and pestle: strontium carbonate ($SrCO_3$, 99.9%); barium carbonate ($BaCO_3$); strontium fluoride (SrF_2, 99%); aluminum (III) oxide (Al_2O_3); hafnium (IV) oxide (HfO_2, 99.99%). Following reaction times of 12-16 hours at 700, 800, and 900 °C with intermittent grinding before heating for 48-72 hours at 1050 °C for up to three times, the compound $Sr_{2.5-\frac{x}{2}}Ba_{0.5}Al_{1-x}Hf_xO_4F$ was successfully synthesized. The synthesis conditions are adjusted according to the purity of the sample and how receptive the materials are to heating at increasingly high temperatures.

$$2-\frac{x}{2}\,SrCO_3 + 0.5\,BaCO_3 + 0.5\,SrF_2 + \frac{1-x}{2}\,Al_2O_3 + x\,HfO_2 \rightarrow$$

$$Sr_{2.5-\frac{x}{2}}Ba_{0.5}Al_{1-x}Hf_xO_4F$$

Scheme 4. Synthesis of $Sr_{2.5-\frac{x}{2}}Ba_{0.5}Al_{1-x}Hf_xO_4F$

CHAPTER III

CHARACTERIZATION OF SYNTHESIZED MATERIALS

Generation of X-Rays

X-rays are a type of electromagnetic radiation with a wavelength between 0.01 nm to 10 nm, and how this radiation interacts with a specific compound allows for its structural analysis. When X-rays interact with matter they can either scatter coherently (elastic scattering), incoherently (inelastic scattering), or be absorbed. Elastic scattering means the X-ray hits the electron cloud of the material and recoils with the same energy and wavelength; inelastic scattering results in loss of energy, so the scattered X-ray has a lower energy than the incident X-ray.

Superposition of waves results in interference patterns depending on whether the waves are in or out of phase. There are two types of interference, constructive and destructive. Constructive interference occurs when waves are in-phase, resulting in amplifications of the waves which can be detected and analyzed. Destructive interference results in an amplitude of zero because the waves are out of phase when the material being analyzed diffracts the X-rays, and this causes systematic absences if the lattice type is body-centered or face-centered, or if certain elements of symmetry are present.

X-rays are generated by bombarding electrons that excite an n= 1 (K shell) electron to a higher unoccupied state, leaving a vacancy in the K shell. Electrons in the n= 2 or 3 (L or M shell) are able to make a transition into the K shell, emitting X-rays.

Transitions from the n= 2 (L) shell to the n= 1 (K) shell gives rise to the Kα line; transitions from the n= 3 (M) shell to the n= 1 (K) shell gives rise to the Kβ line. The Kα line consists of two lines ($K\alpha_1$ and $K\alpha_2$) resulting from two L to K transitions; these emissions have similar energy but differ only due to the spin multiplicity of the 2p electrons.[73] The production of copper Kα X-rays is shown in *Figure 21* as the X-ray powder diffractometer used for analysis uses a Cu radiation source. This is a good wavelength for diffraction studies, resulting in strong scattering and good peak resolution.

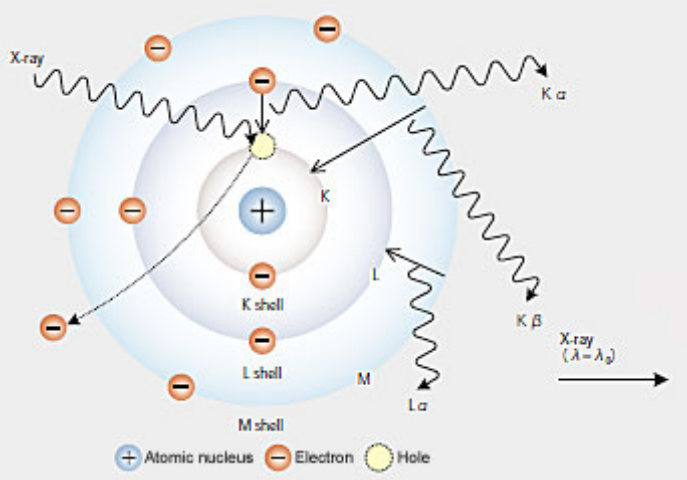

Figure 21. Generation of X-rays. Reproduced from Shimadzu[49]

Bragg's Law

X-rays interacting constructively after diffracting the material being analyzed meet the Bragg reflection conditions, represented visually in *Figure 22* and defined in *equation 2*, known as Bragg's law:

$$2d_{hkl}\sin\theta = n\lambda$$

Equation 2. Bragg's Law derivation

As long as the wavelength (λ) and angle (θ) are known, Bragg's law can be used to determine the interplanar spacing, d_{hkl}, and therefore determine the atomic positions and lattice parameters. When a known structure is changed in any way, such as the introduction of dopant ions as in this thesis, the lattice parameters should vary and these differences can be calculated. The order of diffraction, n, is an integer and indicates the difference in path length between the two scattered X-rays.

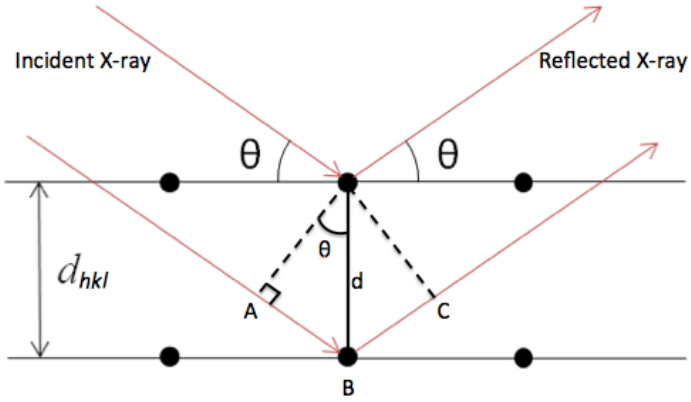

Figure 22. Schematic of the Bragg reflection. Adapted from Smart[73]

The interplanar spacing, d_{hkl}, is the spacing between planes of atoms, or Miller planes. Miller indices, calculated as h, k, and l, are used to describe a plane in the unit cell in the x, y, and z directions that intercept at some part of the unit cell at a, b, and c. Thus, the resulting Miller indices are calculated for a single plane in *equations 3.1-3.3*, followed by the interplanar spacing of a cubic crystal in *equation 4.1*, and *equation 4.2* shows how to calculate d_{hkl} of a tetragonal crystal:

$$h = \frac{a}{x}$$

Equation 3.1. Calculating interplanar spacing, d_{hkl}, of h

$$k = \frac{b}{y}$$

Equation 3.2. Calculating interplanar spacing, d_{hkl}, of k

$$l = \frac{c}{z}$$

Equation 3.3. Calculating interplanar spacing, d_{hkl}, of l

$$d^2 = \frac{a^2}{h^2 + k^2 + l^2}$$

Equation 4.1. Calculating interplanar spacing of a cubic crystal

$$d^2 = \frac{a^2}{h^2 + k^2} + \frac{c^2}{l^2}$$

Equation 4.2. Calculating interplanar spacing of a tetragonal crystal

Powder X-Ray Diffraction (PXRD)

To analyze the anti-perovskite materials synthesized PXRD is used and this technique allows for the characterization of materials since the electron cloud inherently scatters X-rays. The number of electrons an atom has is proportional to the form factor, f_0, or the scattering power of each atom, this form factor is responsible for the decreasing intensity of the reflection as the scattering angle (2θ) is increased. Although the X-ray scattering is distinctive for each atom, PXRD is not the best for differentiating between adjacent atoms on the periodic table or atoms with low atomic numbers.

Figure 23 shows the Rigaku MiniFlex™ 600 Powder X-Ray Diffractometer used for analysis of each compound. This PXRD uses a copper anode to emit X-rays at 1.5418 Å, a favorable wavelength for the crystal size of the reagents and products being analyzed. The Kβ filter, nickel in this case, is used to remove the Kβ X-rays. The $K\alpha_1$ and

$K\alpha_2$ X-rays can be separated, but this PXRD does not have a monochromator that can separate the two. The divergent Soller slits help to further filter the incident and reflected X-rays for a higher resolution. Another commonly used anode is molybdenum, which emits X-rays at 0.71 Å, which is commonly used for single crystals; a zirconium filter is commonly used with when molybdenum is used to produce the X-rays.[50]

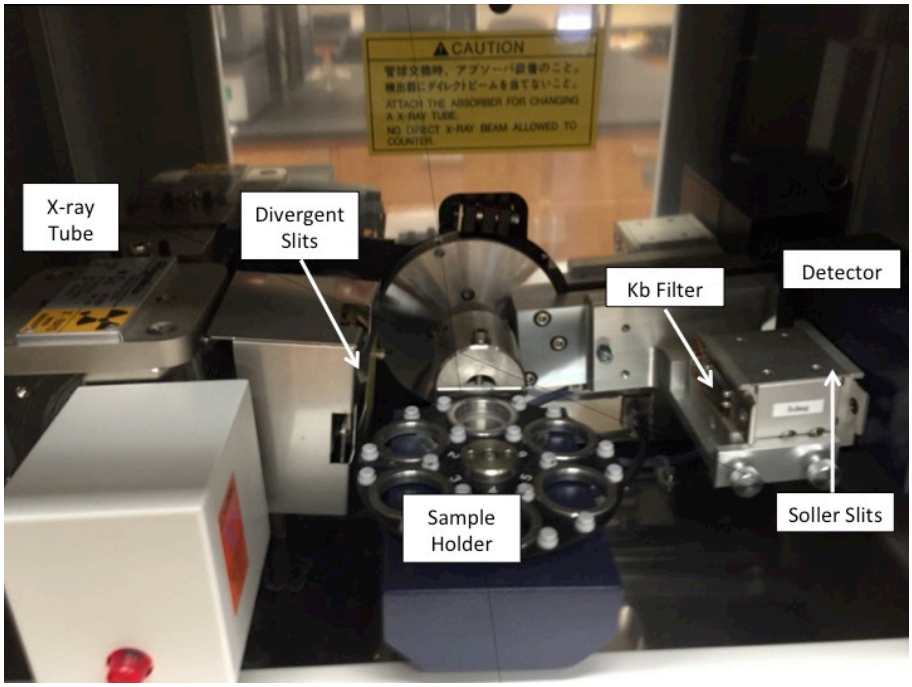

Figure 23. A labeled view inside of the Rigaku MiniFlex™ 600 PXRD

Neutron Powder Diffraction (NPD)

Another technique for analyzing powders and crystals is through neutron powder diffraction (NPD) and this offers a few advantages over PXRD. This technique is based on the same principles of PXRD, but NPD uses a nuclear reactor for an intense source of neutrons that then come into contact with the nucleus of an atom. This offers a true distance for bond lengths between nuclei, thus is a higher resolution because the atomic positions are determined very accurately. NPD does require a larger sample size since

neutrons have a low flux, but there is no drop off in intensity with 2θ which is an advantage over PXRD. Neutron scattering form factors vary irregularly with atomic and mass numbers, allowing for greater detection between adjacent elements in most cases; NPD can even be used to differentiate between different isotopes or to determine the magnetic structure.[51] NPD data for this thesis were collected at the Australian Nuclear Science and Technology Organization (ANSTO) in Sydney, Australia by Dr. Maxim Avdeev on the high-resolution neutron diffractometer Echidna that includes a Ge monochromator to select a wavelength of 1.6215 Å.

Profile Refinement

The data collected from PXRD and NPD can be analyzed through Rietveld refinement, a technique originating in the late 1960s that allows for the structural analysis of said compound. Data collected from powder diffraction are compared to a calculated fit for the specific structure based on where scattering would take place.[52-55] The refinement package used for the data presented in this thesis is GSAS, Generalized Structure and Analysis Software, which is used in conjunction with EXPGUI, Experiment Graphical User Interface, as shown in *Figure 24*.[56] Using the various tabs allow for a least squares refinement to calculate atomic parameters, background, phase fractions, constraints, and model preferred orientation.

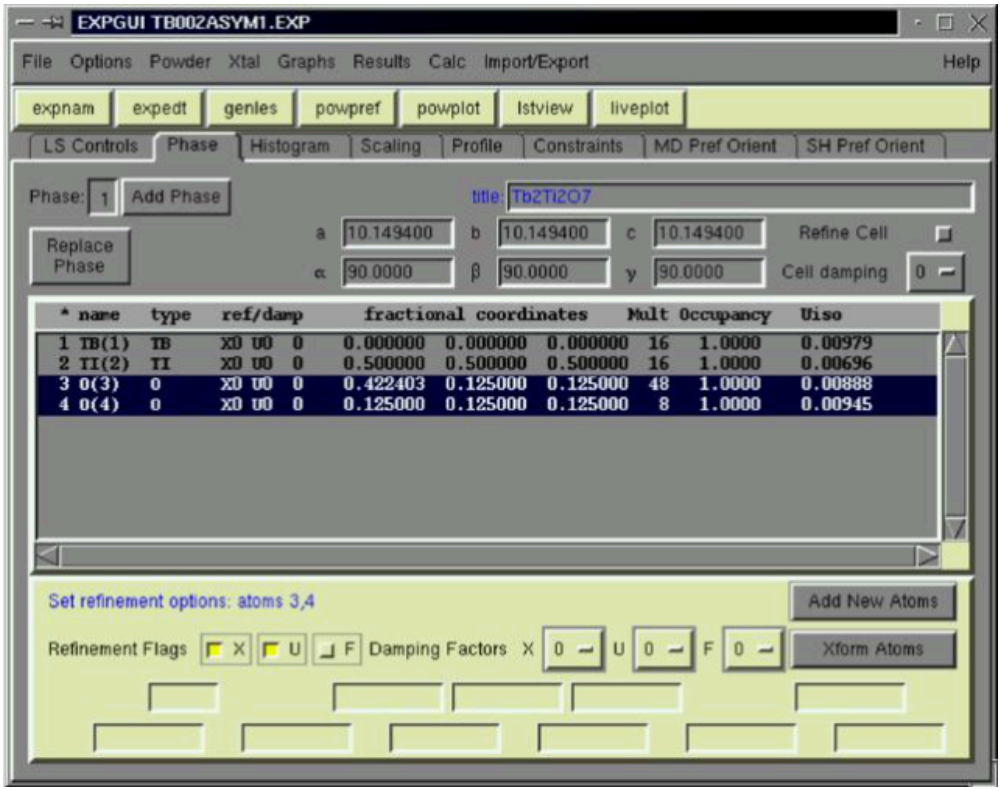

Figure 24. Screenshot of the EXPGUI interface for GSAS. Reproduced from Toby[56]

Another major component of GSAS and EXPGUI is the ability to live-plot the profile refinements. *Figure 25* shows a Rietveld refinement in process, where the red line is comprised of data points collected from the powder diffractometer, the green line is the calculated fit through least squares analysis, and the pink line is the difference between the two; ideally, a straight pink line would arise but minor inflections are expected. As this pink line visually indicates the goodness of fit, the number can be quantified as χ^2. A value of $\chi^2 = 1$ would be ideal, but this is more of a visualization technique so generally a single digit value of χ^2 is accepted as a good fit.[56] Upon completing the refinement, various structural parameters can be refined such as the lattice parameters, atomic positions, bond lengths and angles, fractional site occupancies, and thermal parameters.[56]

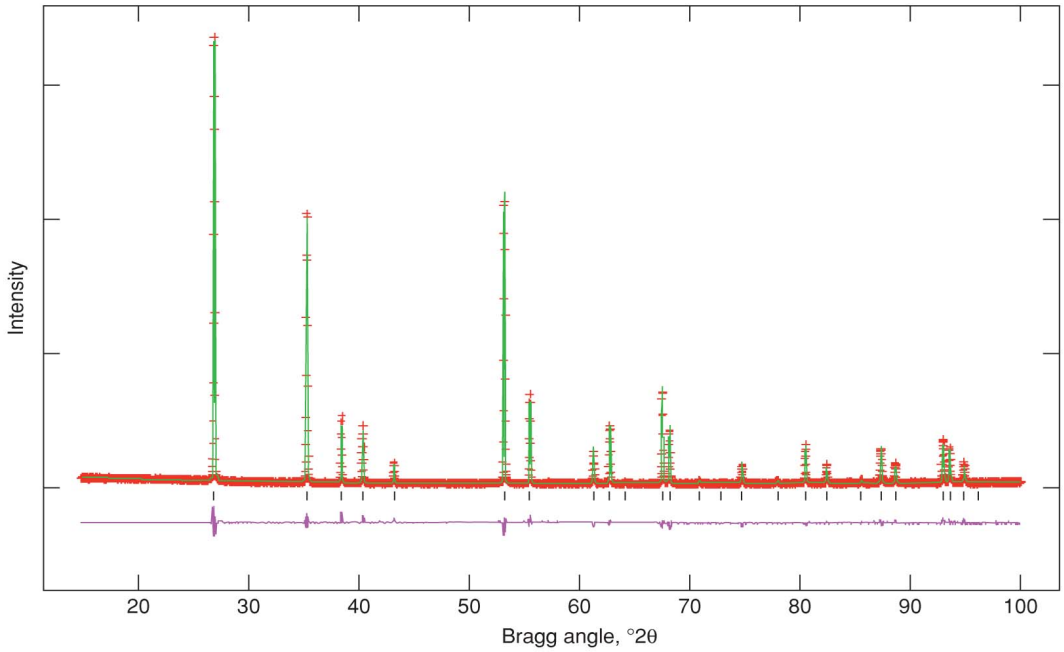

Figure 25. Rietveld refinement analyzed by E.C. Sullivan for demonstrative laboratory purposes

The oxidation state of each atom can be calculated through bond valence sum (BVS) calculations. Using the observed bond lengths the individual bond valences, *S*, are calculated in *equation 5.1* where R_0 is the ideal bond length, R_i is the observed bond length (calculated using GSAS), and *b* is an empirical constant. Typically reported as 0.37 Å, *b* can vary from 0.37-0.42 Å based on the bond type.[57,58] If the BVS value is higher than the formal valence then the structure is overbonded, indicating the ion is too large for the site; however, if this value is lower than the formal valence then the structure is underbonded, meaning the ion is too small for the site.

$$S = \exp\left(\frac{R_0 - R_i}{b}\right)$$

Equation 5.1. Calculating the bond valence sums

The difference between the expected valence (V_i) and the calculated valence (S_{ij}) is reported as d_i, the discrepancy factor (*equation 5.2*). Positive values indicate an elongation in the bonds by this ion, where a negative value indicates that the bonds are compressed.

$$d_i = \sum S_{ij} - V_i$$

Equation 5.2. Calculating the discrepancy factor

The bond valence sum is also useful to determine the stability of the structure. Using the BVS results, the global instability index, *G*, can be calculated (*equation 5.3*). If *G* is less than 0.1 it is considered stable, 0.1-0.2 indicates there is strain, and values greater than 0.2 are not often reported for stable structures.[59] The Sr_3AlO_4F compound comes with a large amount of strain, and published *G* values have been reported as high as 0.25.[36,59]

$$G = ((\sum {d_i}^2)/N)^{\frac{1}{2}}$$

Equation 5.3. Calculating the global instability index

Photoluminescence

The excitation and emission of these materials were analyzed on a Perkin-Elmer LS-55 spectrofluorimeter using a fiber optic attachment specifically designed for solid materials. The fluorescence spectrometer measures the intensity and wavelength of emitted light after excitation by a certain wavelength of light. Excitation and emission scans were taken in the ranges of 200-450 nm and 400-800 nm, respectively. Photoluminescent data were collected on these materials before and after being treated

under reducing conditions to analyze the difference in photoluminescent properties between the reduced and unreduced samples as reported by Park and discussed in Chapter I, Strontium Aluminum Oxy-fluoride.[39]

CHAPTER IV

CHARACTERIZATION OF THE NOVEL STRONTIUM ALUMINUM OXYFLUORIDE DOPED WITH PHOSPHORUS, $Sr_{2.5-x}Ba_{0.5}Al_{1-x}P_xO_4F$ [$0 \leq x \leq 0.1$]

Single Substitution

After synthesis of $Sr_{2.5}Ba_{0.5}Al_{1-x}P_xO_4F$ [$0 \leq x \leq 0.1$], the final products are a white polycrystalline solid. The data were gathered for these samples *via* PXRD with a range of 2θ= 5-145° at every 0.10 degrees at a rate of 0.20 degrees/minute; this is plotted as intensity *vs*. 2θ and was analyzed through Rietveld refinement to determine the lattice parameters, atomic positions, thermal parameters, bond length, and angles. The $Sr_{2.5-x}Ba_{0.5}Al_{1-x}P_xO_4F$ structure was confirmed to have an *I*4/*mcm* space group even as P^{5+} was incorporated. As the concentration of phosphorus was increased, so did the χ^2 values, indicating the presence of low levels of impurities that are not discernible from background noise in the PXRD data. Using GSAS and EXPGUI, the atomic positions and thermal parameters obtained are displayed in *Tables 2.1-2.4*.

Table 2.1. Atomic Positions and Thermal Parameters of $Sr_{2.5}Ba_{0.5}AlO_4F$

Atom	*x*	*y*	*z*	$U_{iso} \times 100$
Sr/Ba(1)	0	0	0.25	2.75(2)
Sr(2)	0.1702(1)	0.6702(1)	0	2.36(2)
Al	0	0.50	0.25	1.78(6)
O	0.1412(4)	0.6411(4)	0.6474(3)	2.34(8)
F	0	0	0	2.57(1)

Space Group: *I*4/*mcm*; χ^2= 5.5; *a*= 6.8571(6) Å; *c*= 11.1603(3) Å

Table 2.2. Atomic Positions and Thermal Parameters of $Sr_{2.45}Ba_{0.5}Al_{0.95}P_{0.05}O_4F$

Atom	*x*	*y*	*z*	$U_{iso} \times 100$
Sr/Ba(1)	0	0	0.25	2.33(1)
Sr(2)	0.1703(1)	0.6704(1)	0	2.62(1)
Al/P	0	0.50	0.25	1.29(1)
O	0.1435(5)	0.6433(5)	0.6507(9)	3.58(1)
F	0	0	0	2.63(1)

Space Group: *I*4/*mcm*; χ^2= 8.1; *a*= 6.8752(1) Å; *c*= 11.1459(3) Å

Table 2.3. Atomic Positions and Thermal Parameters of $Sr_{2.4}Ba_{0.5}Al_{0.9}P_{0.1}O_4F$

Atom	*x*	*y*	*z*	$U_{iso} \times 100$
Sr/Ba(1)	0	0	0.25	0.405(5)
Sr(2)	0.1724(1)	0.6724(1)	0	0.614(3)
Al	0	0.50	0.25	0.05(9)
O	0.1381(1)	0.6381(1)	0.6496(9)	1.06(3)
F	0	0	0	1.08(7)

Space Group: *I*4/*mcm*; χ^2= 16.1; *a*= 6.8757(1) Å; *c*= 11.1263(3)

Table 2.4. Atomic Positions and Thermal Parameters of $Sr_{2.35}Ba_{0.5}Al_{0.85}P_{0.15}O_4F$

Atom	*x*	*y*	*z*	$U_{iso} \times 100$
Sr(1)	0	0	0.25	2.68(6)
Sr(2)	0.1714(2)	0.6717(2)	0	2.92(6)
Al	0	0.50	0.25	3.88(3)
O	0.1461(1)	0.6461(1)	0.6707(5)	7.82(5)
F	0	0	0	3.19(4)

Space Group: *I*4/*mcm*; χ^2= 10.5; *a*= 6.8934(2) Å; *c*= 11.1201(4) Å.

After the refinements converged, the atomic positions the cell parameters were calculated and plotted in *Figure 26*. While not linear, there is an observable trend as the concentration of P^{5+} is increased. The *a* parameter is increased by almost 0.50% (from 6.8571(6) Å to 6.8934(2) Å) while *x* is increased from 0 to 0.15, but the *c* parameter contracts slightly (from 11.1603(3) Å to 11.1201(4) Å, less than 0.20%) when *x* is increased from 0 to 0.15.

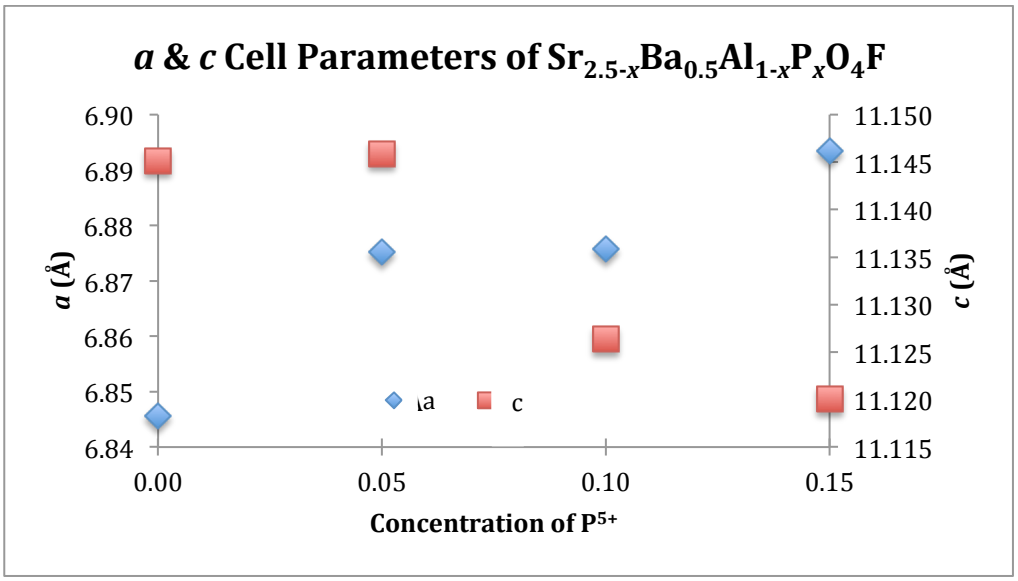

Figure 26. Cell parameters of *a* and *c* as [P^{5+}] is increased from 0 to 0.15

The observation that the *c* parameter contracts as *x* increases can be rationalized by considering the relatively small size of the P^{5+} ion compared to Al^{3+} (0.31 Å *vs*. 0.53 Å, respectively).[46] The bond of interest when doping on the *M*-site is the Al-O bond, which is 1.784(2) Å for the undoped Sr_3AlO_4F host structure, but as phosphorus is incorporated at *x*= 0.15, this bond length decreases to 1.676(1) Å. Bond lengths are reported in *Tables 3.1-3.4*.

Table 3.1. Selected Bond Lengths of $Sr_{2.5}Ba_{0.5}AlO_4F$

Bond	*Length (Å)*
8 × Sr(1)-O	2.882(1)
2 × Sr(1)-F	2.790(3)
4 × Sr(2)-O	2.702(1)
2 × Sr(2)-O	2.461(2)
2 × Sr(2)-F	2.545(1)
4 × Al-O	1.784(2)

Table 3.2. Selected Bond Lengths of $Sr_{2.45}Ba_{0.5}Al_{0.95}P_{0.05}O_4F$

Bond	*Length (Å)*
8 × Sr(1)-O	2.865(2)
2 × Sr(1)-F	2.786(1)
4 × Sr(2)-O	2.741(3)
2 × Sr(2)-O	2.469(4)
2 × Sr(2)-F	2.551(4)
4 × Al-O	1.781(4)

Table 3.3. Selected Bond Lengths of $Sr_{2.4}Ba_{0.5}Al_{0.9}P_{0.1}O_4F$

Bond	*Length (Å)*
8 × Sr(1)-O	2.888(6)
2 × Sr(1)-F	2.782(6)
4 × Sr(2)-O	2.713(1)
2 × Sr(2)-O	2.485(1)
2 × Sr(2)-F	2.545(5)
4 × Al-O	1.747(1)

Table 3.4. Selected Bond Lengths of $Sr_{2.35}Ba_{0.5}Al_{0.85}P_{0.15}O_4F$

Bond	*Length (Å)*
8 × Sr(1)-O	2.780(5)
2 × Sr(1)-F	2.783(3)
4 × Sr(2)-O	2.903(1)
2 × Sr(2)-O	2.599(2)
2 × Sr(2)-F	2.553(4)
4 × Al-O	1.676(3)

Based on the atomic positions, bond lengths, and expected valences the bond valence sums and global stability index were calculated, as reported in *Tables 4.1-4.3*. The bond valences for Sr(1) are all less than 2, which is consistent with the literature and indicates underbonding. Ba^{2+} was included to help alleviate structural instability arising from the Sr^{2+} ion being rather small for the 10-coordinate Sr(1) site. The valence of Al^{3+}

is calculated as 2.5657 for x= 0, which increases to 3.4382 when x= 0.15, as was hypothesized due to the incorporation of the +5 phosphorus ion.

Using these values the global stability index value can be calculated, and this indicates how much strain there is in the structure. For the undoped compound the G value is calculated as 0.31, a high value but one common to the literature value of 0.25.[36,59] As more P^{5+} is incorporated on the Al^{3+} site the G value decreases to 0.28 for x= 0.10, indicating that the introduction of P^{5+} is relieving some of the strain of the cell. As the concentration of P^{5+} is increased, the underbonded Al^{3+} site becomes less underbonded (d_i increases from -0.4343 for x= 0 to -0.1510 for x= 0.10). The structure cannot incorporate phosphorus past x= 0.10, most likely due to charge considerations and steric hindrances. Impurities arise after this concentration because any phosphorus not successfully incorporated into the cell can cause phosphorus-containing impurities or appear as the unreacted starting material. Often times these impurities form before the successful synthesis of the cell, meaning there are not enough starting materials to form the cell of interest.

Table 4.1. Bond Valence Sums and Global Stability Index of $Sr_{2.5}Ba_{0.5}AlO_4F$

Atom	V_i	S_{ij}	d_i
Sr(1)/Ba(1)	2	1.2489	-0.7511
Sr(2)	2	2.0697	0.0698
Al	3	2.5657	-0.4343
O	2	1.7034	-0.2966
F	1	1.1404	0.1405
G		0.31	

Table 4.2. Bond Valence Sums and Global Stability Index of $Sr_{2.45}Ba_{0.5}Al_{0.95}P_{0.05}O_4F$

Atom	V_i	S_{ij}	d_i
Sr(1)/Ba(1)	2	1.2977	-0.7023
Sr(2)	2	1.9641	-0.0359
Al/P	3	2.5887	-0.4113
O	2	1.6715	-0.3285
F	1	1.1287	0.1287
G		0.29	

Table 4.3. Bond Valence Sums and Global Stability Index of $Sr_{2.4}Ba_{0.5}Al_{0.9}P_{0.1}O_4F$

Atom	V_i	S_{ij}	d_i
Sr(1)/Ba(1)	2	1.2350	-0.7650
Sr(2)	2	1.8770	-0.1230
Al/P	3	2.8490	-0.1510
O	2	1.7320	-0.2860
F	1	0.9110	-0.0890
G		0.28	

Table 4.4. Bond Valence Sums and Global Stability Index of $Sr_{2.35}Ba_{0.5}Al_{0.85}P_{0.15}O_4F$

Atom	V_i	S_{ij}	d_i
Sr(1)/Ba(1)	2	1.5750	0.4250
Sr(2)	2	1.4685	0.5315
Al/P	3	3.4382	-0.4382
O	2	1.7059	0.2941
F	1	1.1266	-0.1266
G		0.29	

If phosphorus were to be successfully incorporated into the cell at higher concentrations, I would expect the volume of the cell to continue to decrease, but with no further outcomes such as a structural change. The Goldschmidt tolerance factor calculation with Al^{3+}, and P^{5+} results in a *t* value greater than one, and due to the smaller size of P^{5+} compared to Al^{3+}, it is reasonable that this would result in a larger Goldschmidt tolerance factor; as the *A* ion increases with size (in this case Sr^{2+} remains constant) or the *B* ion decreases in size (from 0.39 Å for Al^{3+} to 0.17 Å for P^{5+}) the *t* value increases, but with values over 1.0 for each calculation both perovskites would appear to be hexagonal in nature according to the Goldschmidt tolerance factor. However, the Sr_3AlO_4F anti-perovskites are tetragonal, so as stated previously the

Goldschmidt tolerance factor should only be used as a guideline and not a determining factor.

The Rietveld refinements, *Figures 27.1-27.4*, are plotted to include thousands of calculated points gathered from PXRD or NPD (in red), a green line which is the calculated values, and a pink line at the bottom which is the difference between these two; as χ^2 nears 1 (the best possible χ^2 value), the pink line becomes more linear.

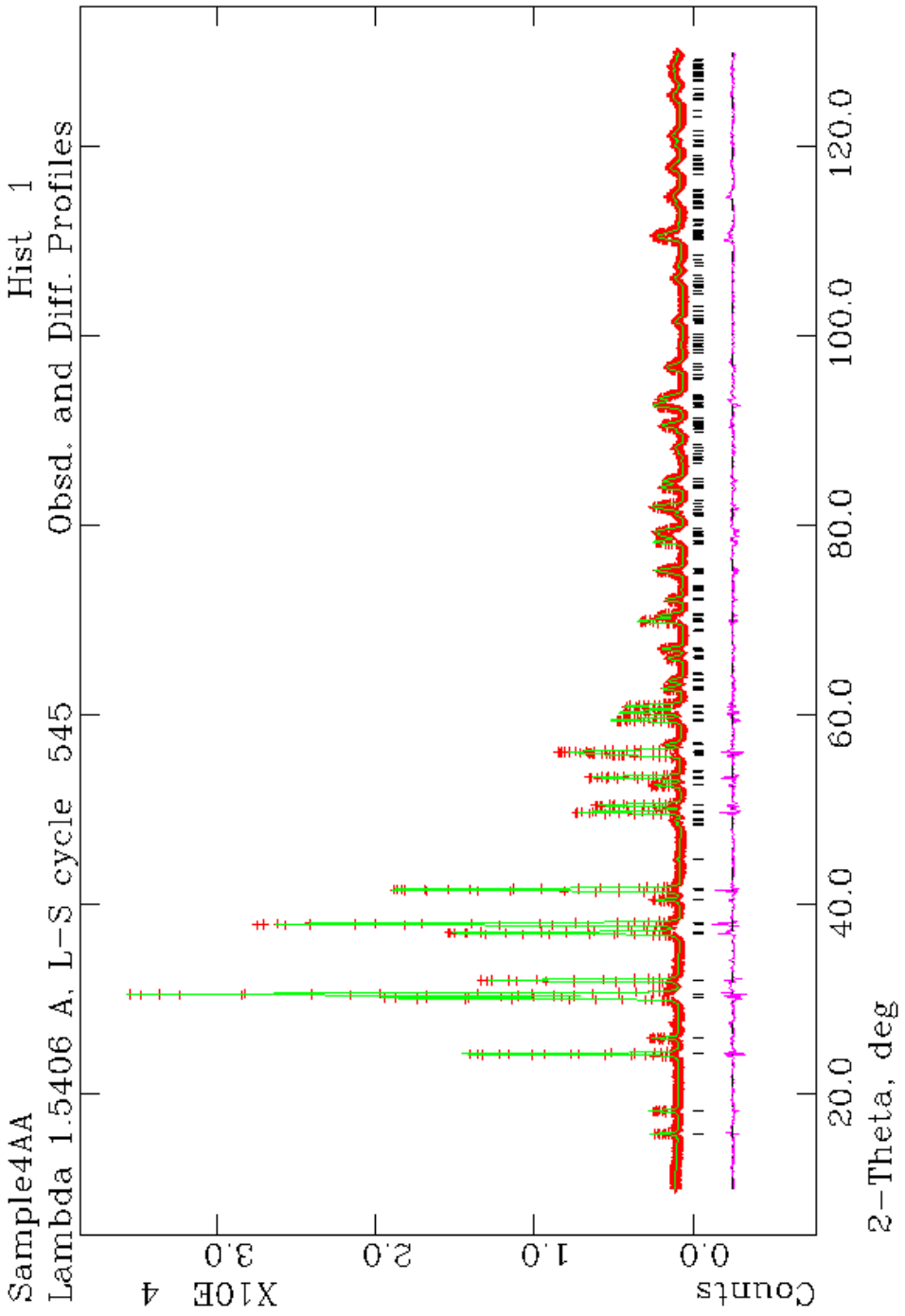

Figure 27.1. Rietveld refinement based upon PXRD data for $Sr_{2.5}Ba_{0.5}AlO_4F$

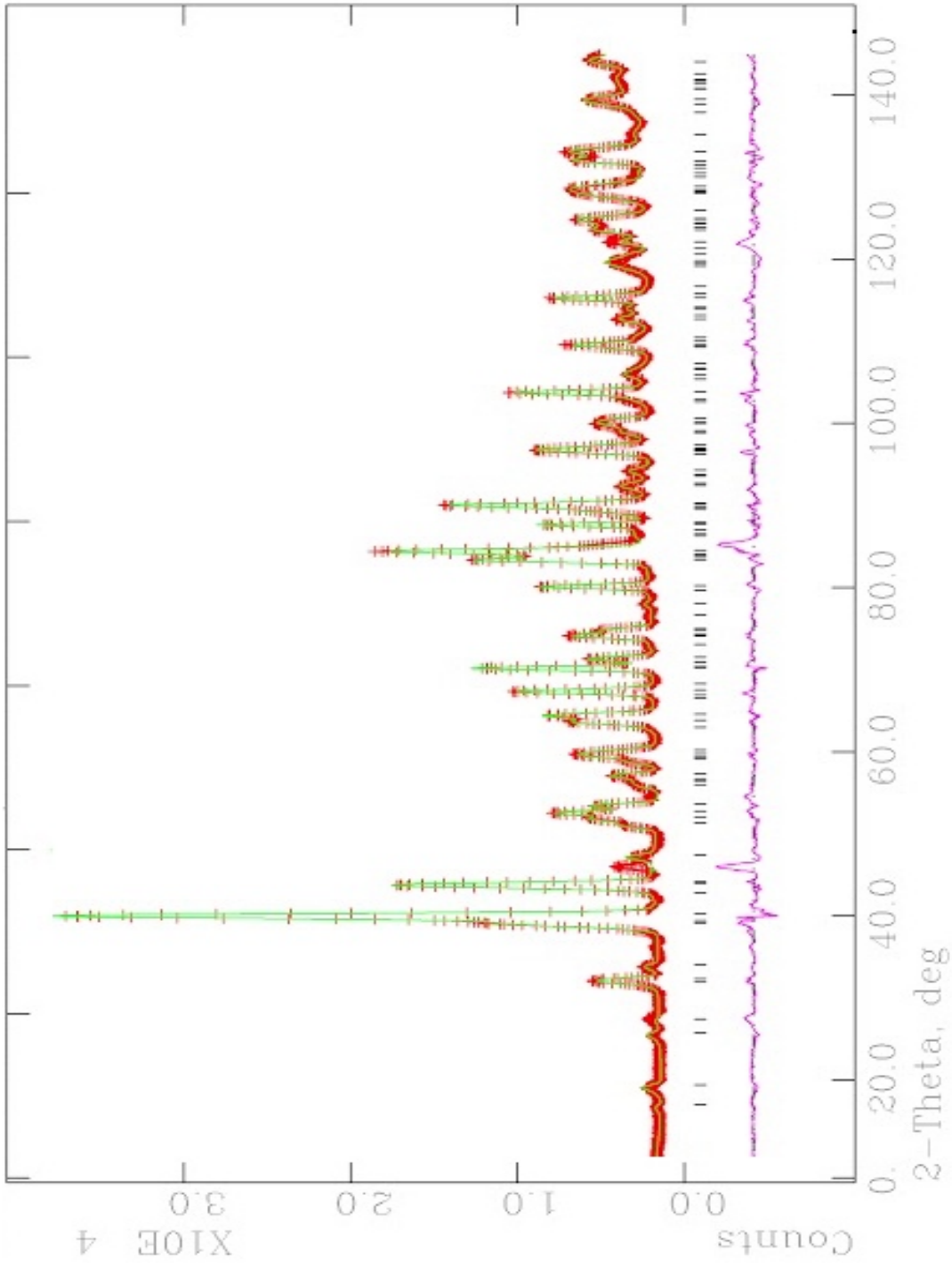

Figure 27.2. Rietveld refinement based upon PXRD data for $Sr_{2.45}Ba_{0.5}Al_{0.95}P_{0.05}O_4F$

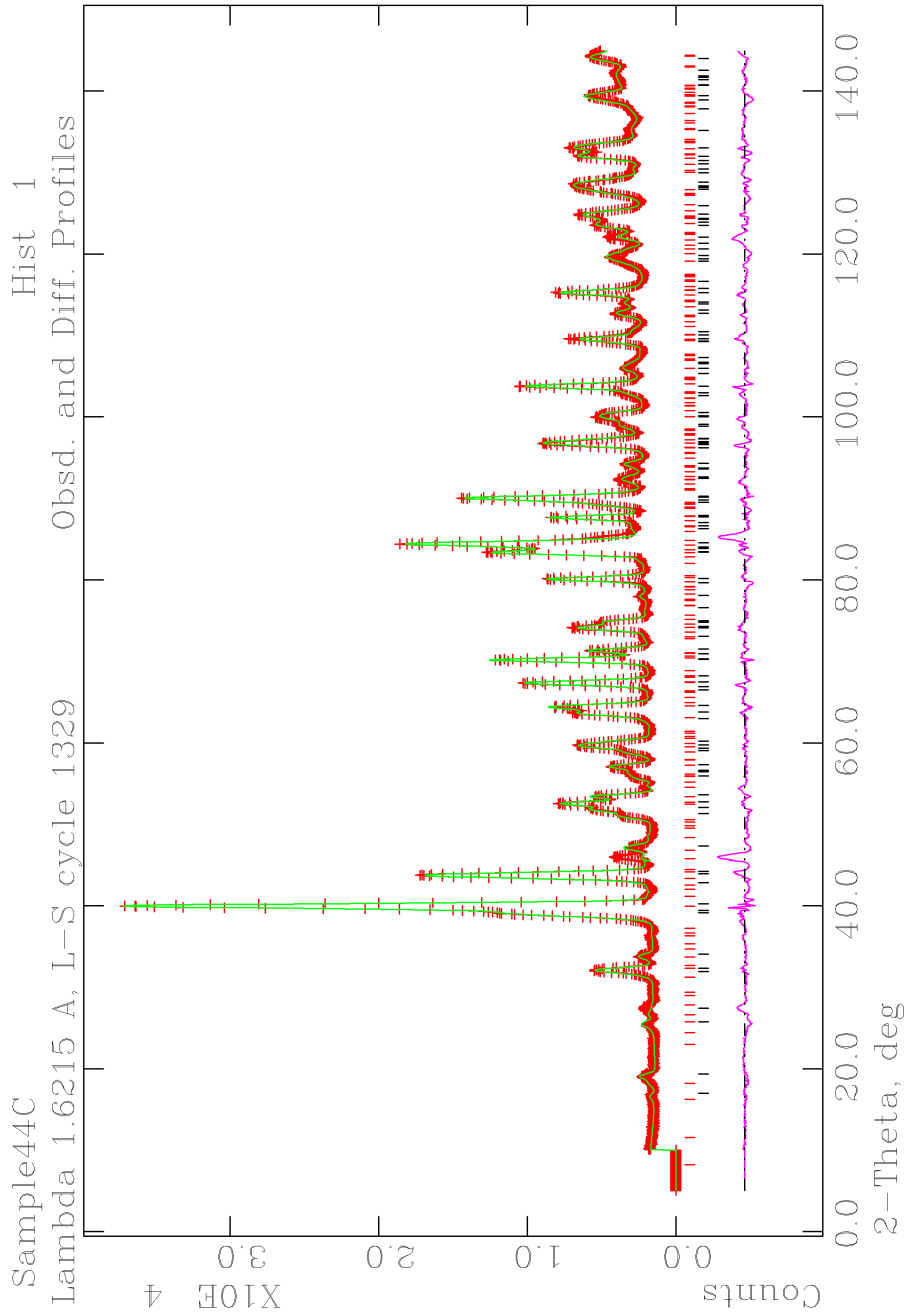

Figure 27.3. Rietveld refinement based upon NPD data for $Sr_{2.4}Ba_{0.5}Al_{0.9}P_{0.1}O_4F$

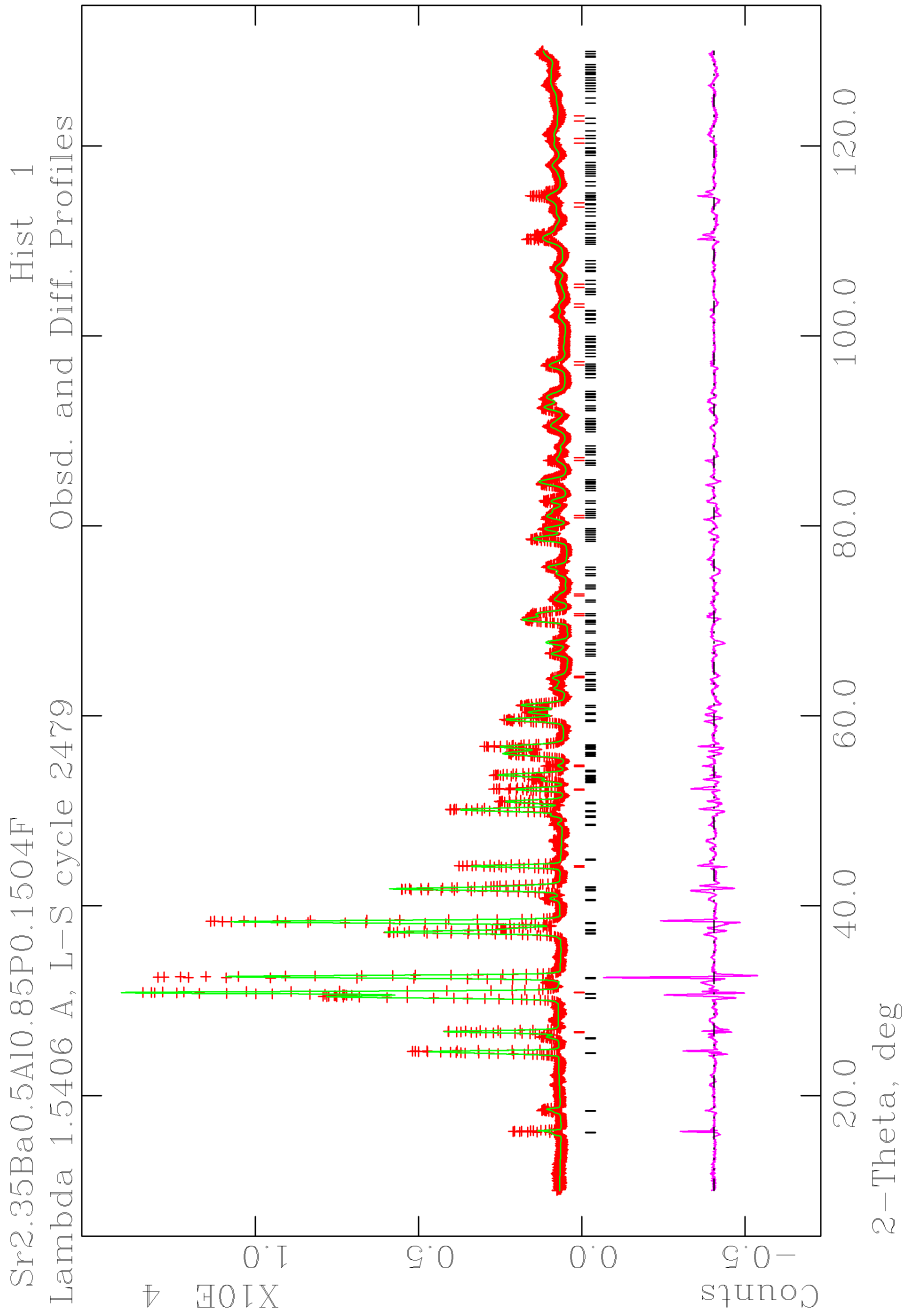

Figure 27.4. Rietveld refinement based upon PXRD data for $Sr_{2.35}Ba_{0.5}Al_{0.85}P_{0.15}O_4F$

Data for $Sr_{2.5-x}Ba_{0.5}Al_{1-x}P_xO_4F$ (x= 0, 0.05, 0.15) were collected *via* PXRD. Dr. Maxim Avdeev collected NPD data for $Sr_{2.4}Ba_{0.5}Al_{0.9}P_{0.1}O_4F$ at the Australian Nuclear Science and Technology Organization (ANSTO) in Sydney, Australia; this technique allows for higher resolution than PXRD. *Figure 28.3* displays black lines under the refinement that indicate where the expected peaks for the main phase would appear (Sr_3AlO_4F); the red lines are indicative of the main impurity, AlF_3, which is present in a 1.86% phase fraction compared with the main phase. The atomic positions and thermal parameters for the aluminum fluoride impurity are recorded in *Table 5*. Aluminum fluoride is acceptable as an impurity because it is not an impurity containing the dopant of interest and it did not disrupt the target unit cell from forming. Modeling this impurity helps to ensure that the atomic parameters of the unit cell were calculated correctly.

Table 5. Atomic Positions and Thermal Parameters of AlF_3 in $Sr_{2.4}Ba_{0.5}Al_{0.9}P_{0.1}O_4F$[60]

Atom	*x*	*y*	*z*	$U_{iso} \times 100$
Al	0.4205(3)	0.2829(2)	0	1.26(6)
Al	0.5	0	0	1.26(6)
F	0.3585(2)	0.4333(3)	0	0.26(6)
F	0.5049(2)	0.1568(3)	0	0.26(6)
F	0.4264(2)	0.2950(3)	0.5	2.51(9)
F	0.2839(3)	0.2162(3)	0	0.26(6)
F	0.5	0	0.5	2.51(9)

Space Group: *P*4/*mbm*; *a*= 11.588(6) Å; *c*= 3.550(4) Å

Photoluminescence

Photoluminescence data were collected on these phosphorus doped samples (x= 0.05, 0.10) before and after being treated in reducing conditions. Before being reduced an excitation of ~214 nm results in a broad emission with a λ_{max} of ~454 nm, as seen in *Figure 28.1*.

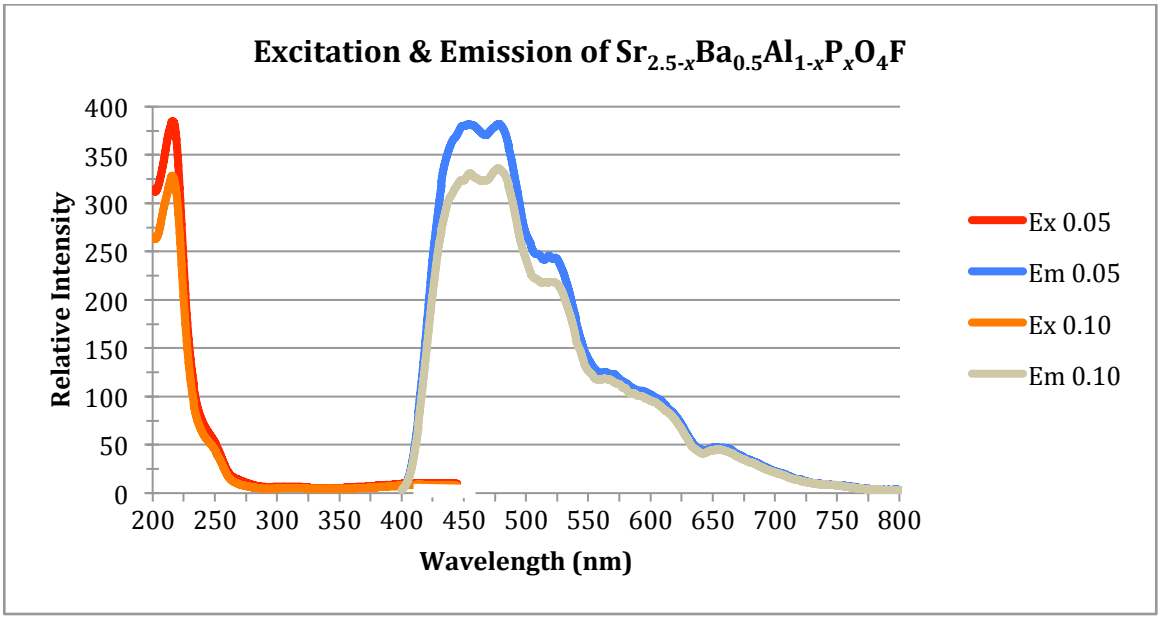

Figure 28.1. Excitation and emission spectra of $Sr_{2.5-x}Ba_{0.5}Al_{1-x}P_xO_4F$ (not reduced)

Reduced samples were prepared by post-synthesis annealing at 900℃ for one hour with a flow rate for $3\%H_2(g)/97\%N_2(g)$ of four seconds per bubble. No photoluminescence was observed for these samples. Reducing $Sr_{2.5-x}Ba_{0.5}Al_{1-x}P_xO4F$ under these conditions destroyed the previously observed photoluminescence in these samples. Another batch of unreduced samples were then reduced under a milder set of conditions, 800℃ for 30 minutes with the same flow rate for $3\%H_2(g)/97\%N_2(g)$ of four seconds per bubble, and the samples prepared using this method still exhibited photoluminescence, as seen in *Figure 28.2*. An important observation is that the intensity of the x= 0.10 sample after post-synthesis annealing is greater than that of x= 0.05, which was not the case before reduction. These reduced materials were analyzed *via* PXRD to confirm that the Sr_3AlO_4F host lattice was still present after annealing under reducing conditions, and it was in all cases.

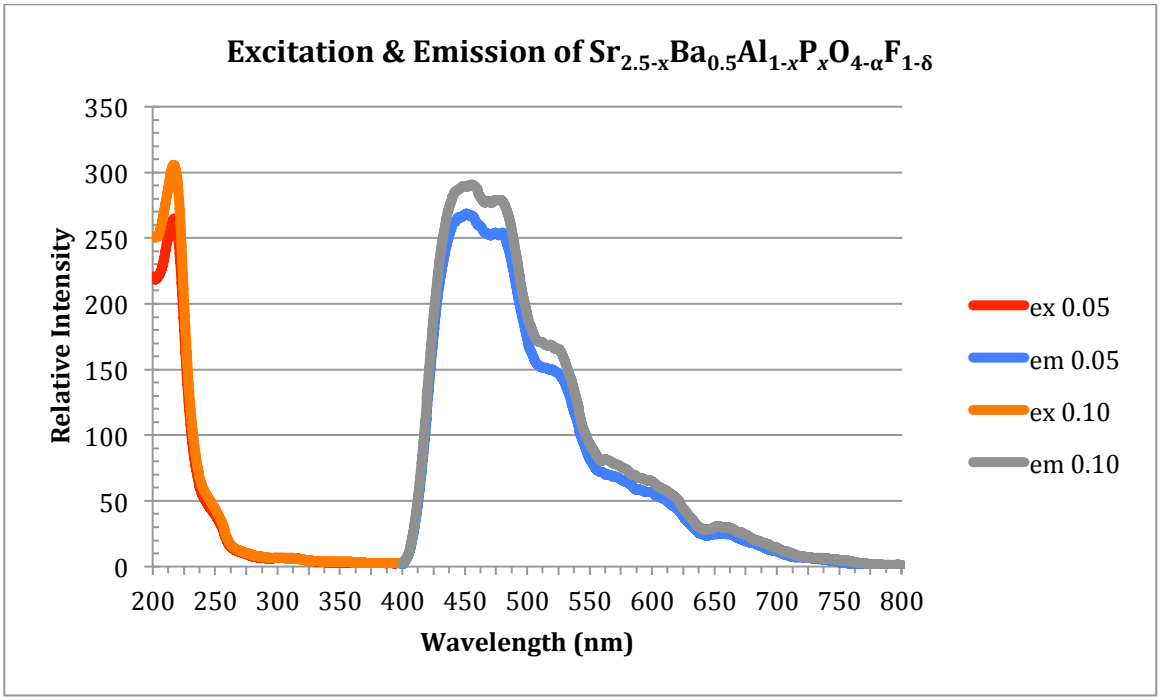

Figure 28.2. Excitation and emission spectra of $Sr_{2.5-x}Ba_{0.5}Al_{1-x}P_xO_{4-\alpha}F_{1-\delta}$ (reduced)

The CIE coordinates for the emissions were generated for the samples after being reduced, *Table 6*, and plotted in the blue region on the color space diagram, *Figure 29*. As the concentration of phosphorus is increased, the *x* and *y* CIE values are also increasing, moving slightly towards the white region of the color space. While the observed change is relatively minor, this speaks to the potential tunability of solid state lighting systems using phosphorus as a dopant.

Table 6. CIE *x* and *y* Coordinates of $Sr_{2.5-x}Ba_{0.5}Al_{1-x}P_xO_{4-\alpha}F_{1-\delta}$ (x= 0, 0.05, 0.10)

Compound	*x*	*y*
(a) $Sr_{2.5}Ba_{0.5}Al_1O_4F$	0.2189	0.2424
(b) $Sr_{2.45}Ba_{0.5}Al_{0.95}P_{0.05}O_4F$	0.2218	0.2495
(c) $Sr_{2.4}Ba_{0.5}Al_{0.9}P_{0.1}O_4F$	0.2269	0.2571

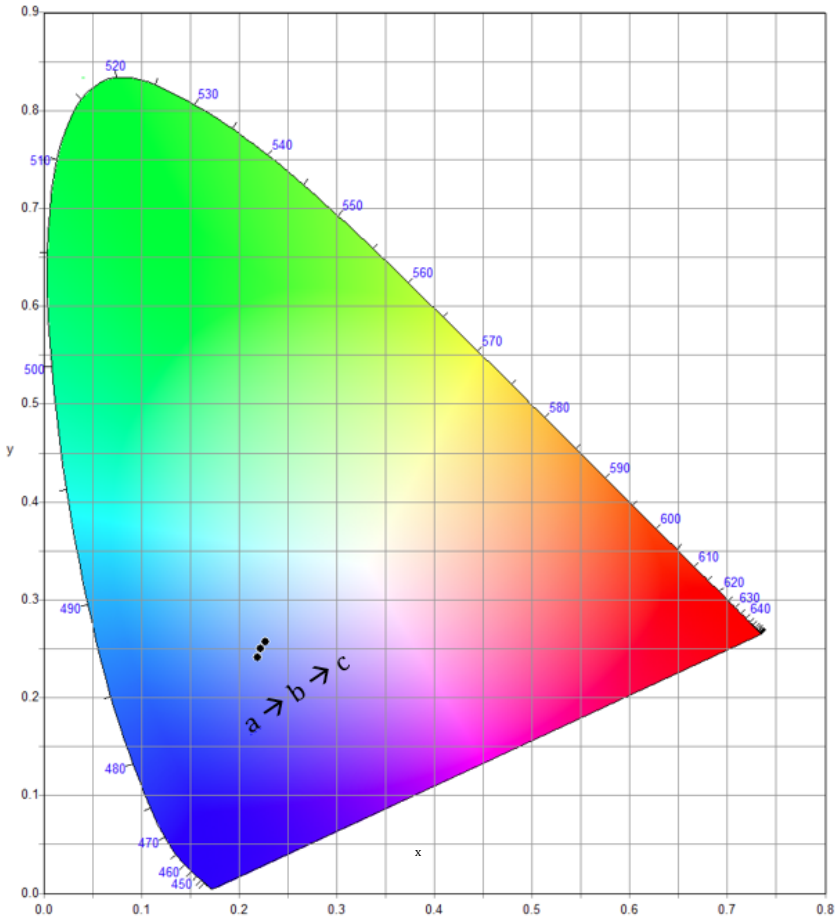

Figure 29. CIE plot of $Sr_{2.5-x}Ba_{0.5}Al_{1-x}P_xO_{4-\alpha}F_{1-\delta}$

Double Substitution

Further doping on $Sr_3Al_{0.9}P_{0.1}O_4F$ was investigated with the introduction of Zn^{2+}, following the work of Williams in the 1940s,[33] which was briefly discussed in *Chapter I, Important Phosphor Materials*. It was hypothesized that the incorporation of Zn^{2+} might play a role in enhancing the emission spectra without changing the structure of the lattice. The same synthesis protocol was used for this procedure, shown in *Scheme 5*, using stoichiometric amounts of the pure, dried starting materials, and following the same heating times of 12-16 hours at 700, 800, and 900 °C, respectively, and then 48-72 hours at 1050 °C for up to three times with intermittent grinding in an agate mortar and pestle. Zn^{2+} was used at 0.1 equivalents since this was the highest dopable concentration of P^{5+}; P^{5+} was also kept at 0.1, and Na^{+} was added at a concentration of 0.1 to charge compensate for each Zn^{2+} cation added and therefore not require the formation of any vacancies.

$$2\,SrCO_3 + 0.05\,Na_2CO_3 + 0.9\,SrF_2 + 0.4\,Al_2O_3 + 0.1\,(NH_4)_2HPO_4 + 0.1\,ZnO \rightarrow Sr_{2.9}Na_{0.1}Al_{0.8}P_{0.1}Zn_{0.1}O_4F$$

Scheme 5. Synthesis of $Sr_{2.9}Na_{0.1}Al_{0.8}P_{0.1}Zn_{0.1}O_4F$

Analysis of this white polycrystalline powder shows that zinc was not properly incorporated into the anti-perovskite lattice. An integrated X-ray powder diffraction software (PDXL) was used to determine what phases are present in the given compound; PDXL generates figures of merit based on how well the observed peaks match up with the expected peaks; as this value approaches 1 this indicates a better match. The Sr_3AlO_4F lattice was not present, and of the three main phases, one of the impurities

contained zinc (gahnite), while all three of the impurities contained aluminum. These impurities are possibly due to the number of starting materials used. High temperature solid state synthesis typically uses the smallest number of starting materials possible, disallowing any side reactions to occur and generate impurities before the synthesis of the hypothesized host lattice. Information about the main impurities (Al_2O_3, gahnite (Al_2O_4Zn), and AlF_3)[61,62,60] is shown in *Table 7* and plotted in *Figure 30*.

Table 7. $Sr_{2.9}Na_{0.1}Al_{0.8}P_{0.1}Zn_{0.1}O_4F$ Impurity Phases from PDXL

Formula	*FOM*	*Space Group*	*Lattice Parameters (Å)*
Al_2O_3	1.664	*C*2/*m*	*a*= 11.795(5)
			b= 2.910(1)
			c= 5.621(2)
Al_2O_4Zn	1.589	$Fd\bar{3}m$	*a*= 8.091(5)
			b= 8.091(5)
			c= 8.091(5)
AlF_3	1.739	*P*4/*mbm*	*a*= 11.403(4)
			b= 11.403(4)
			c= 3.544(1)

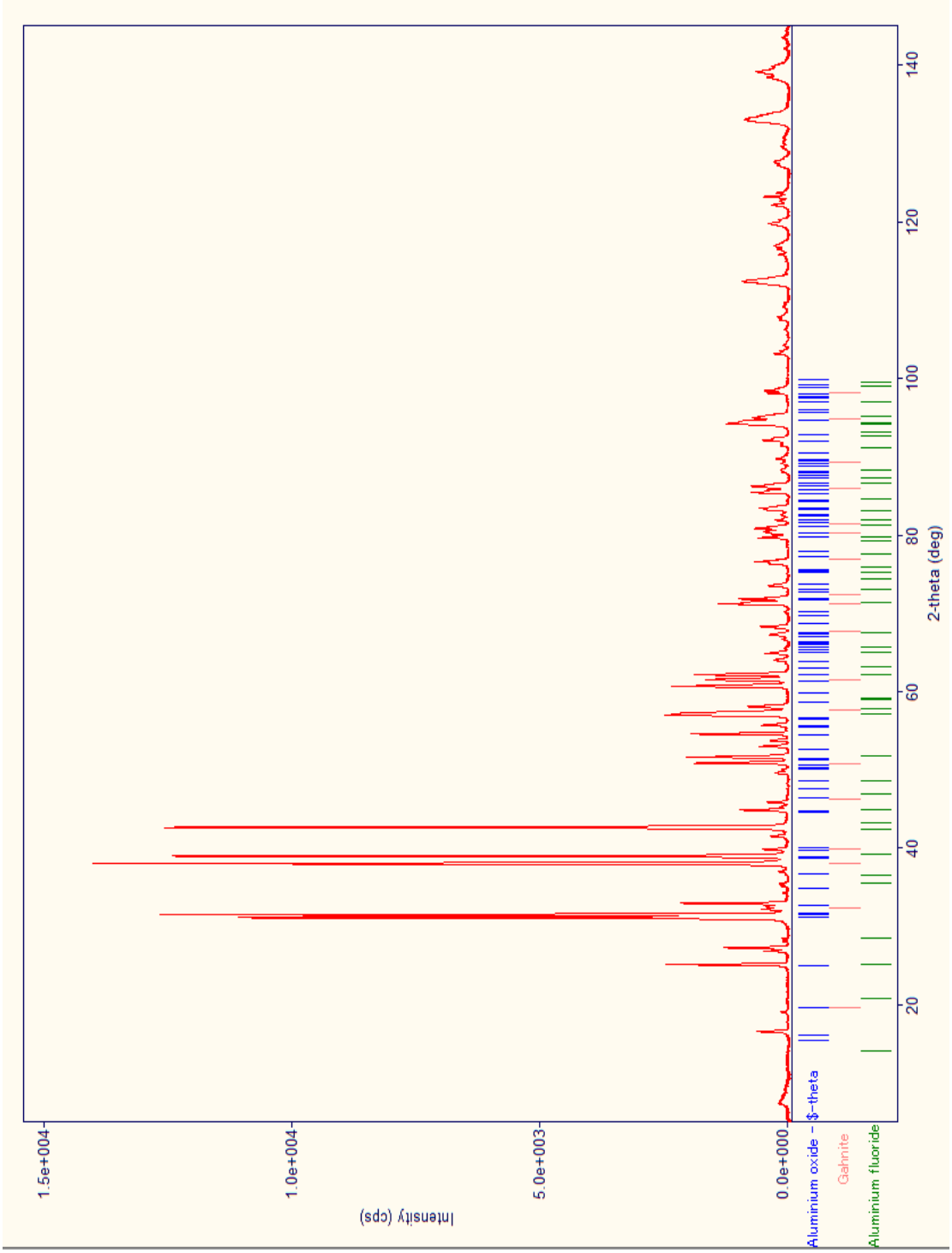

Figure 30. PXRD pattern for attempted synthesis of $Sr_{2.9}Na_{0.1}Al_{0.1}P_{0.1}Zn_{0.1}O_4F$ showing peaks for main phases present

CHAPTER V

CHARACTERIZATION OF THE STRONTIUM ALUMINUM OXYFLUORIDE UPON DOPING WITH YTTRIUM

Yttrium was chosen as a dopant due to the isovalent nature compared to phosphorus, but one concern was the steric hindrance due to the Y^{3+} ion being larger than the Al^{3+} ion (1.04 Å *vs* 0.53 Å).[46] Considering this large size difference, Ba^{2+} was not included for these syntheses. The doping range for Y^{3+} was broader than that of P^{5+}; while $0 \leq x \leq 0.1$ was investigated, $0 \leq x \leq 1$ was primarily investigated to see if yttrium would completely replace aluminum in the Sr_3AlO_4F compound. A structurally related compound with YO_4^{5-} polyhedra has not yet been reported in the literature, so the doping concentration was investigated as high as $x = 1$ to discover whether a pure Sr_3YO_4F phase was possible.

After gathering PXRD data, an integrated X-ray powder diffraction software (PDXL) was used to determine what phases are present in the given compound. Y^{3+} was not found to incorporate into the Sr_3AlO_4F lattice, but information on phases observed and their peak positions and intensities can be evaluated before starting Rietveld refinements. Since Y^{3+} was not shown to incorporate into the lattice, many impurities were generated during the reaction. As opposed to Rietveld refinements, *Figures 31.1-31.4* are shown to indicate the powder diffraction and a few impurity phases. These figures encompass the compounds with Y^{3+} concentrations of $x = 0.25$, 0.50, 0.75, and

1.0, the phase views for $0 \leq x \leq 0.1$ are included in *Appendix A*. A few of the impurities seen are the starting materials (SrF_2) or their immediate byproducts (SrO from decomposing $SrCO_3$). The other "impurities" are called such because they are the phases being generated though this synthesis, not the products hypothesized. *Tables 8.1-8.4* show the main impurities seen as well as their space group and their figure of merit, FOM.

Table 8.1. $Sr_3Al_{0.75}Y_{0.25}O_4F$ Impurity Phases from PDXL[63,64,65]

Formula	*FOM*	*Space Group*	*Lattice Parameters (Å)*
$Sr_{1.7}Y_{1.2}F_7$	1.364	Not determined, seen as a byproduct	n/a
SrY_2O_4	1.804	*Pnam*	*a*= 10.090* *b*= 11.901* *c*= 3.412*
$YAlO_3$	2.106	*Pbnm*	*a*= 5.330(2) *b*= 7.375(2) *c*= 5.180(2)

*Standard deviation not reported

Table 8.2. $Sr_3Al_{0.5}Y_{0.5}O_4F$ Impurity Phases from PDXL[60,66,67,68]

Formula	*FOM*	*Space Group*	*Lattice Parameters (Å)*
AlF_3	1.333	*P*4/*mbm*	*a*= 11.403(4) *b*= 11.403(4) *c*= 3.544(1)
Al_2Y	1.460	$Fd\bar{3}m$	*a*= 2.368* *b*= 2.777* *c*= 4.535*
YOF	1.570	*Pmnb*	*a*= 3.096* *b*= 1.896* *c*= 1.617*
$Sr_6Y_2Al_4O_{15}$	1.677	*C*2	*a*= 17.597(1) *b*= 5.741(1) *c*= 7.686(1)

*Standard deviation not reported

Table 8.3. $Sr_3Al_{0.25}Y_{0.75}O_4F$ Impurity Phases from PDXL[69,64,70]

Formula	*FOM*	*Space Group*	*Lattice Parameters (Å)*
SrO	0.703	$Fm\bar{3}m$	*a*= 5.159*
			b= 5.159*
			c= 5.159*
SrY_2O_4	0.823	*Pnam*	*a*= 10.090*
			b= 11.901*
			c= 3.412*
SrF_2	1.095	$Fm\bar{3}m$	*a*= 5.800(3)
			b= 5.800(3)
			c= 5.800(3)

*Standard deviation not reported

Table 8.4. Sr_3YO_4F Impurity Phases from PDXL[71,68,72]

Formula	*FOM*	*Space Group*	*Lattice Parameters (Å)*
$Y_3Al_2(AlO_4)_3$	1.387	$Ia\bar{3}d$	*a*= 2.689(4)
			b= 4.909(1)
			c=1.667(3)
$Sr_6Y_2Al_4O_{15}$	1.542	*C*2	*a*= 17.597(1)
			b= 5.741(1)
			c= 7.686(1)
$Sr_7Y_6F_{30}O$	1.642	$R\bar{3}H$	*a*= 14.498(2)
			b= 14.498(2)
			c= 9.926(1)

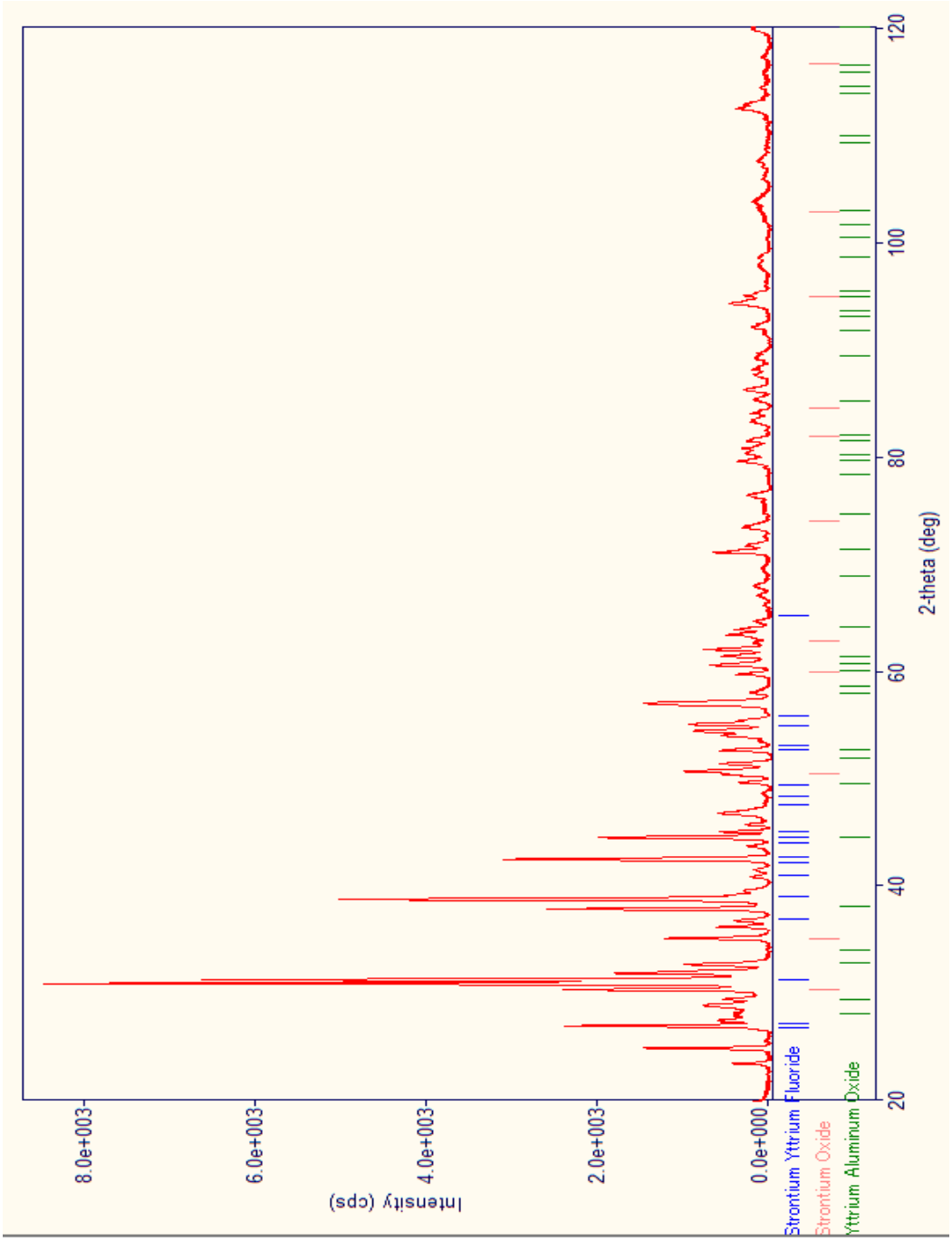

Figure 31.1. PXRD pattern for attempted synthesis of $Sr_3Al_{0.75}Y_{0.25}O_4F$ showing peaks for main phases present

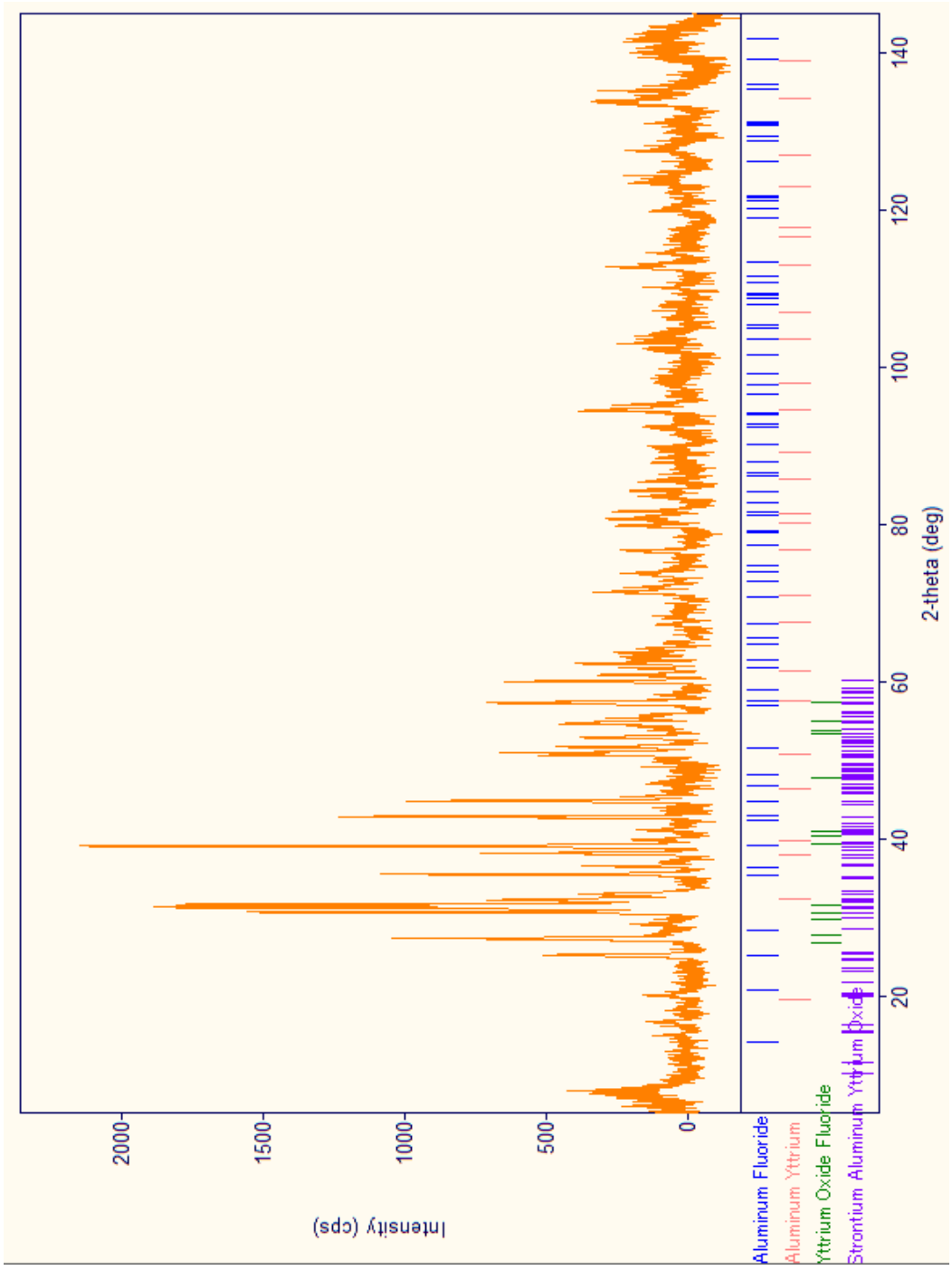

Figure 31.2. PXRD pattern for attempted synthesis of $Sr_3Al_{0.5}Y_{0.5}O_4F$ showing peaks for main phases present

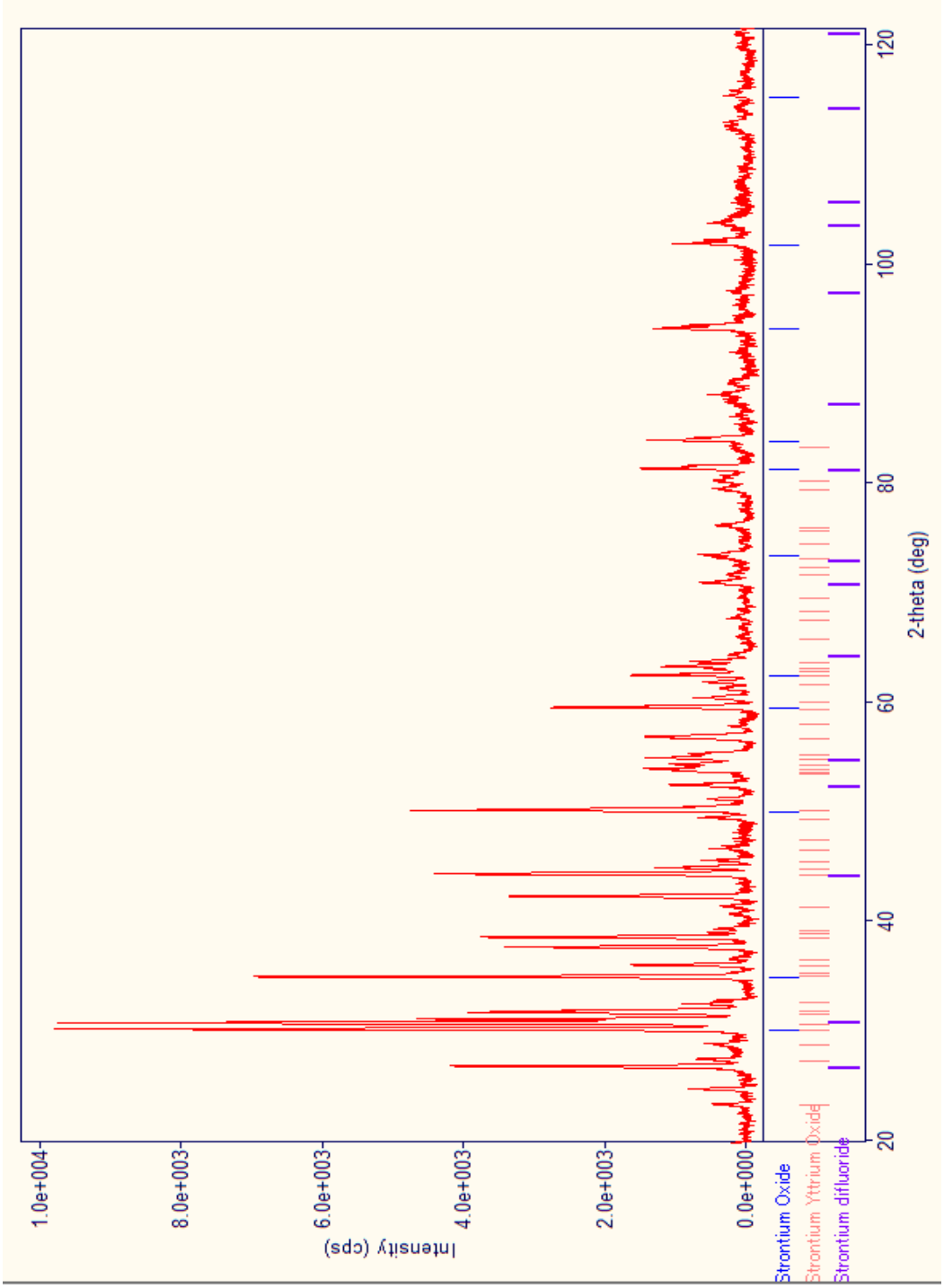

Figure 31.3. PXRD pattern for attempted synthesis of $Sr_3Al_{0.25}Y_{0.75}O_4F$ showing peaks for main phases present

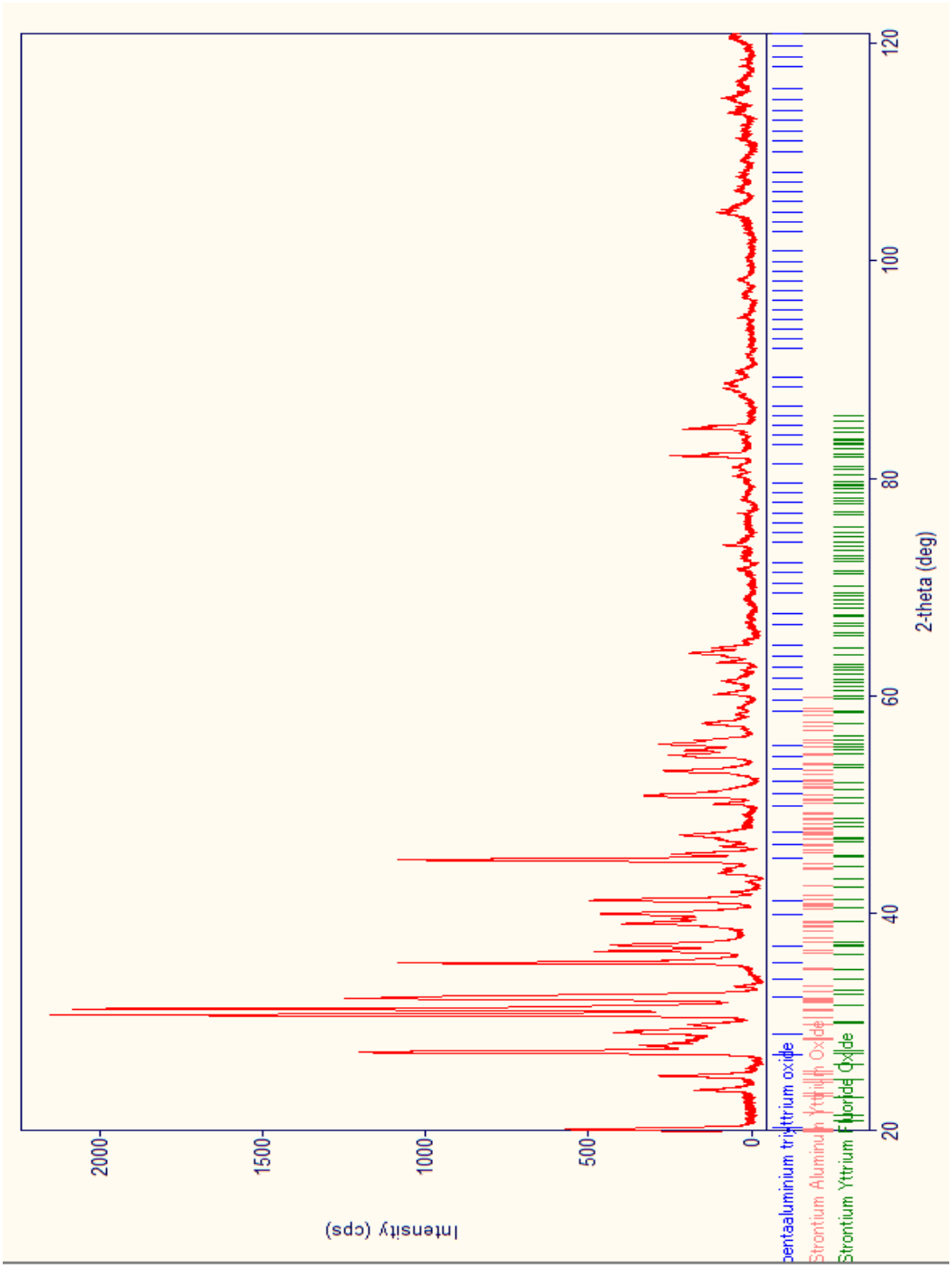

Figure 31.4. PXRD pattern for attempted synthesis of Sr_3YO_4F showing peaks for main phases present

CHAPTER VI

CHARACTERIZATION OF THE NOVEL STRONTIUM ALUMINUM OXYFLUORIDE DOPED WITH HAFNIUM, $Sr_{2.5-\frac{x}{2}}Ba_{0.5}Al_{1-x}Hf_xO_4F$ [$0 \leq x \leq 0.1$]

Synthesis and Characterization

Following the standard heating as discussed in *Chapters IV & V*, the Sr_3AlO_4F host lattice was successfully doped with a small amount of Hf^{4+}, yielding the white polycrystalline compound $Sr_{2.4875}Ba_{0.5}Al_{0.975}Hf_{0.025}O_4F$. The data were gathered for this sample *via* PXRD with a range of 2θ= 5-145° at every 0.10 degrees at a rate of 0.20 degrees/minute; the data were then analyzed through Rietveld refinement to determine the lattice parameters, atomic positions, thermal stability, bond length, and valences. The $Sr_{2.4875}Ba_{0.5}Al_{0.975}Hf_{0.025}O_4F$ structure was confirmed to have an *I*4/*mcm* space group. After completing the Rietveld refinement, *Figure 32*, the atomic positions and thermal parameters were calculated using GSAS and EXPGUI and are displayed in *Table 9*, the bond lengths were calculated for *Table 10*, and the bond valence sums were calculated to determine the global stability index as shown in *Table 11*.

Table 9. Atomic Positions and Thermal Parameters of $Sr_{2.4875}Ba_{0.5}Al_{0.975}Hf_{0.025}O_4F$

Atom	*x*	*y*	*z*	$U_{iso} \times 100$
Sr(1)/Ba(1)	0	0	0.25	0.844(4)
Sr(2)	0.1689(0)	0.6689(0)	0	0.570(7)
Al/Hf	0	0.50	0.25	2.11(9)
O	0.1410(0)	0.6410(0)	0.6452(0)	1.26(0)
F	0	0	0	2.93(7)

Space Group: *I*4/*mcm*; χ^2= 6.8; *a*= 6.8606(1) Å; *c*= 11.1682(5) Å

Table 10. Selected Bond Lengths of $Sr_{2.4875}Ba_{0.5}Al_{0.975}Hf_{0.025}O_4F$

Bond	*Length (Å)*
8 × Sr(1)-O	2.893(5)
2 × Sr(1)-F	2.792(8)
4 × Sr(2)-O	2.681(4)
2 × Sr(2)-O	2.456(4)
2 × Sr(2)-F	2.550(4)
4 × Al-O	1.800(3)

Table 11. Bond Valence Sums and Global Stability Index of $Sr_{2.4875}Ba_{0.5}Al_{0.975}Hf_{0.025}O_4F$

Atom	V_i	S_{ij}	d_i
Sr(1)/Ba(1)	2	1.2168	-0.7832
Sr(2)	2	2.1229	0.1229
Al/Hf	3	2.4578	-0.5422
O	2	1.6982	-0.3018
F	1	1.1275	0.1275
G		0.34	

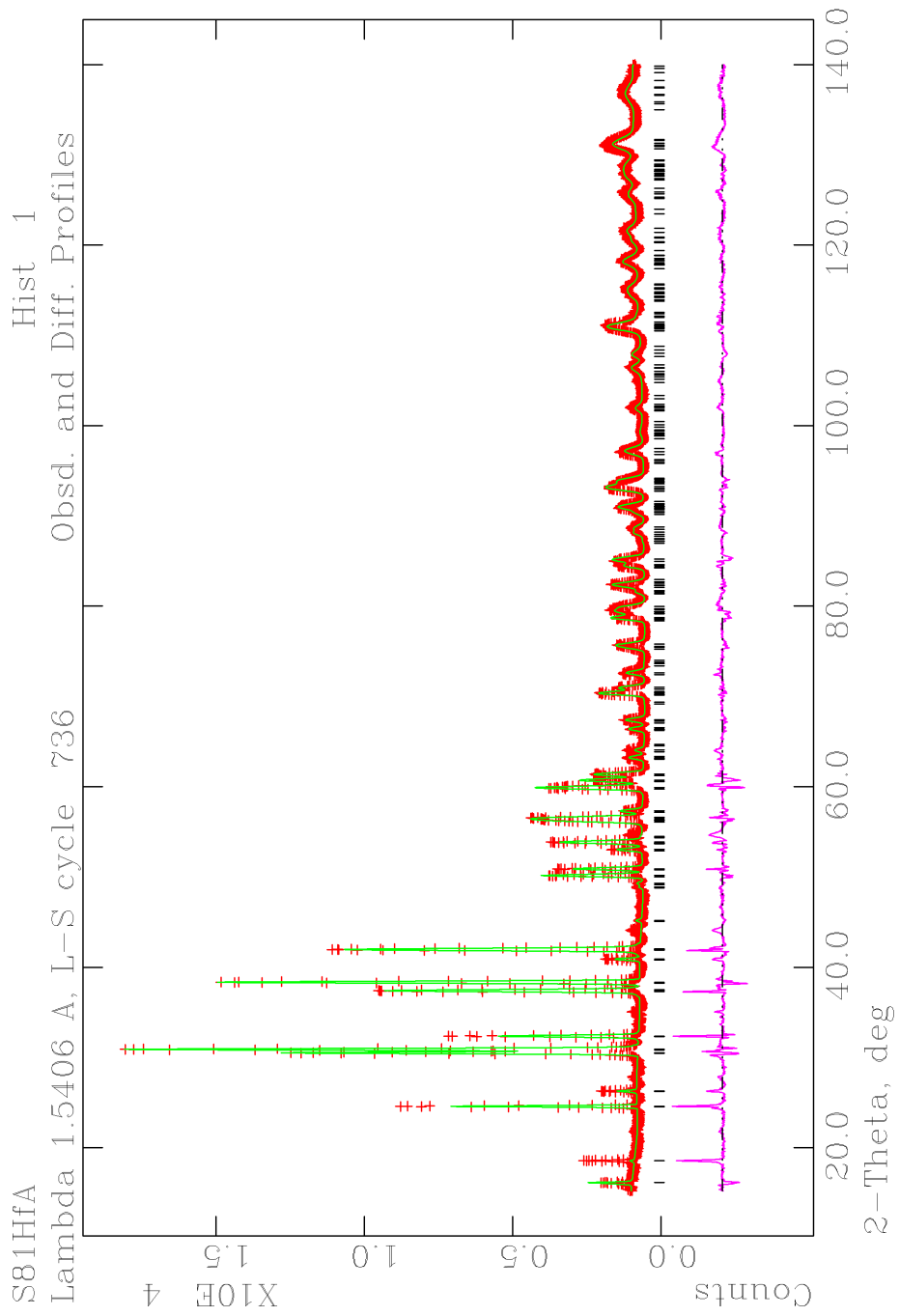

Figure 32. Rietveld refinement based upon PXRD data for $Sr_{2.4875}Ba_{0.5}Al_{0.975}Hf_{0.025}O_4F$

Hafnium was not able to incorporate onto the *M*-site at higher concentrations. Increasing concentrations of Hf^{4+} led to more impurities but these impurities did not revolve around hafnium, which would indicate that this dopant was successfully being incorporated into the host lattice. The impurities that arose were most commonly SrF_2 or SrO, suggesting Hf^{4+} may be incorporating on the strontium (*A*) site and not the aluminum (*M*) site as hypothesized. The Hf^{4+} ion is larger than the Al^{3+} ion (0.58 Å vs 0.39 Å, respectively)[46] but this should not disallow Hf^{4+} from incorporating on this site; compared to the Sr^{2+} ion, which is about twice as large as the Hf^{4+} ion, it would be able to incorporate onto the strontium site even with the addition of barium.

The global instability index is also an indication of how Hf^{4+} may be incorporating onto the strontium site. Introducing Hf^{4+} onto the strontium site would result in more strain on these crystals that already have a high level of strain, rationalizing a *G* value that is higher than what is typical for these crystals.

For the samples of $Sr_{2.5-\frac{x}{2}}Ba_{0.5}Al_{1-x}Hf_xO_4F$ synthesized where x= 0.05, 0.075, and 0.1 the refinements were constrained to allow disorder on both the *A* and *M* sites to determine where the Hf^{4+} is bonding during synthesis. As the concentration increased, the fractional amount of Hf^{4+} on the Al^{3+} site was decreasing while increasing on the Sr(1) site. The two median concentrations seemed to incorporate hafnium on both sites, but the amount of impurities and strain on the cell did not lead to worthwhile refinement of these compounds. At the highest concentration of Hf^{4+} [x= 0.1] when fractionalizing the amount of Hf^{4+} on the *A* or *M* sites, the peak positions and intensities had a more acceptable goodness of fit value (χ^2) when fully introduced on the *A* site as opposed to the

M-site as targeted, further supporting the new hypothesis of Hf^{4+} incorporating onto the Sr(1) site.

Photoluminescence

Upon synthesis there was not an observable photoluminescence for these materials. To induce photoluminescence the samples were annealed using a slightly milder set of reducing conditions than in *Chapter IV, Photoluminescence*: 800℃ for 60 minutes with a flow rate for 3%H_2(*g*)/97%N_2(*g*) of four seconds per bubble; this method induced photoluminescence in all of the Hf^{4+}doped samples. Post-reduction the samples were analyzed *via* PXRD to determine if the Sr_3AlO_4F host lattice was still present, which it was in all cases. All samples showed a broad emission centered around 445 nm with an excitation near 250 nm. These materials would be a good fit for a host lattice for PC-LEDs because of the broad emission seen across ~415-600 nm, resulting in a net white emission, as seen on the CIE plot. These excitation and emission bands are shown in **Figure 33**, whereas **Figure 34** shows how these values correspond to the 1931 color space diagram for the $Sr_{2.4875}Ba_{0.5}Al_{0.975}Hf_{0.025}O_{4-\alpha}F_{1-\delta}$ sample (x= 0.2323, y= 0.3110).

Photoluminescence data were collected for various synthesized materials even though the higher concentrations have more strontium impurities due to the Hf^{4+} being incorporated onto the Sr^{2+} site. This can be seen by the lower concentrations having a slightly higher intensity than the samples with a higher concentration of Hf^{4+}. While it is possible that this could be the result of concentration quenching, most dopants can be introduced up to x= 0.1; however, due the non-stoichiometric nature of these compounds because of the strontium impurities, this may not be the case. With a weak intensity overall, adjusting the starting materials to the appropriate stoichiometric amounts may

lead to a brighter emission and another option for solid state lighting. Note the *y* axis (intensity) for these samples is set at 100 but the maximum intensity is 57, whereas the intensity in *Figure 28.1* and *Figure 28.2* is well over 300. Future work with the appropriate stoichiometric amounts of starting materials for the introduction of Hf^{4+} on the Sr^{2+} site would follow *Scheme 6*. Further investigation of doping Hf^{4+} on this cell could also be carried out where *A*= Ba or Ca and where *M*= Ga instead of Al.

$$2.5\text{-}2x\ SrCO_3 + 0.5\ SrF_2 + x\ HfO_2 + Al_2O_3 \rightarrow Sr_{3\text{-}2x}Hf_xAlO_4F$$

Scheme 6. Synthesis of $Sr_{3\text{-}2x}Hf_xAlO_4F$

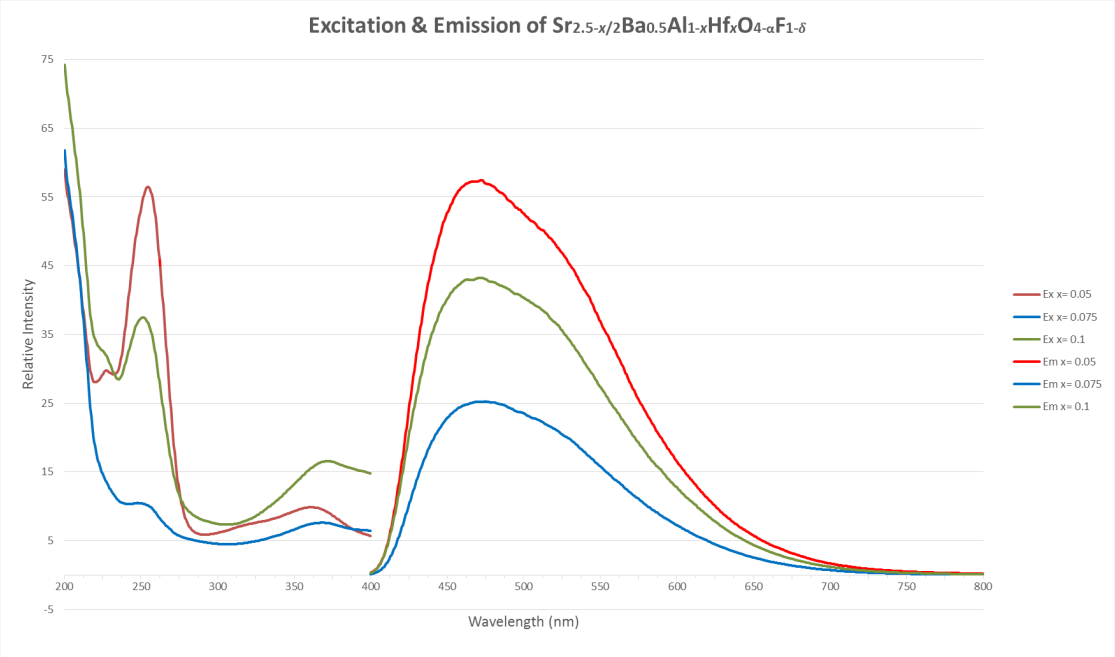

Figure 33. Excitation and emission spectra of $Sr_{2.5-\frac{x}{2}}Ba_{0.5}Al_{1-x}Hf_xO_{4-\alpha}F_{1-\delta}$

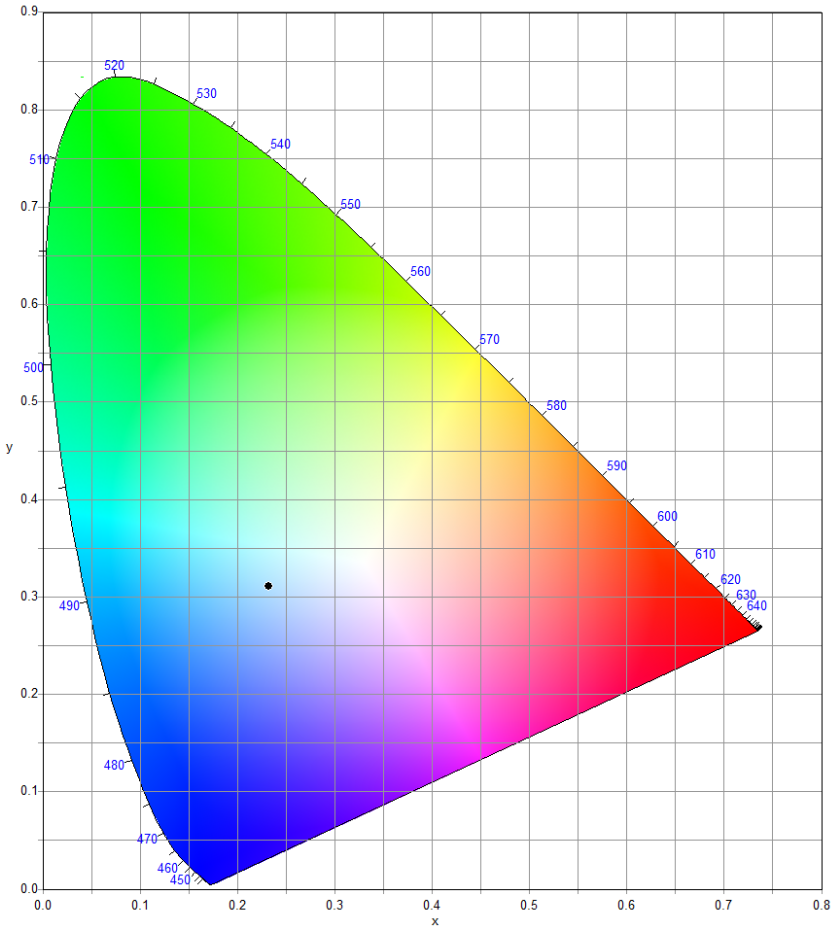

Figure 34. CIE plot of $Sr_{2.4875}Ba_{0.5}Al_{0.975}Hf_{0.025}O_{4-\alpha}F_{1-\delta}$

CHAPTER VII

CONCLUSIONS AND FUTURE RESEARCH REGARDING THESE NOVEL PHOSPHOR MATERIALS

The primary concluding work of this thesis is the successful incorporation of phosphorus onto the *M*-site in the Sr_3AlO_4F host lattice up to 0.10 equivalents. After analysis through PXRD or NPD and characterization though Rietveld refinement with EXPGUI & GSAS, no major impurities were present in the $Sr_{2.5}Ba_{0.5}AlO_4F$ or $Sr_{2.45}Ba_{0.5}Al_{0.95}P_{0.05}O_4F$ products, but a small (2%) impurity of AlF_3 was present in the $Sr_{2.4}Ba_{0.5}Al_{0.9}P_{0.1}O_4F$ sample. These samples were shown to be photoluminescent materials when excited at 214 nm, emitting at a wavelength near 454 nm; the excitation and emission values are comparable to those in the literature, meaning that this phosphor could be useful if incorporated into a PC-LED. Also, incorporation of P^{5+} on the *M* site is one of the few aliovalent metals to be substituted on this site, joining Si^{4+} and Ge^{4+}.[45] After being reduced for 1 hour at 900 °C in a 3% H_2(g)/97% N_2(g) environment, the samples did not show any photoluminescence. When reduced under the milder reducing conditions of 30 minutes at 800 °C, photoluminescence was induced, and the samples were shown to have a broad emission around 450 nm when excited at 214 nm.

In regards to the $Sr_{3-x}Al_{1-x}P_xO_4F$ material, future investigation as to the use of gallium instead of aluminum would be worthwhile. Both Al^{3+} and Ga^{3+} compounds have been successfully synthesized as photoluminescent materials, and substituting Ga^{3+} for

Al^{3+} has been shown to have a shift on the photoluminescence of a given material. On the *A*-site, tuning with Ba^{2+} and Ca^{2+} has also shown to impact the observed fluorescence and would be a worthwhile investigation.

Investigatory research was done on the substitution of the isovalent Y^{3+} onto the Al^{3+} site, but it did not incorporate into the $Sr_3Al_{1-x}Y_xO_4F$ lattice. Concentrations of yttrium were increased up to x= 1 due to the yet unreported structure containing a YO_4^{5-} tetrahedron. The large size of Y^{3+} as opposed to P^{5+} is likely the reason for yttrium not incorporating into the lattice. Formation of the $Ca_3A_{1-x}Y_xO_4F$ oxyfluoride might be a beneficial experiment for trying to incorporate yttrium onto a photoluminescent anti-perovskite oxyfluoride. Investigating if yttrium incorporates onto the strontium site would also be worthwhile as yttrium has the largest ionic radii out of the dopants introduced in this thesis; with this it is possible that if Y^{3+} does successfully incorporate, some degree of structural rearrangement may need to take place to allow for this.

Hafnium was shown to successfully incorporate into the Sr_3AlO_4F host lattice on the *M*-site at a lowest concentration of x= 0.025. The optical properties of this material show a broad emission between ~410-600 nm when excited at ~251 nm, making this material potentially beneficial for PC-LEDs. At higher concentrations of Hf^{4+}, it appears to be doping onto the *A*-site in a disordered fashion, so this would be the first thing to investigate. As stated for further investigation of P^{5+} compounds, substituting Ga^{3+} for Al^{3+} and the tunability of Ca^{2+} versus Ba^{2+} would be a sensible investigation. It might also be interesting to explore how photoluminescence is impacted when doped with excess amounts of fluorine; this may increase the efficiency of the Hf^{4+} doped phosphor but could also change the structure.

REFERENCES

1. Rohwer, L. S.; Srivastava, A. M. *Electrochem. Soc. Interface.* **2003,** *12*, 36-39.
2. U.S. Department of Energy. http://energy.gov/energysaver/articles/how-energy-efficient-light-bulbs-compare-traditional-incandescents (accessed Aug 1, 2015).
3. Home Guides, Energy Efficient Bulbs. http://homeguides.sfgate.com/energyefficient-bulbs-halogen-*vs*-fluorescent-*vs*-incandescent-78832.html (accessed Mar 26, 2015).
4. Thomas, P.J.; Carpenter, D.; Boutin, C.; Allison, J.E. *Chemosphere,* **2014**, *96*, 57–66.
5. Smith, K.S.; Huyck, H.L.O. *Reviews in Econ. Geol.* **1999,** *6A-6B*.
6. Georgia State University: HyperPhysics. http://hyperphysics.phy-astr.gsu.edu/hbase/solids/pnjun.html (accessed Dec 1, 2015).
7. Shenai-Khatkhate, D. V.; Goyette, R. J.; DiCarlo, R. L. Jr.; Dripps, G. *J. Cryst. Growth*, **2004**, *272,* 816-821.
8. Popular Science Background: The Nobel Prize in Physics 2014. http://www.nobelprize.org/nobel_prizes/physics/laureates/2014/popular-physicsprize2014.pdf (accessed Jul 1, 2015).
9. From Theory to Applications. In *Luminescence*; Ronda, C., Ed.; WILEY-VCH Verlang Gm bH & Co., 2008; Vol.1 ; p 1-33, 133-188.
10. Holonyak, N.; Bevacqua, S.F. *Appl. Phys. Lett.* **1962,** *1*.
11. Spitzer, S.M.; North, J.C. *J. Appl. Phys.* **1973,** *44*, 214.
12. Simon, Y.C. *J. Mater. Chem.* **2012,** *22*, 20817-20830.
13. Ronda, C.R.; Jüstel, T.; Nikol, H. *J. Alloys and Compd*. **1998,** *257-277,* 669-676.
14. Huang, R.; Li, S.; Xue, S.; Jiang, Z.; Wu, S. *IACSIT Press, Singapore*, **2012,** *28*, 85-89.
15. Hasegawa, Y.; Nakanishi, T. *RSC Adv.* **2015,** *5*, 338-353.

16. Popular Mechanics: Incandescent *vs* Compact Fluorescent *vs* LED. http://www.popularmechanics.com/technology/gadgets/reviews/g164/incandescent-*vs*-compact-fluorescent-*vs*-led-ultimate-light-bulb-test/ (accessed Nov 2, 2015).
17. MDidea: Camera Effects and Differences of Displayed Products. http://www.mdidea.com/support/orderhelp/photo/CameraEffectsandDifferencesofDisplayedProducts.html (accessed Nov 1, 2015).
18. Smith, T.; Guild, J. *Transactions of the Optical Society,* **1931,** *33*, 73-134.
19. SmartEnergy Energy Conversion: Color Correlated Temperature. http://www.smartenergy.company (accessed Oct 30, 2015).
20. Green, M.A.; Ho-Baillie, A.; Snaith, H.J. *Nature Photonics,* **2014,** *8*, 506-514.
21. Pfaff, G. *Mat. Chem.* **1994,** *6*, 58-62.
22. Johnsson, M.; Lemmens, P. "Crystallography and Chemistry of Perovskites" (unpublished; http://arxiv.org/pdf/cond-mat/0506606.pdf)
23. Takeda, Y.; Kanamaru, F.; Shimada, M.; Koizumi, M. *Acta Cryst.* **1976,** *B32*, 2464-2466.
24. Chen, W.; Liang, H.; Ni, H.; He, P.; Su, Q. *J. Electrochem. Soc.* **2010,** *157*, J1159-J163.
25. Kissel, T.; Brübach, J.; Euler, M.; Frotscher, M.; Litterscheid, C.; Albert, B.; Dreizler, A. *Matt. Chem. & Physics,* **2013,** *140*, 435-440.
26. Sullivan, E.; Vogt, T. *ECS J. Solid State Sci. Tech.* **2012,** *2,* R3088-R3099.
27. Setlur, A.A., *The Electrochemical Society Interface*, **Winter 2009**, 32-36.
28. Shinomura, Y.; Honma, T.; Shigeiwa, M.; Akai, T.; Okamoto, K.; Kijima, N. *J. Electrochem. Soc.* **2007,** *154*, J35-J38.
29. Zhang, Z. *ECS J. Solid State Sci. & Tech.* **2013,** *2*, R70-R75.
30. H.W. Leverenz, U.S. patent 2066044 (1936).
31. McMurdie, H.F.; Evans, M.C.; Paretzkin, E.H.; Wong-Ng, B.; Errlinger, L. *Powder Diffr.* **1986,** *1*, 92.
32. Goldschmidt, V.M. *Nachr. Ges, Wiss. Göttingen, Math-Physik. KI.* **1931,** 184-190.
33. Williams, F.E. *J. Opt. Soc. Am.* **1947,** *37*, 302.
34. F.E. Williams, U.S. patent 2447448 (1945).

35. Bless, P.W.; von Dreele, R.B.; Kostiner, E.; Hughes, R.E. *J. Solid State Chem.* **1972,** *4*, 262.
36. Kostiner, E.; Bless, P.W. *J. Electrochem. Soc.* **1971,** *118*, 351.
37. Vogt, T.; Woodward, P. M.; Hunter, B. A.; Prodjosantoso, A. K.; Kennedy, B. J. *J. Solid State Chem.* **1999,** *144,* 228-231.
38. Prodjosantoso, A.K.; Kennedy, A.J.; Vogt, T.; Woodward, P.M. *J. Solid State Chem.* **2003,** *172*, 89-94.
39. Park, S.; Vogt, T. *J. Am. Chem. Soc.* **2010,** *132*, 4516-4517.
40. Shang, M.; Li, G.; Kang, X.; Yang, D.; Geng, D.; Lin, J. *ACS Appl. Mater. Interfaces.* **2011,** *3*, 2738-2746.
41. Park, S. *Lumin.* **2012,** *132*, 875-879.
42. Green, R.; Vogt. T. *J. Solid State Chem.* **2012,** *194*, 375-384.
43. Green, R. L. (2013). *Structural and Photoluminescent Characterization of Substituted A_3MO_4F (A = Sr, Ba, Ca; M = Al, Ga, In, Si and Ge).* (Doctoral dissertation). Retrieved from http://scholarcommons.sc.edu/etd/2529
44. Im, W.B.; George, N.; Kurzman, J.; Brinkley, S.; Mikhailovsky, A.; Hu, J.; Chmelka, B.F.; DenBaars, S.P.Seshadri, R. *Adv. Mater.* **2011,** *23*, 2300-2305.
45. Lee, J.S.; Unithrattil, S.; Im, W.B. *J. Alloys Compd.* **2013,** *555*, 297-303.
46. Shannon, R.D. *Acta Crystallogr,* **1976,** *A23*, 751-761.
47. Sullivan, E. *J. Solid State Chem.* **2012,** *194*, 375-384.
48. Huang, C.H.; Chen, Y.C.; Kuo, T.W.; Chen, T.M. *J. Lumin.* **2011,** *131,* 1346-1349.
49. Shimadzu: Excellence in Science. http://www.shimadzu.com/an/elemental/edxrf/edx7000_8000/index.html (accessed Aug 20, 2015).
50. Drenth, J. **2002.** X-Ray Crystallography Encyclopedia of Molecular Biology.
51. Sears, V. F. *Neutron News*. **1992**, *3*, 26-37.
52. Rietveld, H.M. *Acta. Cryst.* **1966,** *20*, 508.
53. Rietveld, H.M. *Acta. Cryst.* **1966,** *21*, A228.
54. Rietveld, H.M. *Acta. Cryst.* **1967,** *22*, 151.
55. Rietveld, H.M. *J. Appl. Cryst.* **1969,** *2*, 65-71.
56. Toby, B.H. *J. Appl. Cryst.* **2001,** *34*, 210-213.

57. Adams, S. *Acta. Cryst. B,* **2001,** *57*, 278.
58. Bond Valences. In *Structural Bonding*; Brown, I.D.; Poepplermeier, K.R., Eds.; Springer-Verlag Berlin Heidelberg: 2014; Vol. 158.
59. Brown, I.D. *Chem. Rev.* **2009,** *109*, 6858-6919.
60. Herron, N.; Thorn, D.L.; Harlow, R.L; Jones, G.A.; Parise, J.B.; Fernandez-Baca, J.A.; Vogt, T. *Chem. Mater.* **1995,** *7*, 75-83.
61. Zhou, R.S.; Snyder, R. *Acta Crystallogr. Sec. B: Struct. Sci*. **1991,** *47*, 617.
62. Levy, D.; Pavese, A.; Sani, A.; Pischedda, V. *Phys. Chem. Min.* **2001,** *28*, 612-618.
63. Patwe, S.; Achary, S.; Tyagi, A.; Moorthy, P. *Mater. Res. Bull.* **1999,** *34*, 761.
64. Kurosaki, K.; Tanaka, T.; Maekawa, T.; Yamanaka, S. *J. Alloys Compd.* **2005,** *395*, 318-321.
65. Diehl, R.; Brandt, G. *Mater. Res. Bull.* **1975,** *10*, 85.
66. Kistaiah, P.; Saryanarayana-Muthy, K.; Reddy, CV.; Appa-Rao, B. *J. Less-Common Met.* **1987,** *134*, 91.
67. Bendeliani, N. *Sov. Phys. Dokl.* **1975,** *20*, 526.
68. Wang, C.H.; Gua, D.F.; Li, Z.F.; Wang, X.M.; Lin, J.H.; Zeng, Z.Z.; Jing, X.P. *J. Solid State Chem.* **2012,** *192*, 195-200.
69. Strontium oxide (SrO) crystal structure, lattice parameters, thermal expansion. In *II-VI and I-VII Compounds; Semimagnetic Compounds;* Madelung, O., Rössler, U., Schulz, M., Eds.; Springer Berlin Heidelberg, 1999; Vol. 41B; p 1-3.
70. Wang, J.S.; Ma, C.L.; Zhou, D.; Xu, Y.S.; Zhang, M.Z.; Gao, W.; Zhu, H.Y.; Cui, Q.L. *J. Solid State Chem.* **2012,** *186*, 231.
71. Carda, J.; Tena, M.A.; Monros, G.; Esteve, V.; Reventos, M.M.; Amigo, J.M. *Cryst. Res. Technol.* **1994,** *29*, 387.
72. Achary, S.N.; Tyagi, A.K.; Koehler, J. *Mater. Chem. Phys.* **2004,** *88*, 207.
73. Solid State Chemistry: An Introduction. Smart, L.E., Moore, E.A., Eds.; CRC Press, Boca Raton, 2012, Vol. 4; p 1-326.

APPENDIX A

PDXL VIEW OF UNREPORTED SAMPLES

The following figures are data collected *via* PXRD with 2θ= 5-145° at every 0.10 degrees at a rate of 0.20 degrees/minute, plotted as intensity *vs*. 2θ. Sr_3AlO_4F was selected as a reference (Sr_3GaO_4F for only *F.A2*) so the corresponding peaks can be matched up visually; any impurities for these samples are not reported as these are preliminary results or scans used to help verify a variety of conditions such as melting temperatures and if a dopant of interest would be worth investigating further. PDXL plots are only included for the highest heating of each sample set, the preliminary scans after 700, 800, 900, and initial 1050° C are not shown. Various samples are not reported based on the sample melting or not yielding enough material for proper analysis.

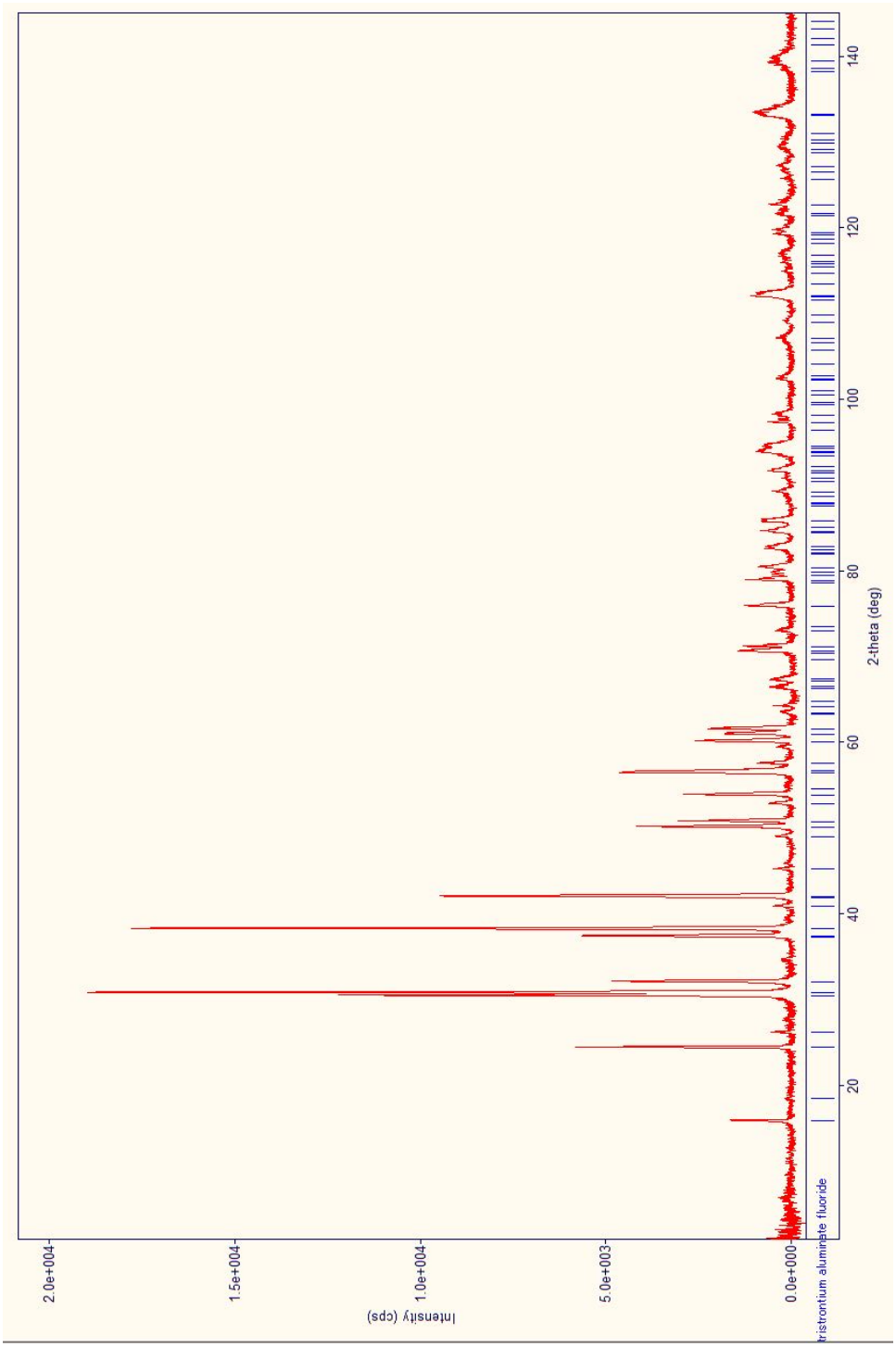

Figure A1. Undoped Sr_3AlO_4F

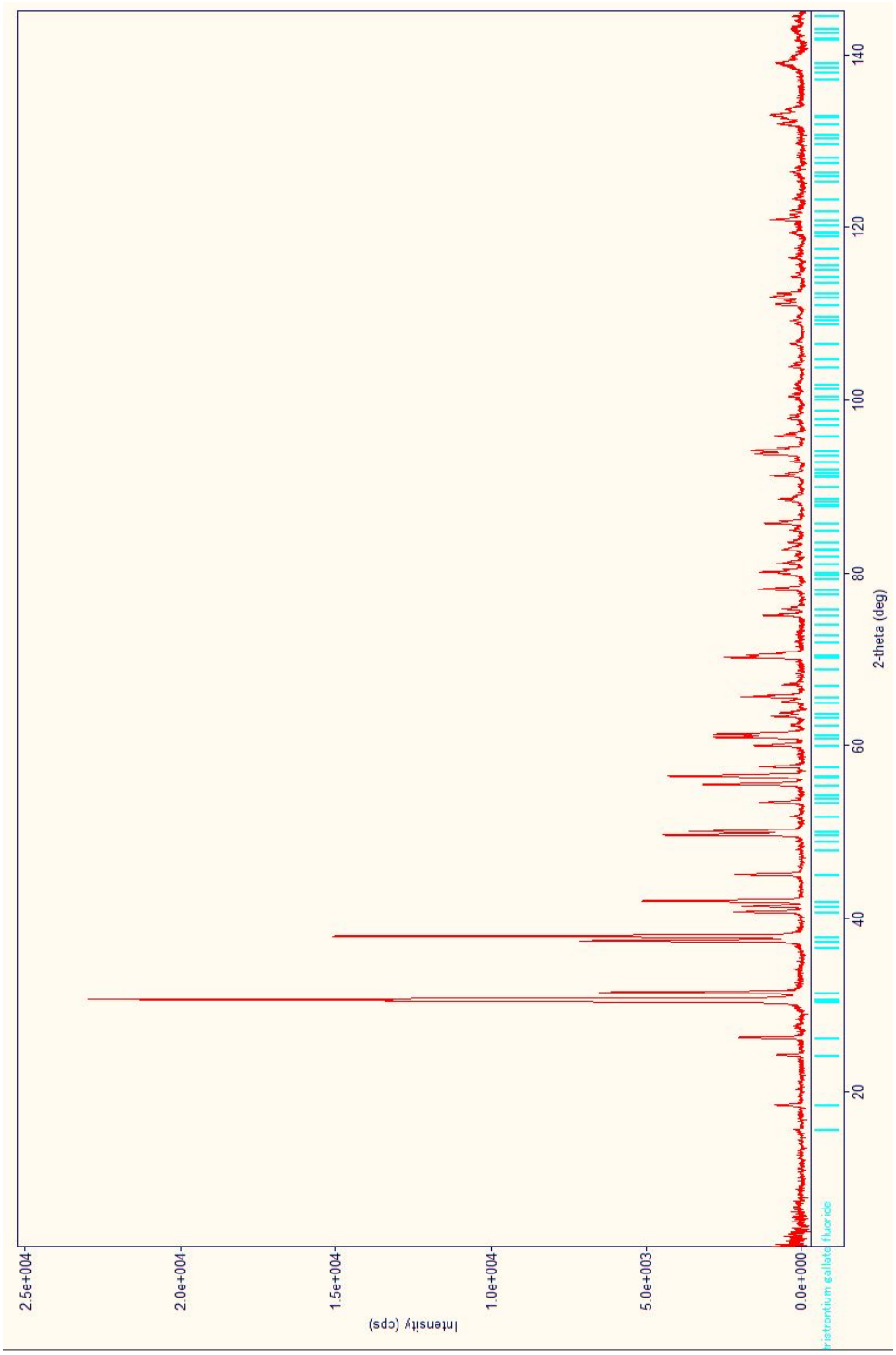

Figure A2. Undoped Sr_3GaO_4F

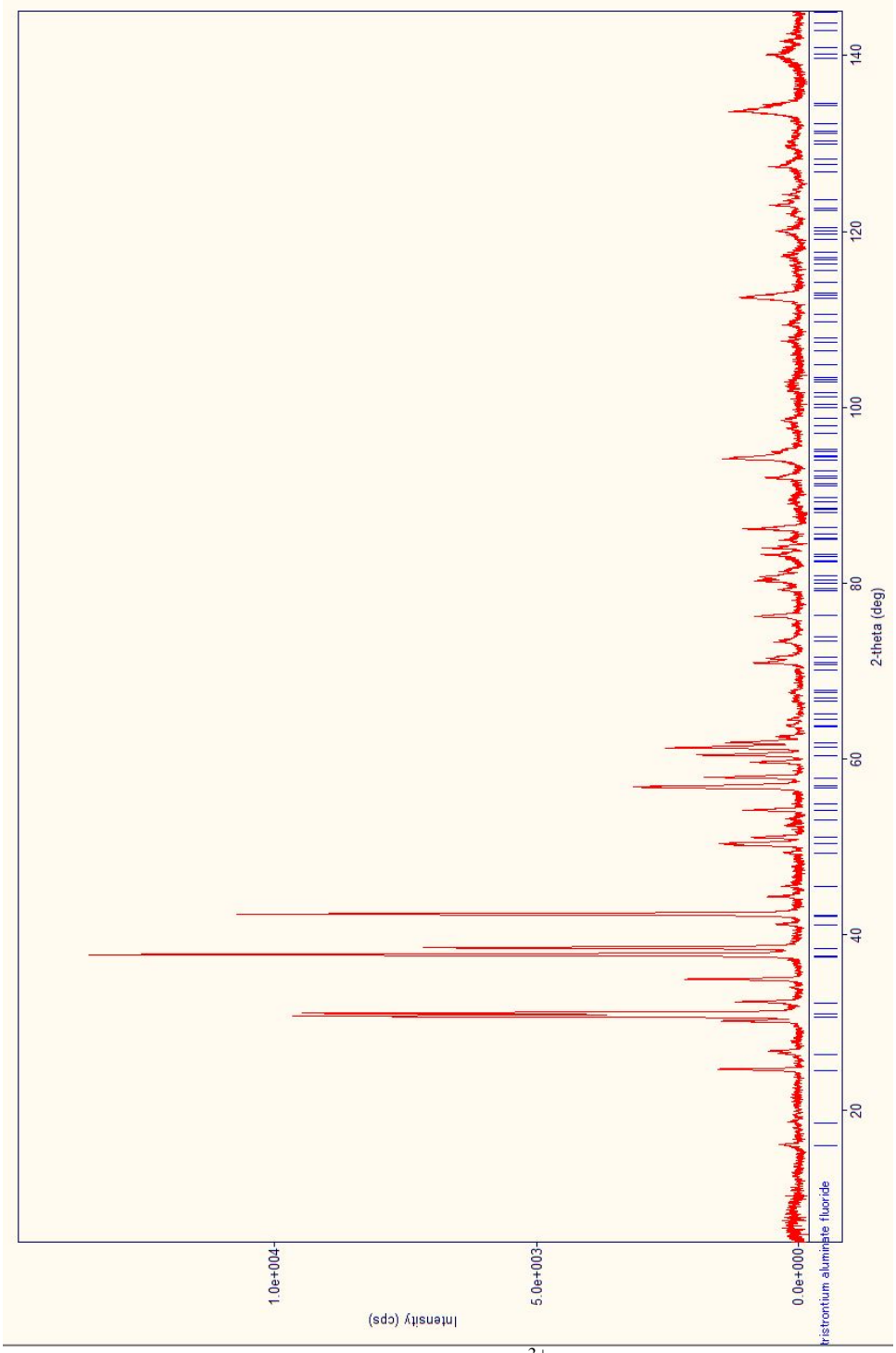

Figure A3. $Sr_3AlO_4F:Y^{3+}$ [x= 0.05]

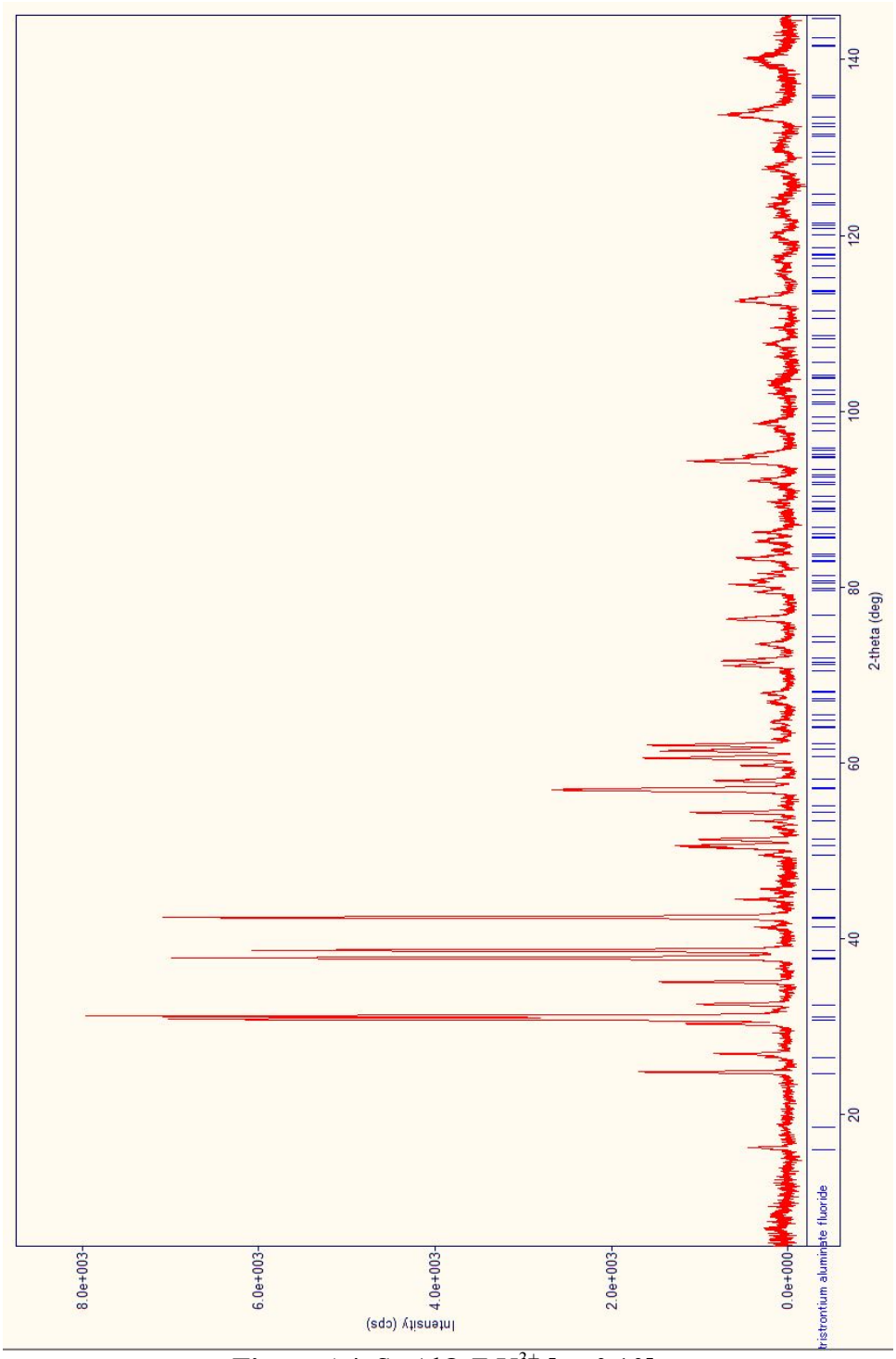

Figure A4. $Sr_3AlO_4F:Y^{3+}$ [x= 0.10]

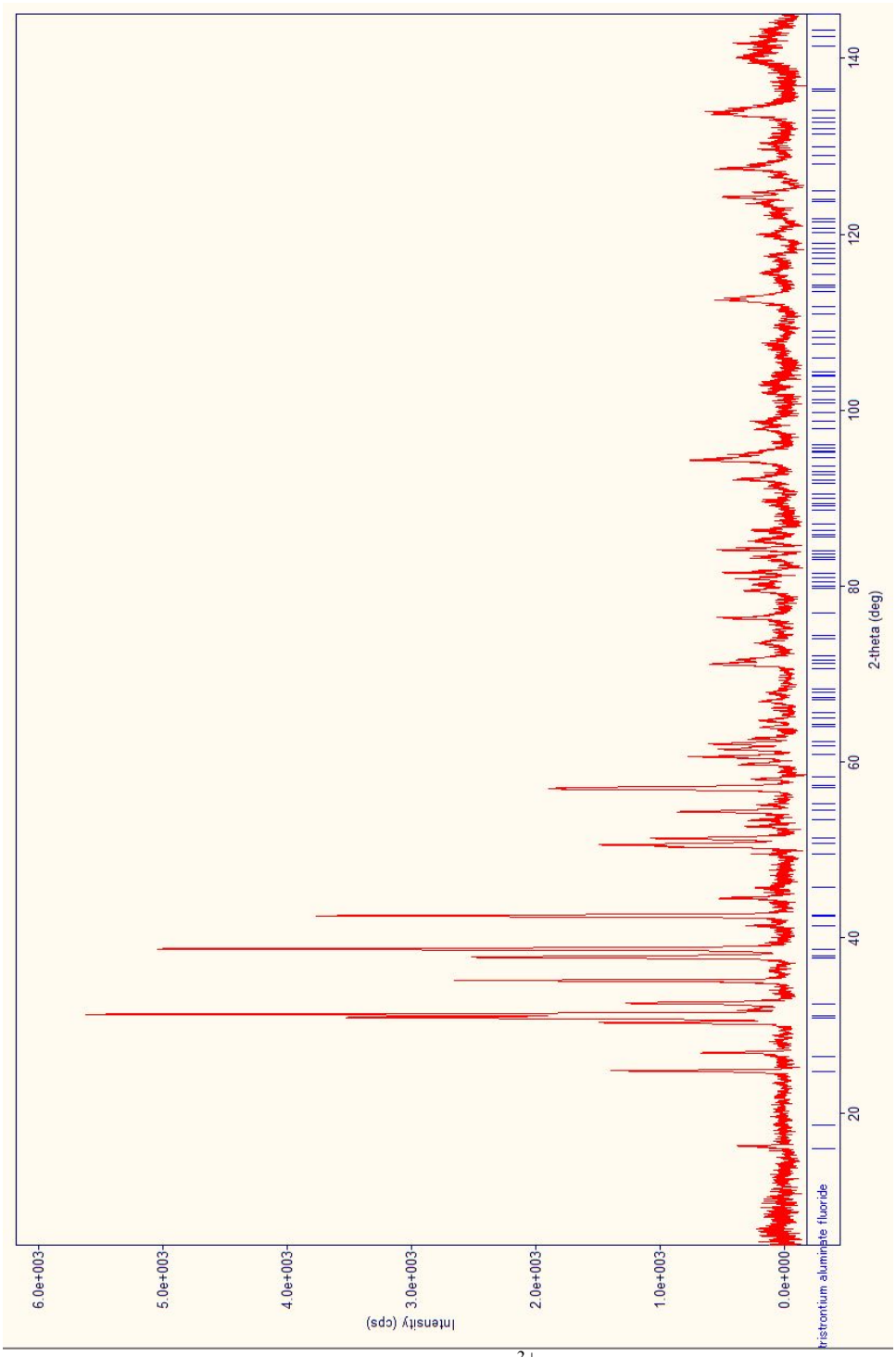

Figure A5. $Sr_3AlO_4F:Y^{3+}$ [x= 0.15]

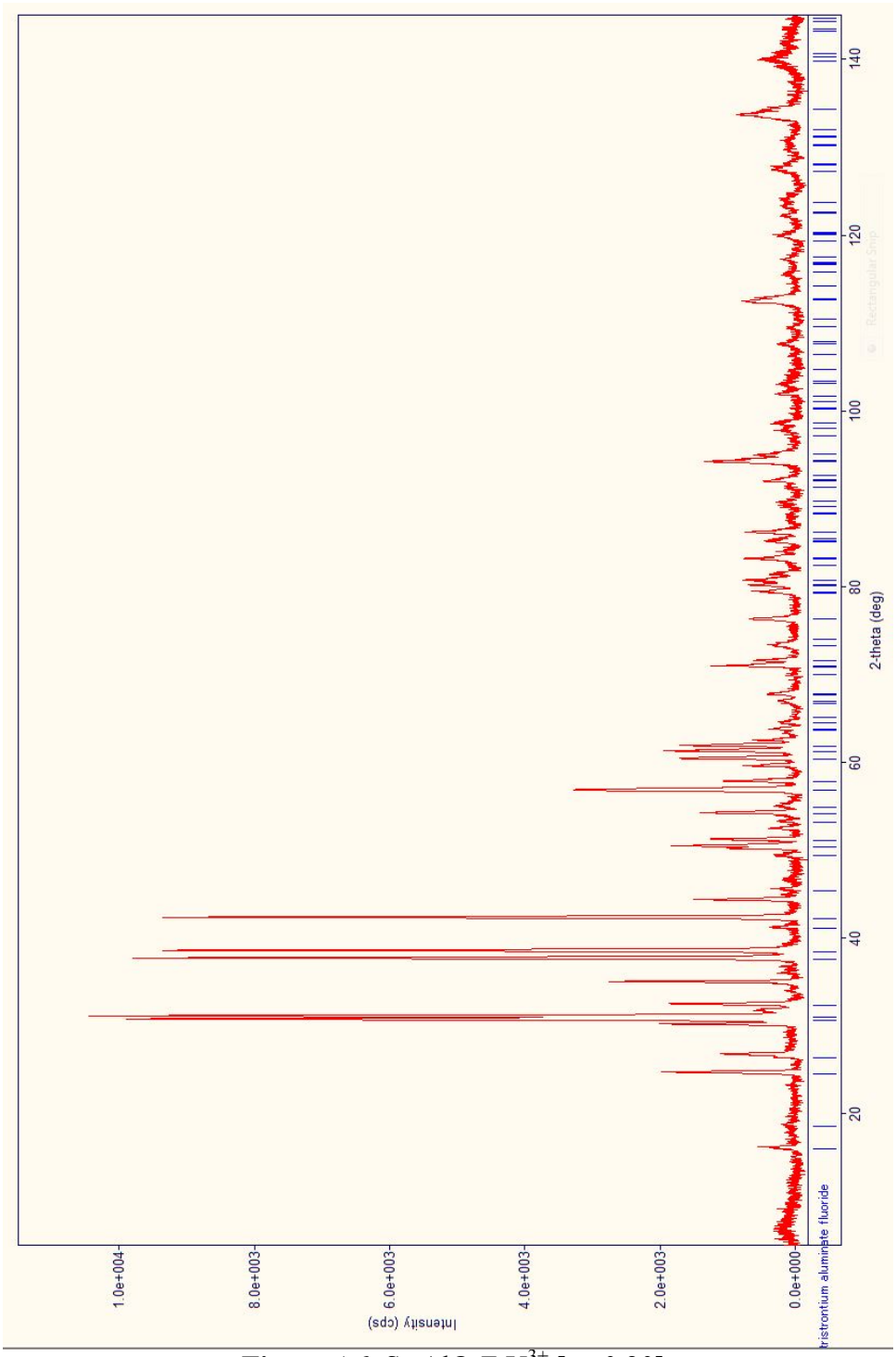

Figure A6. $Sr_3AlO_4F:Y^{3+}$ [x= 0.20]

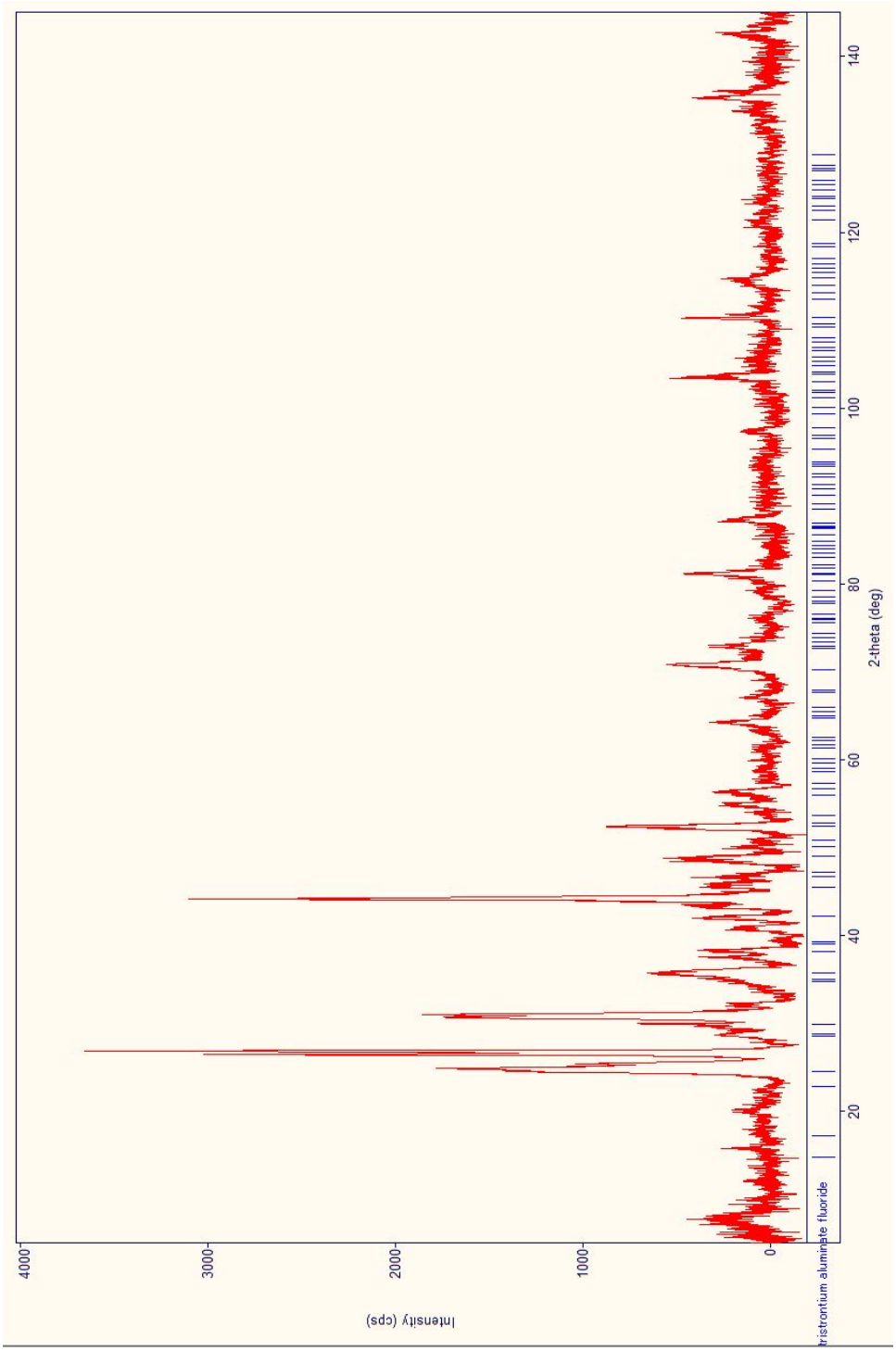

Figure A7. $Sr_{2.5}Ba_{0.5}Al_{0.9}Y_{0.1}O_4F$